
Electronic Thesis and Dissertation Repository

8-26-2022 10:00 AM

Atrial Fibrillation and Cognitive Decline: a Computational Hemodynamics Investigation

Timothy J. Hunter, *The University of Western Ontario*

Supervisor: Goldman, Daniel, *The University of Western Ontario*

Co-Supervisor: McIntyre, Christopher W, *The University of Western Ontario*

A thesis submitted in partial fulfillment of the requirements for the Master of Science degree in Medical Biophysics

© Timothy J. Hunter 2022

Follow this and additional works at: <https://ir.lib.uwo.ca/etd>



Part of the [Medical Biophysics Commons](#)

Recommended Citation

Hunter, Timothy J., "Atrial Fibrillation and Cognitive Decline: a Computational Hemodynamics Investigation" (2022). *Electronic Thesis and Dissertation Repository*. 8824.
<https://ir.lib.uwo.ca/etd/8824>

This Dissertation/Thesis is brought to you for free and open access by Scholarship@Western. It has been accepted for inclusion in Electronic Thesis and Dissertation Repository by an authorized administrator of Scholarship@Western. For more information, please contact wlsadmin@uwo.ca.

Abstract

Background: Atrial fibrillation (AF) is a prevalent cardiac disease which has been associated with increased risk of dementia and cognitive decline. We hypothesize that atrial fibrillation leads to regional transient hypoperfusion events in the brain, and that geometric variations in the arterial structure called the Circle of Willis (CoW) play a role in these events.

Methods: A computational model was developed to simulate cerebral blood flow in six common variations of the CoW. Risk was assessed based on frequency of beat-wise regional hypoperfusion events during AF, and sensitivity analysis was performed with respect to this model output.

Results: A key artery in the CoW, called the A1 segment, was found to play the most important role in cerebral perfusion. Intrinsic heart rate was also found to influence the frequency of hypoperfusion events.

Conclusions: Our results suggest that heart rate and CoW geometry play important roles influencing cerebral hemodynamics during AF.

Keywords

Reduced order modelling, cerebral blood flow, hemodynamics, Circle of Willis, atrial fibrillation, cognitive decline.

Summary for Lay Audience

Atrial fibrillation is a common cardiac illness characterized by irregular and dysfunctional beating of the heart. We know that patients suffering from atrial fibrillation often have an increased risk of early cognitive decline; however, the mechanism underlying this risk is not well understood. We hypothesize that atrial fibrillation reduces blood supply to the brain, which means the brain receives less than normal amounts of food and oxygen. To help our future experiments and clinical trials, this study developed a computer model that could test our hypothesis. It is designed to help us better understand how atrial fibrillation affects blood supply to the brain. The model can also help the study of varying shapes and sizes of large arteries in the brain. The results of these simulations show that atrial fibrillation leads to adverse low blood flow events in the brain. Moreover, it was found that the heart rate has a large impact on how often these events occur. A lower heart rate resulted in fewer harmful events. Finally, it was found that geometric configuration of cerebral arteries plays an important role in the severity of low blood flow events caused by atrial fibrillation, and patients with a “missing A1” configuration are at highest risk for these adverse events.

Co-Authorship Statement

Chapter 2 of this text is based on the journal article titled “Atrial Fibrillation and Anterior Cerebral Artery Absence Reduce Cerebral Perfusion: A de Novo Hemodynamic Model” authored by Hunter, T. J.; Joseph, J.J.; Anazodo, U.; Kharche, S.R.; McIntyre, C.W.; Goldman, D.

Author contributions to this work were as follows: Conceptualization, T.J.H., S.R.K. and D.G.; Methodology, T.J.H. and S.R.K.; Software, T.J.H. and J.J.J.; Formal Analysis, T.J.H.; Original draft, T.J.H.; Final manuscript, T.J.H, U.A., C.W.M., and D.G.; Visualization, T.J.H.; Supervision, D.G. and C.W.M.; Project Administration, S.R.K.; Funding acquisition, C.W.M., D.G., and S.R.K.

Acknowledgments

Countless people supported my effort on this thesis. I will start by thanking my supervisors, Professors Daniel Goldman and Christopher W. McIntyre, for their infinite support, patience, invaluable feedback, and overall sense of humour. I am indebted to my advisor Dr. Sanjay R. Kharche for providing mentorship and technical training in the interdisciplinary field of computational hemodynamic research. I thank my advisor Dr. Udunna Anazodo for providing motivation, insights and expertise for this thesis. I appreciate Professor Christopher G. Ellis allowing me to work on related projects during this period which expanded my knowledge in hemodynamic phenomena.

I thank my parents, John and Andrea Hunter, for their unwavering and unquestioning support during this period of my life, for the countless meals they prepared for me, and for keeping me comfortably housed. I am eternally grateful to my friend Omi, who gave me encouragement, motivation, advice, and love throughout the course of my graduate studies. I am appreciative of my friends who saw me grow and stayed by my side throughout this journey.

I am grateful to the lands on which this work has taken place and acknowledge that I am a settler here. I have lived and worked in the city of Mississauga, ON which is part of the Treaty and Traditional Territory of the Mississauga's of the Credit First Nation, The Haudenosaunee Confederacy the Huron-Wendat and Wyandot Nations; as well as the city of London, ON, which is situated on the traditional lands of the Anishinaabek, Haudenosaunee, Lūnaapéewak, and Attawandaron.

I will take this opportunity to extend my gratitude to the Department of Medical Biophysics and Western University, as well as their excellent faculty and staff.

Table of Contents

Abstract	ii
Keywords	ii
Summary for Lay Audience	iii
Co-Authorship Statement	iv
Acknowledgments	v
List of Figures	viii
List of Tables	xi
List of Acronyms and Abbreviations	xii
Chapter 1. General Introduction	1
1.1. Physiological Background	1
1.1.1. <i>Blood Flow in the Brain</i>	1
1.1.2. <i>Pathophysiology</i>	5
1.2. Modelling Background	8
1.2.1. <i>Clinical Significance of Mathematical Modelling</i>	8
1.2.2. <i>Theory and Mathematics Behind Lumped Parameter Modelling</i>	9
1.2.3. <i>Current Landscape of Computational Modelling</i>	17
1.3. Motivation and Thesis Aims	19
1.3.1. <i>Current Gap in Knowledge</i>	19
1.3.2. <i>Hypothesis and Aims</i>	19
1.3.3. <i>Overview of What Was Achieved</i>	19
1.4. References	20
Chapter 2. Computational Modelling of Cerebral Hemodynamics During Atrial Fibrillation: A Lumped Parameter Approach	24
2.1. Introduction	24
2.2. Methods	26
2.2.1. <i>Model Components</i>	26
2.2.2. <i>Atrial Fibrillation</i>	32
2.2.3. <i>Numerical Methods</i>	33
2.2.4. <i>Hemodynamic Differences in CoW Variants</i>	34
2.2.5. <i>Sensitivity Analysis</i>	35
2.3. Results	37
2.4. Discussion	44
2.5. References	48
Chapter 3. General Discussion and Conclusions	51
3.1. Discussion of Chapter 2 Results	51
3.1.1. <i>Hypoperfusion Events</i>	51
3.1.2. <i>Subclinical Cerebral Ischemia</i>	52
3.1.3. <i>Hemodynamic Variability Between CoW Variants</i>	53
3.1.4. <i>Sensitivity Analysis</i>	54
3.2. General Conclusions and Reflections	58
3.3. Future Work	59

3.3.1. <i>Application of Model in Basic Science Research</i>	59
3.3.2. <i>Applications of Model in Clinical Research</i>	60
3.4. References	61
Appendices	66
A1. Model Parameter Table	66
A2. List of Hemodynamic Simulations Research Landscape	69
A3. Code Availability	71
A4. Open-Source Intracranial Aneurysm CFD Modelling Workflow	72
A4.1. <i>Intracranial Aneurysms</i>	72
A4.2. <i>Aneurysm Structures</i>	75
A4.3. <i>Boundary Conditions</i>	77
A4.4. <i>Finite Element Meshing</i>	83
A4.5. <i>Steady State and Transient Simulations</i>	85
A4.6. <i>Postprocessing</i>	90
A4.7. <i>Applications</i>	90
Appendix References	91
Curriculum Vitae	96

List of Figures

Figure 1. The Circle of Willis is shown as red tubes that are surrounded by cerebral white and grey matter. Individual Circle of Willis arteries are labelled. This thesis investigated the role of each artery in the Circle of Willis in the presence of cardiac atrial fibrillation.3

Figure 2. Diagram of two hearts comparing normal sinus rhythm to atrial fibrillation. A) On the left is a healthy heart under normal sinus rhythm with organized propagation of electrical signals (depicted as yellow arrows), and a rhythmic electrocardiogram to the right. B) On the left is a heart under atrial fibrillation with disorganized and spontaneous electrical impulses, and on the right is a corresponding electrocardiogram with an unsteady and erratic signal. Figure inspired by (<https://www.mayoclinic.org/diseases-conditions/atrial-fibrillation/symptoms-causes/syc-20350624>).7

Figure 3. Illustration of the effects of a first-order filter (e.g., the basic Windkessel model) on a periodic (sinusoidal) signal and a step function signal. The top panels represent the input function to the first order filter. The bottom panels illustrate the output of first order filters with varying time constants. The time constant is represented by tau in seconds. The left panels show the effect on a sinusoidal function, and the right panels show the effect on a step function.11

Figure 4. Illustration of a Windkessel electrical analogue representation of a blood vessel. Blood flows from left to right. Sawtooth lines represent resistances, the two parallel lines represent a capacitor and circles represent pressure nodes. The left-hand side resistance represents the proximal viscous resistance. The capacitance represents the ability of the blood vessels to store blood due to its tone. The right-hand side distal resistance represents the distal viscous resistance. P_{n-1} , P_n , and P_{n+1} represent the upstream (proximal), inside Windkessel element, and downstream (distal) pressures that drive flow through the element.13

Figure 5. Electrical analogue of whole-body blood flow model. The green shaded area (top) represents the cerebral circulation, including the complete Circle of Willis, distal circulation, and cerebral spinal fluid compartment, which are further detailed in Figure 6. The red shaded region (middle) represents the heart, including the four pumping chambers of the heart and valves, as well as an aortic compartment. The blue shaded region (bottom) represents the systemic circulation, including splanchnic, kidney, legs, upper body, lungs, and venous circulation. The symbols represent electrical elements shown in the figure legend.27

Figure 6. Electrical analog diagram of the cerebral circulation module. All resistances and capacitances are labeled, values and descriptions for which are given in Appendix A1. P_A is the inlet, given as the arterial pressure value from the systemic model. P_v is the outlet, given as superior vena cava pressure from the systemic model.29

Figure 7. Caricature of the complete Circle of Willis. Blood flows into the Circle of Willis through the internal carotid arteries (ICA) and the basilar artery (BA). RA: Right anterior artery; LA: left anterior artery; RM: right middle artery; LM: left middle artery; RP: right posterior artery; LP: left posterior artery; ACA1: pre-communicating anterior cerebral artery; PCoA: posterior communicating artery; and PCA1: pre-communicating posterior cerebral artery.31

Figure 8. Caricature representations of all the common CoW variants. Variant 1 has all CoW vessels. Variant 2 has a missing posterior communicating artery (PCoA). Variant 3 has both missing PCoAs. Variant 4 has a missing precommunicating anterior cerebral artery, ACA1, segment. Variant 5 has a missing precommunicating posterior cerebral artery, PCA1, segment. Variant 6 has a missing PCoA and contralateral PCA1 segment.	32
Figure 9. Stochastic RR interval assignment. Top row: Probability distribution functions for sampled RR intervals in normal sinus rhythm (A), and AF (B) at shown heart rates. C: Sampled RR intervals with mean of 70 bpm over the span of 5000 beats under NSR (blue line) and AF (red line) conditions.	34
Figure 10. Hemodynamic outputs of a simulation of AF (red) and NSR (blue) at 70 bpm in the normal CoW. A: Aortic blood pressures. Under NSR the heart rate is stable giving rise to periodic aortic blood pressure. In contrast, under AF the heart rate is erratic that may promote a disproportionate loss of aortic blood pressure. B: Blood flow through the left middle distal artery with hypoperfusion events shown in black. A typical hypoperfusion event is shown with horizontal black lines overlaid on the AF related flow (red lines) whenever perfusion was below the 5 th percentile threshold that was considered as a hypoperfusion event.	38
Figure 11. A grid of bar charts, in which each panel shows the number of hypoperfusion events found at a range of heart rates in a particular CoW variant. Each Cow variant was simulated for 5000 heart beats at each heart rate from 50 to 130 bpm.	39
Figure 12. Histograms of beat-wise mean flow distributions in NSR and AF. Flow distributions are taken from flow to the left medial region. The top panel shows distributions for the NSR case, and the bottom shows distributions for the AF case. Three CoW variants are represented: variant 1 (complete CoW) in blue, variant 4 (missing A1) in orange, and variant 5 (missing P1) in green.	41
Figure 13. Perfusion to various parts of the brain, represented by outflow at three distinct vessel terminals. In all panels, black lines show blood flow rate in the left posterior (LP) region, blue lines show blood flow rate in the left anterior (LA) region, and red lines show blood flow rate in the left medial (LM) region. Blood flow rate was normalized by the mean flow rate for the respective regions. A: complete CoW. B: missing PCoA. C: Missing both PCoAs. D: Missing A1. E: missing P1. F: missing PCoA and P1.	43
Figure 14. PRCC values for hypoperfusion count for each of the 6 considered CoW variants. The 5 PRCC values with the greatest magnitude are shown for each case and are ordered from greatest to least magnitude. Symbols are described in Table 2.	44
Figure 15. Basic visualization of 9 geometries selected from the Aneurisk dataset. All selected geometries contain at least one aneurysm on the MCA.	76
Figure 16. Basic visualization of 9 geometries selected from the Aneurisk dataset. All selected geometries contain at least one aneurysm on the MCA.	77
Figure 17. Visualization of FE mesh of an aneurysm geometry. The aneurysm is enlarged for increased visibility of the tetrahedral mesh elements on the aneurysm surface.	84
Figure 18. Wall shear stress magnitudes mapped on to an intracranial aneurysm geometry. Wall shear stress values are derived from velocity vectors which are outputs of the CFD simulation. The results shown are from a steady state simulation with constant flow rate imposed at the inlet.	86

Figure 19. Plot of the volumetric flow rate (Q) versus time (t) at the inlet boundary. Four key timepoints are marked for reference by following figures. This flow profile has been scaled to the surface area of the inlet of case C0019 according to previously mentioned scaling laws. The waveform spans 0.86 seconds, which was taken as the length of a heartbeat. In practice, the waveform repeats periodically. A-B are respectively diastolic flow rate, systolic flow rate, trough of the dicrotic notch, peak of the dicrotic notch.87

Figure 20. Wall shear stress is shown on aneurysm geometry at four key timepoints during a transient simulation. Wall shear stress magnitude is indicated both by arrow size and by colour. A-D reference key timepoints in the cardiac cycle which are shown in Figure 19.88

Figure 21. Blood velocity fields are shown within aneurysm geometry at four key timepoints during a transient simulation. Velocity vector direction is indicated by arrow direction. Velocity magnitude is indicated both by arrow size and by colour. A-D reference key timepoints in the cardiac cycle which are shown in Figure 19.....89

Figure 22. Oscillatory shear stress (OSI) mapped on to an intracranial aneurysm geometry. OSI values are derived from transient velocity vectors over the course of a single cardiac cycle which are outputs of the CFD simulation.90

List of Tables

Table 1. Coefficients for the 6th order BDF formula.	17
Table 2. Model parameters relevant to PRCC analysis.	36
Table 3. Model output statistics under NSR conditions.	37
Table 4. All relevant baseline model parameters for the lumped parameter cerebral model detailed in Chapter 2.	68
Table 5. A compiled list of studies focussing on hemodynamic simulation. Studies are divided by modelled dimensionality (i.e., 0D, 1D or 3D). The table includes the purpose of the study, and the platform used.	70
Table 6. Inlet cross sectional area and derived inlet flow rate. C: cerebral geometry from Aneurisk repository. ICA: Internal carotid artery. Q: blood flow rate (ml s^{-1}).	79
Table 7. Outlet boundary condition data for each aneurysm geometry. All values are shown are in ($\times 10^4 \text{ dynes s cm}^{-5}$). M2: second segment of middle cerebral artery. ACA: Anterior cerebral artery. AChA: Anterior choroidal artery. ACoA: Anterior communicating artery. PCoA: Posterior communicating artery. OpthA: Ophthalmic artery.	83
Table 8. Mesh properties of all 20 analyzed cases.	85

List of Acronyms and Abbreviations

0D	Zero Dimensional
ACA	Anterior Cerebral Artery
ACoA	Anterior Communicating Artery
AF	Atrial Fibrillation
BPM	Beats Per Minute
C	Capacitance
CBF	Cerebral Blood Flow
CFD	Computational Fluid Dynamics
CoW	Circle of Willis
ICA	Internal Carotid Artery
LA	Left Anterior
LM	Left Medial
LP	Left Posterior
MCA	Middle Cerebral Artery
NSR	Normal Sinus Rhythm
ODE	Ordinary Differential Equation
P	Pressure
PCA	Posterior Cerebral Artery
PCoA	Posterior Communicating Artery
Q	Flow Rate
R	Resistance
RA	Right Anterior
RCR	Resistor-Capacitor-Resistor
RM	Right Medial
RP	Right Posterior

Chapter 1. General Introduction

The brain is the most intriguing organ in the human body. With its 100 billion neurons, trillions of glial cells, it is what many say sets us apart from the rest of the animal kingdom. The neurons, glial cells, and other tissues are kept alive by blood vessels traversing the brain. You are constantly using your brain, engaging your motor cortex to pick up a cup of coffee, or your language centers to process a thesis dissertation. Your brain plays a role in nearly every aspect of your life, which is why it is critical to maintain its health.

1.1. Physiological Background

1.1.1. Blood Flow in the Brain

The brain consumes an average of 20% of the total body's energy, despite accounting for only 2% of its mass [1]. The brain receives approximately 15% of cardiac output, with average cerebral blood flow levels as high as 50 mL/100 g/min [2,3]. Gray matter has an even higher average demand at 80 mL/100 g/min, while white matter requires around 20 mL/100 g/min. Glucose is the main energy substrate used by the brain except during extreme periods of starvation or hyperglycemia where ketones are used as an alternative energy source. The brain has very little capacity for storage of energy substrates, and therefore it requires a continuous blood supply. Oxygen (aerobic metabolism) and glucose (glycolysis) are both supplied to the brain via the blood through the cardiovascular system. The energy requirements for the brain can be compartmentalized to basal and functional needs. Basal energy is required for maintenance of cell integrity with electrochemical gradients; cellular transport of molecules; synthesis of proteins, lipids, and carbohydrates; and the production, storage, release, and reuptake of transmitters. Functional energy is expended in neuronal functioning including generation of electrical activity by the pyramidal cells. About 40% of the energy is used for basal needs, while functional activity consumes about 60%.

The cardiovascular system supplies nutrients to all tissues in the body by a combination of two transport mechanisms. The first mechanism is convective transport. This is where blood is transported through arteries along a pressure gradient from high to low. High pressures are generated via the pumping action of the heart, and valves within the heart cause the blood to flow out in the direction of the arteries. Blood flows along the pressure gradient through the network of arteries, to arterioles, capillaries, then venules, veins and eventually back to the heart. Blood is also circulated between the pulmonary system, where it becomes enriched in oxygen. The heart then pumps the oxygen enriched blood into the systemic circulation, where it deposits the oxygen and circulates other nutrients. The network of blood vessels is crucial to allow blood to perfuse the tissues, flowing in capillaries within microns from any point in the body which brings us to the second mechanism of diffusive transport. This small distance is necessary to allow diffusive transport between the blood and tissues. Diffusive transport is the movement of particles through a medium down a concentration gradient. In the case of nutrient delivery, this means oxygen and glucose diffusing out of the blood in the capillaries into the cells which consume them.

In addition to the brain having relatively high metabolic demands, it is also very sensitive to ischemic damage. Cessations or alterations to cerebral blood flow (CBF) can have devastating consequences for cognitive functioning [4], therefore there are several mechanisms in place to maintain CBF at healthy levels. The first of these mechanisms is collateral vessels. Blood flow in the brain is highly collateralized, meaning that blood to one region may be supplied by several vessels (Figure 1). The two common carotid arteries (anterior circulation) and the two vertebral arteries (posterior circulation) supply blood to the anterior and posterior parts of the brain respectively. The internal carotid arteries (ICA) supply the brain and eyes. In general, the size of the area supplied by the artery determines the diameter of the cerebral artery [5]. The ophthalmic, posterior communicating (PCoA), anterior choroidal, anterior cerebral (ACA), and middle cerebral (MCA) arteries are all branches of the ICA, and the majority of blood flow to the cerebrum comes from these branches. All the areas supplied by these vessels generally have adequate collateral vessels to protect against occlusions, except the middle cerebral artery, and as a result the MCA territory is at higher risk of ischemia than other regions of the brain.

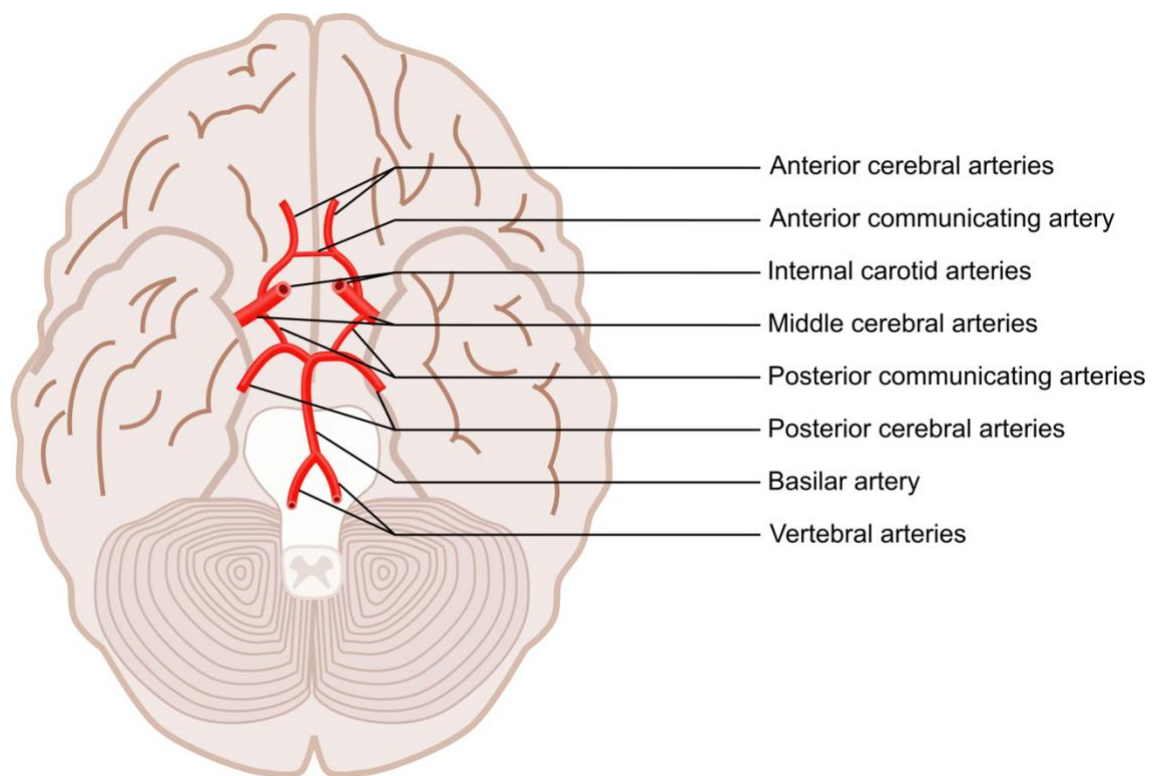


Figure 1. The Circle of Willis is shown as red tubes that are surrounded by cerebral white and grey matter. Individual Circle of Willis arteries are labelled. This thesis investigated the role of each artery in the Circle of Willis in the presence of cardiac atrial fibrillation.

The posterior circulation is fed from two vertebral arteries, which conjoin into the basilar artery. Branches from these arteries supply blood to the cerebellum and brainstem, before bifurcating into the posterior cerebral arteries, which supply the posterior cerebrum. The posterior communicating arteries (PCoA) connect posterior cerebral arteries to the carotid circulation.

The Circle of Willis (CoW) represents an anastomosis of the basal cerebral arteries and the potential collateral circulation. This ring-shaped structure allows collateral flow to any of the major cerebral arteries. It is composed of the anterior communicating segments (ACoA) which connect the left and right ACAs; and the two PCoAs, which connect each posterior cerebral artery to the ipsilateral MCA. However, the complete CoW pattern is found in less than 50% of people; the ACoA and PCoA are frequently missing congenitally, or

hypoplastic. While the main function of the CoW structure is to supply collateral blood flow to areas of the brain which may be receiving decreased perfusion, missing or hypoplastic vessels may restrict this function.

CBF is also maintained by a system of regulatory mechanisms that ensure sufficient nutrients are delivered to all regions of the brain. This is achieved in the cerebral circulation by modulating the vascular resistance in order to maintain adequate perfusion in response to changing perfusion pressures and metabolic demands. Vascular resistance is dependent only on hematocrit, vessel length, and vessel radius, and because the first two of these remain effectively constant over short periods of time, blood flow is controlled by altering the vessel radius, also called vascular tone. According to Poiseuille's law vascular resistance (R) is inversely proportional to vessel radius (r) to the fourth power,

$$R = \frac{P}{Q} = 8 \frac{\mu L}{\pi r^4} \quad \text{Equation 1}$$

Where P is pressure difference across a vessel segment, Q is flow rate, μ is fluid viscosity, and L is vessel length. Therefore, even small changes to the vessel radius result in large changes to vascular resistance. Passively, vessel radius will decrease when blood pressure decreases due to lower forces on the vessel wall. This results in higher resistance in addition to lower perfusion pressures, and a large drop off in blood flow. To combat this passive effect, vessel tone is actively modulated in response to blood flow levels, acting in contrast to the passive effect.

Vascular tone is modulated by several physiological signals, leading to precise and localized control of blood flow levels in the brain [6]. Vascular tone may be decreased (i.e., dilation) in response to hypoxia or increased metabolic demand. This signal is thought to be in response to increased adenosine levels, which occur both in tissues experiencing low oxygenation, and tissues experiencing increased metabolic activity. The response to this signal would result in increased blood flow to tissues for which there is a local metabolic demand. Nitric oxide levels are another important physiological signal involved in the regulation of CBF.

Nitric oxide is a known vasodilator, and its production in endothelial cells is increased in response to shear stress. This means that vessels experiencing high shear stress, which is

related to blood velocity, will have decreased vascular tone, and therefore higher blood flow. Blood CO₂ levels also play a strong role in the regulation of nutrient delivery in the brain. CO₂ acts as a strong vasodilator in the brain, decreasing tone to increase blood flow to any regions with increased CO₂ levels.

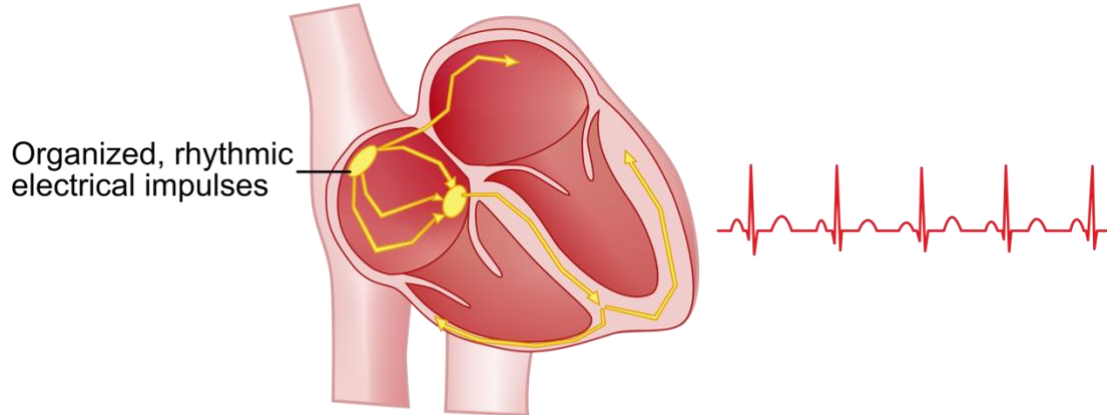
Finally, sympathetic nervous activity also plays a role in CBF regulation. The sympathetic nervous system works to maintain arterial blood pressure in the entire body by adjusting total peripheral resistance. Norepinephrine, a vasoconstrictor, is released from sympathetic nerve fibers in response to low systemic blood pressures and acts on systemic arteries and arterioles, including in the brain. The effects of metabolic, shear stress, CO₂, and sympathetic pathways in regulating CBF levels are the most widely accepted and best understood mechanism currently, however our understanding is constantly evolving, and new mechanisms and pathways may be discovered as research and methods develop.

1.1.2. Pathophysiology

Cardiac atrial fibrillation (AF) affects the upper chambers of the heart called the atria (Figure 2). During AF, the atrial contractions become erratic which manifests in the electrocardiogram as irregular R-R intervals. AF is a known comorbidity that is simultaneous to dysfunction in other organs including the brain [7]. The bidirectional interactions between the heart and brain (called the heart-brain axis) have been widely recognized. In one direction, for example, the brain can have an impact on cardiac contractility via sympathetic and parasympathetic nervous system [7]. In the alternate direction, reductions, alterations, or irregularities in cardiac output led to adverse effects towards tissue in the brain if regulation mechanisms are unable to maintain CBF. AF has been implicated in increased risk of early onset dementia and cognitive decline [8]. AF is also associated with a fivefold increased risk for thromboembolic transient ischemic attack and stroke [9]. It has also been associated with lower total white and grey brain matter volumes [10]. The association between AF and decreased brain volume is stronger with increased arrhythmia burden and a longer duration of persistent AF [9]. It has been recently observed that AF is independently associated with cognitive decline through a range of different potential mechanisms including micro and macro embolic events [9]. Whereas the links between cardiac diseases such as AF and deleterious brain disorders are well

established, the mechanisms remain elusive. One of the main postulated mechanisms is reduced CBF due to the RR interval variability characteristic of AF, and reduction or loss of atrial systole, which leads to a reduction in stroke volume [11]. Attempts to normalize cardiac output by increasing heart rate are inefficient as tachycardia shortens the ventricular filling time, contributing to further decrease in cardiac output, and CBF. Cardioversion patients were found to have significant improvements in CBF 30 days after treatment if sinus rhythm was preserved [12,13]. Pharmaceutical rate control has been a widely used method for AF treatment, and recent computational modelling suggests that strict rate control (< 80 bpm) can reduce deleterious effects associated with RR variability in AF [11]. Patients experiencing paroxysmal AF were found to exhibit similar CBF values as those without a history of arrhythmia if measured during sinus rhythm, supporting the fact that the presence of arrhythmia at the time of imaging is of key importance [9].

A. Normal sinus rhythm



B. Atrial fibrillation

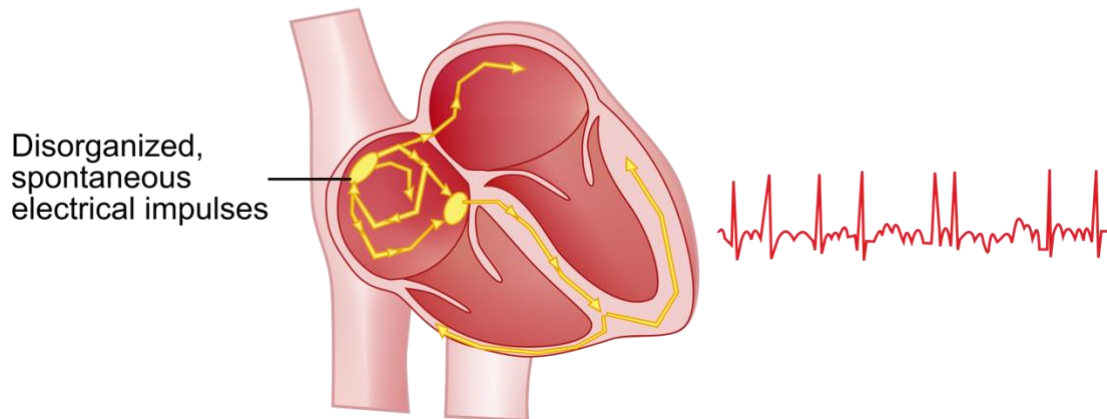


Figure 2. Diagram of two hearts comparing normal sinus rhythm to atrial fibrillation. A) On the left is a healthy heart under normal sinus rhythm with organized propagation of electrical signals (depicted as yellow arrows), and a rhythmic electrocardiogram to the right. B) On the left is a heart under atrial fibrillation with disorganized and spontaneous electrical impulses, and on the right is a corresponding electrocardiogram with an unsteady and erratic signal. Figure inspired by (<https://www.mayoclinic.org/diseases-conditions/atrial-fibrillation/symptoms-causes/syc-20350624>).

A reduction of CBF is known to be related to debilitating chronic diseases such as Alzheimer's disease [8]. Over the course of time, loss of biomechanical strength of blood vessels promotes cerebral aneurysms, vasospasm, and fatal hemorrhage. The vast clinical literature is witness to the prime relevance of cerebral blood flow's role in health and disease. However, current treatment strategies for most conditions remain suboptimal due

to poorly understood mechanisms. Basic scientific research is targeted towards understanding the mechanisms in the hope to control these diseases. One such basic science approach is of mathematical modelling which is becoming increasingly deployed in both the clinical and experimental sciences, in addition to being a field in its own merit. We believe that uncovering the relationship between cerebral anatomy (e.g., Circle of Willis) and function (cerebral perfusion, autoregulation) will permit development of novel diagnostic biomarkers that can be generated using existing imaging and clinical testing technology. The models presented in this study are expected to be deployed in ongoing clinical research.

1.2. Modelling Background

1.2.1. Clinical Significance of Mathematical Modelling

The research community's response to the ongoing pandemic has brought to light the extensive applicability of mathematical modelling to help understand disease mechanisms and to make decisions. Modelling of cerebral neurons is already an advanced field demonstrating the necessity of mathematical data interpretation and data driven prediction [14]. Similarly, the modelling-based study of cerebral blood flow is expected to generate clinically relevant knowledge and help in the research process. Cerebral disease mechanisms are heterogeneous and remain unclear, which is a severe limitation for effective and predictable patient treatment. Therefore, intense worldwide investigations into mechanisms behind diseases such as AF are being performed in a multidisciplinary multifaceted manner [15]. Finding strategies for better individualized treatment has therefore become an important goal in treatment strategy planning. In silico clinical trials are now rapidly becoming routine and offer the hope of saving volunteers, expenditure, and accelerating translation [8]. The advances in engineering and material sciences are supplemented and streamlined using modelling of treatment devices such as drug eluting stents and wire meshing [9]. However, the use of modelling is yet nascent and requires further development to enable its standardization in the clinical research environment. Additionally, some modelling techniques used in clinical research such as multi-scale

computational fluid dynamics (CFD) currently have large requirements in terms of time, computational resources, and user experience. Therefore, there is a need for computational models that can be used for clinical insight, with the capability to be run in the hospital or at the patient bedside. This thesis provides a few straightforward solutions that can be used in our London Ontario Hospitals immediately, using lumped parameter modelling.

1.2.2. Theory and Mathematics Behind Lumped Parameter Modelling

The model presented in this work is made up of a system of ordinary differential equations (ODEs) and delay differential equations (DDEs). A differential equation is an equation which relates a function of an independent variable, y , to its derivative, \dot{y} . An ODE is a special case of differential equation in which the function y only depends on one independent variable, such as time (t). This property means that ODEs can be used to show how the value of y will evolve over time given an initial value for y , without having to know the function that describes it. Complex systems may also be modelled by a system of coupled ODEs. In this case y is a vector of states, where each derivative \dot{y} may depend on one or many (inhomogeneous ODE), or none (homogeneous ODE), of the values in y . In the model developed in this thesis, the heart was considered as external pumps consisting of four chambers. In the presence of forcing terms such as the heart the system is called an inhomogeneous ODE where the system behavior is dictated by both the function of y as well as the forcing terms. The key ODEs that are used in the model are described in section 1.2.2.1, while the numerical methods used to solve ODEs are described in section 1.2.2.2.

1.2.2.1. Key Equations

Equations describing forces and mechanisms are called mechanistic models. Such equations are usually based in physical forces and mechanics. An example of mechanistic modelling is the use of the resistor-capacitor-resistor (RCR) Windkessel unit. The major benefit of this approach to modelling is its ability to predict and discover emergent behavior in a system. This is because mechanistic models depend on well understood and accepted laws of physics, and therefore model predictions are understood to be reliable. The downside to this modelling approach is that it requires a precise understanding of the

system, including any forces and mechanisms that might affect it. Practically, this means that assumptions and approximations must be made in order to fully encapsulate the behavior of the system.

Equations that calculate an expected output based on an input are called statistical or phenomenological models. Statistical models are built based on previous measurements of a system. There is no attempt in statistical modelling to describe the mechanisms occurring within a system, only to accurately describe the external behavior of the system. The benefit of this approach to modelling is that it does not require an intimate understanding or representation of the inner workings of a system. This can be very helpful when one wishes to describe a system in which all the mechanisms are not fully understood, or which would be too expensive to compute. The downside to statistical models is that they cannot predict behavior outside of the expected threshold. This is because statistical models are calibrated specifically using input and output data for a system, and therefore cannot reliably predict behavior outside the normal range.

First order filters are used in mathematical modelling to describe phenomena with damping behavior. As an ODE, a first order filter can be expressed as:

$$\frac{dy_1}{dt} = f(y_1, y_2, \tau, p, t) \quad \text{Equation 2}$$

where y_1 is the state variable, y_2 is the input to the filter i.e., some other state value, and τ is the time constant of the filter. Using an appropriate function f , the role of τ is illustrated in Figure 3. The first is a damping behavior. Depending on the time constant and the frequency of the input, oscillations in the input will be decreased in amplitude. The second behavior is a phase shift. Depending only on the time constant, input signal to the filter will be shifted in phase. ODEs of this form are used extensively in phenomenological and mechanistic models. In the presented model, ODEs such as Equation 2 are used extensively to describe the dynamics of the baroreceptor mechanism, as well as the cerebral autoregulation mechanism, using blood pressures and flows to determine some physiological blood pressure and flow signals.

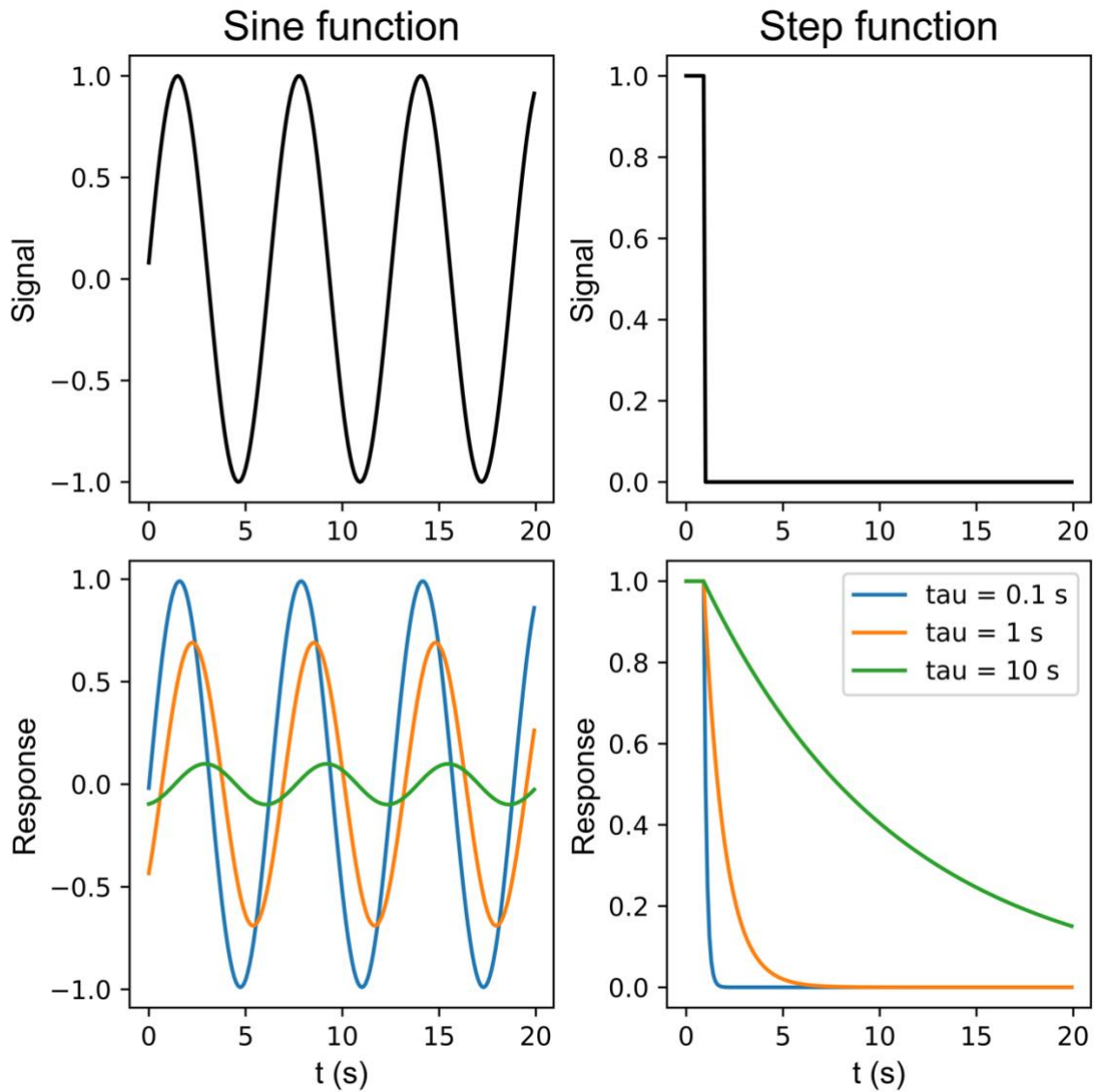


Figure 3. Illustration of the effects of a first-order filter (e.g., the basic Windkessel model) on a periodic (sinusoidal) signal and a step function signal. The top panels represent the input function to the first order filter. The bottom panels illustrate the output of first order filters with varying time constants. The time constant is represented by tau in seconds. The left panels show the effect on a sinusoidal function, and the right panels show the effect on a step function.

Electrical analogs based upon the Windkessel effect are used extensively in lumped parameter modelling of the cardiovascular system (Figure 4). The Windkessel effect refers to the similarities between a blood vessel or network, and an elastic reservoir [16]. The walls of blood vessels (excluding capillaries) contain elastin making them elastic. Blood

vessel walls expand and recoil when blood pressure in the lumen increases or decreases respectively. The expansion and recoil of the walls occur over characteristic time scales, represented by tau in Eq. 2, that allows the vessels to store some volume of blood over each heartbeat. Additionally, as blood flows through the vessels, it is subject to viscous forces, which decreases its pressure proportionally to its velocity. In the electrical analogy, the flow of blood through a vessel is likened to the flow of electrons through a wire, i.e., current, and the blood pressure is likened to the potential electric energy, i.e., voltage. In this analogy, a resistor element represents the viscous resistance to blood flow through a vessel, and a capacitor represents the compliance of the vessel. The 2-element Windkessel unit was formulated by Frank [17] as a circuit with a single capacitor and a single resistor. In this formulation, the resistance R was equal to the total peripheral resistance of the systemic circulation, given by:

$$R = \frac{(P_{ao,mean} - P_{ven,mean})}{CO} \quad \text{Equation 3}$$

With $P_{ao,mean}$ and $P_{ven,mean}$ being mean aortic and venous pressure respectively, and CO being cardiac output. The value for the capacitance C is given as the ratio of the change in volume ΔV over the corresponding change in blood pressure ΔP :

$$C = \frac{\Delta V}{\Delta P} \quad \text{Equation 4}$$

The 2-element model provides a reasonable description of the arterial pressure in systole and diastole, as well as cardiac output, however over time it was found that the model provided inaccurate pressure-flow relation during systole [18–20].

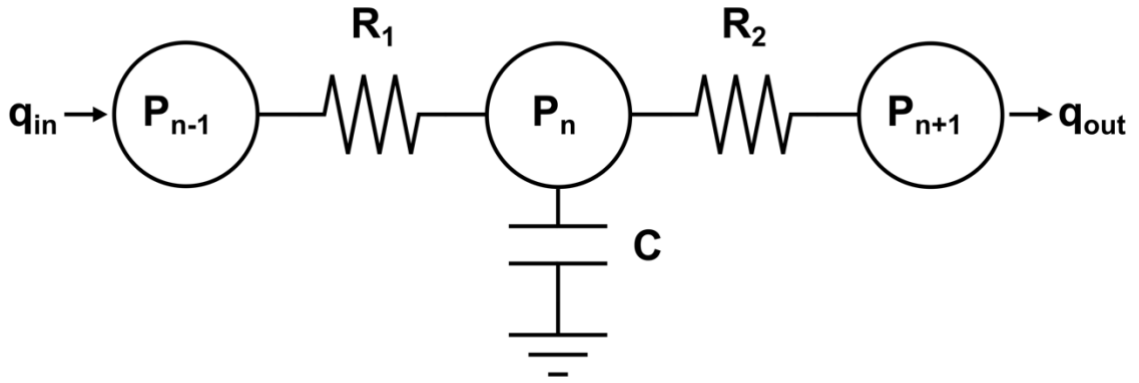


Figure 4. Illustration of a Windkessel electrical analogue representation of a blood vessel. Blood flows from left to right. Sawtooth lines represent resistances, the two parallel lines represent a capacitor and circles represent pressure nodes. The left-hand side resistance represents the proximal viscous resistance. The capacitance represents the ability of the blood vessels to store blood due to its tone. The right-hand side distal resistance represents the distal viscous resistance. P_{n-1} , P_n , and P_{n+1} represent the upstream (proximal), inside Windkessel element, and downstream (distal) pressures that drive flow through the element.

This shortcoming was overcome by adding a characteristic impedance element to the unit as shown in Figure 4, which represents a link to pulse wave dynamics in the aorta [21,22]. The characteristic impedance Z_c has the same units as resistance, and is given by:

$$Z_c = \text{PWV} \cdot \frac{\rho}{A} \quad \text{Equation 5}$$

where PWV is the pulse wave velocity, ρ is the blood density, and A is the cross-sectional area of the proximal aorta [23]. The 3-element formulation of the Windkessel unit was found to provide accurate pressure and flow predictions in the aorta throughout the entire cardiac cycle. Therefore the 3-element model suffices to describe global pressure and flow for most studies [24]. The use of a resistor element for the characteristic impedance also causes small errors in the low frequency range of the impedance, which has led to the introduction of a 4-element Windkessel unit [25–27]. The value for L is often estimated based on measured data because there is no simple measurable phenomena from which to derive it, and even so it has been found difficult to estimate [23].

As an extension of the principles of the Windkessel model, it has become common to model the cardiovascular system as a network of connected Windkessel units. This is done so that pressure and flow waveforms may be studied in local regions of the circulation, rather than only the global arterial pressure. The network model also allows for additional mechanisms to be applied to local regions of the circulation, such as resistance and compliance modulation from the baroreceptor mechanism or cerebral autoregulation. Models of this form frequently utilize the 3-element Windkessel units, with the formulation for flow as follows:

$$q = \frac{P_{n-1} - P_n}{R} \quad \text{Equation 6}$$

With P_{n-1} and P_n being pressure at adjacent nodes. Pressure at each node is described by the following:

$$\frac{dP}{dt} = \frac{q_{in} - q_{out}}{C} \quad \text{Equation 7}$$

Where q_{in} and q_{out} are the sums of flows into and out of the pressure node respectively. The inductor element is neglected in the present work as it is primarily interested in the beat-to-beat characteristics of the pressure and velocity waveforms. In a network model, the contribution of inductors to pressures and flows is greatest in during large changes in flow, however it has been estimated that inertial effects account for less than 1% of stroke volume and mean arterial pressure [28]. Therefore, inclusion of inertial effects would serve only as cosmetic improvement to the pressure and flow waveforms, while nearly doubling the computational cost due to an additional ODE per inductor.

1.2.2.2. Numerical Methods

A system of ODEs shows how a system will progress in time from a set of initial conditions. The problem of deriving this solution is aptly called the initial value problem (IVP). These problems are solved by a variety of numerical strategies which can be executed using a computer, thus extending their value from theoretical research to clinical applications by the patient bedside. The numerical methods to be discussed below are the explicit forward Euler method, the implicit backward Euler method, and finally a family of implicit methods

called the backwards differentiation formula (BDF) of which the backward Euler method is a member.

The forward Euler method is the simplest and the most intuitive of the numerical methods. It is explicit, meaning that it calculates the state of the system at a later time, based on the state of the system at the current time. The solution for $y(t)$ is therefore calculated in steps, iterating over values of t with a suitably small time step size of Δt . The size of Δt determines the accuracy of the solution, with smaller sizes being more accurate. Conversely, smaller Δt leads to more computations over the span of t and a more expensive computation in total. The solution using the forwards Euler method is as follows. Let us consider an IVP for the generic ODE

$$\dot{y}(t) = f(t, y), \quad y(t_0) = y_0 \quad \text{Equation 8}$$

and let $t_i, i = 0, 1, 2, \dots$ be a sequence in time for which $t_{i+1} = t_i + \Delta t$. Let Y_i be the approximate solution to $y(t_i)$. The differential equation (Equation 8) is used to obtain Y_{i+1} . The slope at the point (t_i, Y_i) is given by $f(t_i, Y_i)$. The forward Euler method determines the successive point (t_{i+1}, Y_{i+1}) by assuming it lies on the line through (t_i, Y_i) with slope of $f(t_i, Y_i)$, given by the equation:

$$\frac{Y_{i+1} - Y_i}{\Delta t} = f(t_i, Y_i) \quad \text{Equation 9}$$

which, when rearranged, gives

$$Y_{i+1} = Y_i + f(t_i, Y_i) \cdot \Delta t \quad \text{Equation 10}$$

Iterating this formula through t_i , starting with the known initial value y_0 , therefore yields the approximate solution to $y(t)$. However, physiological models of the brain and heart are often stiff involving multiple timescales. The explicit Euler method is often unstable and leads to erroneous numerical solutions [29]. In addition, methods such as Eq. 10 must obey a restrictive Courant-Frederich-Levy condition which restricts the choice of Δt severely. Therefore, stable, and accurate methods are a necessity for the model developed in this thesis.

The backwards Euler method is an implicit method, meaning the unknown point (t_{i+1}, Y_{i+1}) is computed using the slope $f(t_{i+1}, Y_{i+1})$, contrary to the explicit method which

used the slope at $f(t_i, Y_i)$. The backward Euler method computes the successive point by assuming that the current point (t_i, Y_i) lies on the line through (t_{i+1}, Y_{i+1}) with slope $f(t_{i+1}, Y_{i+1})$, given by the equation:

$$\frac{Y_{i+1} - Y_i}{\Delta t} = f(t_{i+1}, Y_{i+1}) \quad \text{Equation 11}$$

Which, when rearranged, gives:

$$Y_{i+1} = Y_i + f(t_{i+1}, Y_{i+1}) \cdot \Delta t \quad \text{Equation 12}$$

The solution is therefore a value for Y_{i+1} which satisfies the above equation, which may be computed using any root-finding algorithm [30]. The implicit method requires additional iterative computation relative to the forward Euler method but comes at the advantage of increased stability. However, a single step implicit Euler method is restrictive to the integration timestep. The timestep restrictions cause the simulations to consume significant compute time thus limiting the user's ability to perform meaningful computer experiments, especially when solutions are sought in real time. The current numerical methods technology provides significantly more accurate and stable routes to perform the large simulations efficiently. Current methods also provide the key practical option of adaptive time stepping that permits users to perform large to very large (many) simulations. These current methods use the backwards difference formula.

The backwards difference formula (BDF) is a family of methods for determining the solution to a system of ODEs. The BDF uses information from previously computed values of Y_i to determine the next value. The general formula for a BDF is [31]:

$$\sum_{k=0}^s a_k Y_{i+k} = \beta f(t_{i+1}, Y_{i+1}) \cdot \Delta t \quad \text{Equation 13}$$

Where the coefficients a_k and β are derived using the Lagrange polynomial $p_{n,s}(t)$ for the points $(t_i, Y_i), \dots, (t_{i+s}, Y_{i+s})$, which is beyond the scope of this work. It can be seen that the backward Euler method is a member of the BDF family with $s = 1$. The advantage of using higher order, i.e., higher values for s , is that using more information for the integration of the slope yields higher accuracy, as well as increased stability for the

solution. The BDF used to integrate the system of ODEs in the present work had $s = 6$; with coefficients found in Table 1.

a_0	$10/147$
a_1	$-72/147$
a_2	$225/147$
a_3	$-400/147$
a_4	$450/147$
a_5	$-360/147$
a_6	1
β	60

Table 1. Coefficients for the 6th order BDF formula.

1.2.3. Current Landscape of Computational Modelling

Mathematical modelling has been a key aspect of cardiovascular research since before widespread use of computers. Key works that still hold great weight in the present research landscape include Krogh’s description of oxygen delivery in microvasculature [32] and Franks formulation of the Windkessel effect and contribution to the Frank-Starling mechanism [17, 33], among others.

The introduction of computers has allowed for the expansion of this theoretical foundation, as well as the development of broad new experimental and clinical applications. Guyton [34] presented a model of human circulation which encompassed a vast number of mechanisms (354 “blocks”) and was based on a systems analysis and experimental data on the human cardiovascular system. Suga et al. developed a mathematical description of the beating heart which is still used widely to this day [35]. Many of the extensions of to the Windkessel model described in Section 1.2.2.1 were made possible by increasing accessibility of computers [23].

Increasingly useful and applicable models continue to be developed, reaffirming that lumped parameter modelling continues to hold an important place in medical research. An

accurate and highly performant model of blood flow in the systemic circulation was developed by Heldt [36]. Cardiac valve dynamics have been described mechanistically with broad clinical applications. Cerebral circulation has been modelled by Ursino et al. [37] for the study of lumped cerebral hemodynamics in the CoW. A geometrically limited, but more functionally encompassing description of CBF with regulation mechanisms has also been proposed by Spronck et al. [38]. There is a wealth of mathematics and theory that can be applied and expanded for experimental and clinical use in a wide variety of areas.

Additionally, brain blood flow has been modelled extensively in 3D by multiple research groups in Canada and worldwide. Using an advanced software [39], the Marsden group investigate multiple blood flow phenomena including those in the brain. Their computational fluid dynamics simulations (CFD) are primarily imaging driven and in 3D, which makes them informative and detailed in nature. Steinman et al. [40] routinely investigate cerebral flow dynamics under pathophysiological conditions. Their work is often driven by medical images and thus promises to be of diagnostic utility [41]. It has been shown that there is a close link between cerebral vessel geometry (anatomy) and the blood flow hemodynamics in it [42]. The importance of computer modelling to predict outcomes of medical treatments has been demonstrated by Taylor et al. [43]. In particular, Taylor et al. have been instrumental in establishing the CFD methods in relation to human blood flow modelling [44,45]. Another robust library called CRIMSON has been developed by Figueroa et al. [46] and used extensively to study cerebral CFD driven by clinical imaging [47]. Spatially extended 3D modelling is resource intensive with simulations requiring over 2 days on several processors. The information gain from 3D modelling is uncertain in the early stages of any study. In addition, 3D models have several parameters that cannot be informed by measurements introducing an inherent uncertainty in the workflow. To rectify the issues to a certain extent, this thesis focuses on reduced order modelling i.e., lumped parameter modelling.

1.3. Motivation and Thesis Aims

1.3.1. Current Gap in Knowledge

Previous modelling studies form the basis for the present work, however the role of cerebral vascular structural variants, i.e., CoW variants, in AF-cerebral perfusion relationship remains underexplored. As the CoW is known to play an important role in the distribution of blood flow to the brain, variants which are present in a large portion of the population should be considered while studying the interplay between AF and cerebral hemodynamics.

1.3.2. Hypothesis and Aims

The hypothesis of this thesis was:

- a) specific blood vessels in the brain affect overall cerebral blood flow; and
- b) feedback mechanisms such as autoregulation may explain recent clinical observation.

The aims of this thesis were to:

- a) develop an open-source lumped parameter model of cerebral blood flow pathophysiology to permit experimentally-clinically relevant investigations; and
- b) apply the model to uncover the role of Circle of Willis anatomy variants on cerebral blood flow in the presence of atrial fibrillation (Chapter 2).

1.3.3. Overview of What Was Achieved

In this work, a composite 0D model of human circulation, including a detailed cerebral vasculature and functional baroreceptor feedback mechanism, was developed to discover the effects of AF on cerebral perfusion in cases with common CoW variants. Composition of the model is described briefly in section 2.2.2, and further in the appendix. The model is used to assess cerebral hemodynamics during AF in six common CoW variants. The methods and results for this assessment are given in detail in section 2.2.4 and 2.3 respectively. The model itself is also assessed using sensitivity analysis as described in

section 2.2.5, which details the parameter values which are correlated to model outcomes, and 2.3 which details the results of said analysis.

Additionally, a comprehensive pipeline for the CFD analysis of patient specific aneurysm geometries is presented in appendix 5. This pipeline uses only the free, open-source software packages SimVascular and Paraview.

1.4. References

1. Phillips, A.A.; Chan, F.H.; Zheng, M.M.Z.; Krassioukov, A. V.; Ainslie, P.N. Neurovascular coupling in humans: Physiology, methodological advances and clinical implications. *J. Cereb. Blood Flow Metab.* **2015**, *36*, doi:10.1177/0271678X15617954.
2. Vavilala, M.S.; Lee, L.A.; Lam, A.M. Cerebral blood flow and vascular physiology. *Anesthesiol. Clin. North America* **2002**, *20*.
3. Willie, C.K.; Smith, K.J. Fuelling the exercising brain: A regulatory quagmire for lactate metabolism. *J. Physiol.* **2011**, *589*.
4. Iadecola, C. The Neurovascular Unit Coming of Age: A Journey through Neurovascular Coupling in Health and Disease. *Neuron* **2017**, *96*.
5. Lehrer, H.Z. Relative calibre of the cervical internal carotid artery. *Brain* **1968**, *91*, doi:10.1093/brain/91.2.339.
6. Payne, S. Cerebral Flow in the Brain Control of Blood Autoregulation; **2016**; ISBN 9783319317830.
7. Kim, M.S.; Kim, J.J. Heart and brain interconnection - Clinical implications of changes in brain function during heart failure. *Circ. J.* **2015**, *79*, doi:10.1253/circj.CJ-15-0360.
8. De Bruijn, R.F.A.G.; Heeringa, J.; Wolters, F.J.; Franco, O.H.; Stricker, B.H.C.; Hofman, A.; Koudstaal, P.J.; Ikram, M.A. Association Between Atrial Fibrillation and Dementia in the General Population. *JAMA Neurol.* **2015**, *72*, 1288–1294, doi:10.1001/JAMANEUROL.2015.2161.
9. Gardarsdottir, M.; Sigurdsson, S.; Aspelund, T.; Rokita, H.; Launer, L.J.; Gudnason, V.; Arnar, D.O. Atrial fibrillation is associated with decreased total cerebral blood flow and brain perfusion. *EP Eur.* **2018**, *20*, 1252–1258, doi:10.1093/EUROPACE/EUX220.
10. Stefansdottir, H.; Arnar, D.O.; Aspelund, T.; Sigurdsson, S.; Jonsdottir, M.K.; Hjaltason, H.; Launer, L.J.; Gudnason, V. Atrial fibrillation is associated with reduced brain volume and cognitive function independent of cerebral infarcts. *Stroke* **2013**, *44*, doi:10.1161/STROKEAHA.12.679381.
11. Saglietto, A.; Scarsoglio, S.; Ridolfi, L.; Gaita, F.; Anselmino, M. Higher ventricular rate during atrial fibrillation relates to increased cerebral hypoperfusions and hypertensive events. *Sci. Reports 2019 91* **2019**, *9*, 1–9, doi:10.1038/s41598-019-40445-5.
12. Petersen, P.; Kastrup, J.; Videbaek, R.; Boysen, G. Cerebral blood flow before and after cardioversion of atrial fibrillation. *J. Cereb. Blood Flow Metab.* **1989**, *9*, doi:10.1038/jcbfm.1989.62.

13. Porebska, A.; Nowacki, P.; Safranow, K.; Drechsler, H. Nonembolic, hemodynamic blood flow disturbances in the middle cerebral arteries in patients with paroxysmal atrial fibrillation without significant carotid stenosis. *Clin. Neurol. Neurosurg.* **2007**, *109*, doi:10.1016/j.clineuro.2007.06.001.
14. Freestone, D.R.; Aram, P.; Dewar, M.; Scerri, K.; Grayden, D.B.; Kadirkamanathan, V. A data-driven framework for neural field modeling. *Neuroimage* **2011**, *56*, doi:10.1016/j.neuroimage.2011.02.027.
15. Hunter, T.J.; Joseph, J.J.; Anazodo, U.; Kharche, S.R.; McIntyre, C.W.; Goldman, D. Atrial Fibrillation and Anterior Cerebral Artery Absence Reduce Cerebral Perfusion: A De Novo Hemodynamic Model. *Appl. Sci.* **2022**, *12*, 1750, doi:10.3390/app12031750.
16. Ganong, W.F. Ganong's Review of Medical Physiology—23rd edition; **2005**;
17. Frank, O. The basic shape of the arterial pulse. First treatise: Mathematical analysis. *J. Mol. Cell. Cardiol.* **1990**, *22*, doi:10.1016/0022-2828(90)91460-O.
18. Wetterer, E. Flow and pressure in the arterial system, their hemodynamic relationship, and the principles of their measurement. *Minn. Med.* **1954**, *37*, 77-86.
19. Wetterer, E. Die Wirkung der Herztaetigkeit auf die Dynamik des Arteriensystems. In Proceedings of the Klinische Wochenschrift; **1956**; Vol. 34, p. 609.
20. Wetterer, E. Quantitative Beziehungen zwischen Stromstärke und Druck im natürlichen Kreislauf bei zeitlich variabler Elastizität des arteriellen Windkessels; Wetterer, Erik, Dr. med; JF Lehmanns Verlag, **1940**;
21. Westerhof, N.; Bosman, F.; De Vries, C.J.; Noordergraaf, A. Analog studies of the human systemic arterial tree. *J. Biomech.* **1969**, *2*, doi:10.1016/0021-9290(69)90024-4.
22. Westerhof, N.; Elzinga, G.; Sipkema, P. An artificial arterial system for pumping hearts. *J. Appl. Physiol.* **1971**, *31*, doi:10.1152/jappl.1971.31.5.776.
23. Westerhof, N.; Lankhaar, J.W.; Westerhof, B.E. The arterial windkessel. *Med. Biol. Eng. Comput.* **2009**, *47*.
24. Segers, P.; Brimiouille, S.; Stergiopoulos, N.; Westerhof, N.; Naeije, R.; Maggiorini, M.; Verdonck, P. Pulmonary arterial compliance in dogs and pigs: The three-element windkessel model revisited. *Am. J. Physiol. - Hear. Circ. Physiol.* **1999**, *277*, doi:10.1152/ajpheart.1999.277.2.h725.
25. Stergiopoulos, N.; Meister, J.J.; Westerhof, N. Simple and accurate way for estimating total and segmental arterial compliance: The pulse pressure method. *Ann. Biomed. Eng.* **1994**, *22*, doi:10.1007/BF02368245.
26. Westerhof, N.; Elzinga, G. Normalized input impedance and arterial decay time over heart period are independent of animal size. *Am. J. Physiol. - Regul. Integr. Comp. Physiol.* **1991**, *261*, doi:10.1152/ajpregu.1991.261.1.r126.
27. Stergiopoulos, N.; Westerhof, B.E.; Westerhof, N. Total arterial inertance as the fourth element of the windkessel model. *Am. J. Physiol. - Hear. Circ. Physiol.* **1999**, *276*, doi:10.1152/ajpheart.1999.276.1.h81.
28. Defares, J.G.; Osborn, J.J.; Hara, H.H. Theoretical synthesis of the cardiovascular system. Study I: The controlled system. *Acta Physiol. Pharmacol. Neerl.* **1963**, *12*.
29. Birkhoff, G.; Rota, G.-C. *Ordinary Differential Equations*; 4th Edition.; John Wiley & Sons, Ltd, **1989**; ISBN 978-0-471-86003-7.

30. Press, W.H.; Teukolsky, S.A.; Vetterling, W.T.; Flannery, B.P. *NUMERICAL RECIPES The Art of Scientific Computing Third Edition*; **2007**;
31. Ascher, U.M.; Petzold, L.R. Computer methods for ordinary differential equations and differential-algebraic equations; **1998**;
32. Krogh, A. The number and distribution of capillaries in muscles with calculations of the oxygen pressure head necessary for supplying the tissue. *J. Physiol.* **1919**, *52*, doi:10.1113/jphysiol.1919.sp001839.
33. Widmaeir, E.P. DKK Vander's Human Physiology: the Mechanisms of Body Function, Fifteenth Edition; 2017; Vol. 53;.
34. Guyton, A.C.; Coleman, T.G.; Granger, H.J. Circulation: overall regulation. *Annu. Rev. Physiol.* **1972**, *34*.
35. Suga, H.; Sagawa, K.; Shoukas, A.A. Load independence of the instantaneous pressure-volume ratio of the canine left ventricle and effects of epinephrine and heart rate on the ratio. *Circ. Res.* **1973**, *32*, doi:10.1161/01.RES.32.3.314.
36. Heldt, T. Computational models of cardiovascular response to orthostatic stress. **2004**, 185.
37. Ursino, M.; Giannessi, M. A model of cerebrovascular reactivity including the circle of Willis and cortical anastomoses. *Ann. Biomed. Eng.* **2010**, *38*, 955–974, doi:10.1007/S10439-010-9923-7/TABLES/2.
38. Spronck, B.; Martens, E.G.H.J.; Gommer, E.D.; van de Vosse, F.N. A lumped parameter model of cerebral blood flow control combining cerebral autoregulation and neurovascular coupling. *Am. J. Physiol. - Hear. Circ. Physiol.* **2012**, *303*, doi:10.1152/ajpheart.00303.2012.
39. Lan, H.; Updegrave, A.; Wilson, N.M.; Maher, G.D.; Shadden, S.C.; Marsden, A.L. A Re-Engineered Software Interface and Workflow for the Open-Source SimVascular Cardiovascular Modeling Package. *J. Biomech. Eng.* **2018**, *140*, doi:10.1115/1.4038751/367484.
40. Steinman, D.A.; Poepping, T.L.; Tambasco, M.; Rankin, R.N.; Holdsworth, D.W. Flow Patterns at the Stenosed Carotid Bifurcation: Effect of Concentric versus Eccentric Stenosis. *Ann. Biomed. Eng.* **2000**, *28*, 415–423, doi:10.1114/1.279.
41. Antiga, L.; Piccinelli, M.; Botti, L.; Ene-Iordache, B.; Remuzzi, A.; Steinman, D.A. An image-based modeling framework for patient-specific computational hemodynamics. *Med. Biol. Eng. Comput.* **2008**, *46*, 1097–1112, doi:10.1007/s11517-008-0420-1.
42. Alastruey, J.; Parker, K.H.; Peiró, J.; Byrd, S.M.; Sherwin, S.J. Modelling the circle of Willis to assess the effects of anatomical variations and occlusions on cerebral flows. *J. Biomech.* **2007**, *40*, 1794–1805, doi:10.1016/J.JBIOMECH.2006.07.008.
43. Taylor, C.A.; Draney, M.T.; Ku, J.P.; Parker, D.; Steele, B.N.; Wang, K.; Zarins, C.K. Predictive medicine: Computational techniques in therapeutic decision-making. *Comput. Aided Surg.* **1999**, *4*, doi:10.1002/(sici)1097-0150(1999)4:5<231::aid-igs1>3.0.co;2-z.
44. Taylor, C.A.; Hughes, T.J.R.; Zarins, C.K. Finite element modeling of blood flow in arteries. *Comput. Methods Appl. Mech. Eng.* **1998**, *158*, 155–196, doi:10.1016/S0045-7825(98)80008-X.

45. Taylor, C.A.; Fonte, T.A.; Min, J.K. Computational Fluid Dynamics Applied to Cardiac Computed Tomography for Noninvasive Quantification of Fractional Flow Reserve: Scientific Basis. *J. Am. Coll. Cardiol.* **2013**, *61*, 2233–2241, doi:10.1016/J.JACC.2012.11.083.
46. Arthurs, C.J.; Khlebnikov, R.; Melville, A.; Marčan, M.; Gomez, A.; Dillon-Murphy, D.; Cuomo, F.; Vieira, M.S.; Schollenberger, J.; Lynch, S.R.; et al. CRIMSON: An open-source software framework for cardiovascular integrated modelling and simulation. *PLoS Comput. Biol.* **2021**, *17*, doi:10.1371/journal.pcbi.1008881.
47. Ben Ahmed, S.; Dillon-Murphy, D.; Figueroa, C.A. Computational Study of Anatomical Risk Factors in Idealized Models of Type B Aortic Dissection. *Eur. J. Vasc. Endovasc. Surg.* **2016**, *52*, 736–745, doi:10.1016/J.EJVS.2016.07.025.

Chapter 2. Computational Modelling of Cerebral Hemodynamics During Atrial Fibrillation: A Lumped Parameter Approach

This chapter is based upon the following publication: Hunter, T. J.; Joseph, J.J.; Anazodo, U.; Kharche, S.R.; McIntyre, C.W.; Goldman, D. Computational Modelling of the Role of Atrial Fibrillation on Cerebral Blood Perfusion. *Appl. Sci.* **2022**, 12(3), 1750. <https://doi.org/10.3390/app12031750>. [1]

2.1. Introduction

Atrial fibrillation (AF) currently affects a large part of the population. In addition to commonly known risks such as strokes and transient ischemic attacks, AF has been associated with increased cognitive decline and early dementia [2]. AF is known to reduce cerebral perfusion [3], and silent cerebral ischemia is thought to be a key mechanism in the increased cognitive risk [2,4]. Ongoing imaging research strongly suggests that a disrupted cerebral blood flow promotes debilitating early dementia [5]. The effects of AF on cerebral perfusion may be modulated by cerebral vascular geometry, and specifically by common congenital Circle of Willis (CoW) variants [6,7]. The function of a complete CoW is to ensure consistent distribution of blood flow to all regions of the brain. In cases with missing segments in the CoW, regions of the brain may be more susceptible to harmful altered hemodynamics. The aim of this work is to investigate whether structural variants of the CoW behave differently with respect to cerebral perfusion in AF conditions.

Multi-scale hemodynamic modelling has been used to study cerebral circulation and gain insight into patient-specific hemodynamics [8]. 3D modelling is a useful tool, which provides realistic and accurate patient-specific insight into patient hemodynamics. It has increasingly been used as the gold standard in computational hemodynamic studies as

computational fluid dynamics platforms become more accessible [9]. However, current 3D methods remain computationally resource intensive, require super high-definition vascular imaging, and are therefore unsuitable for applications studying large population hemodynamics.

In contrast to 3D hemodynamic models, lumped parameter (0D) models are known to provide clinically relevant information using significantly less time and computational resources [8]. 0D models are particularly useful in studies where there are poorly understood outcomes of diseases with well understood mechanisms because of their ability to assess the impact of a range of parameters or cases on a particular outcome. This lab has previously used 0D models to gain insight into the causes of pediatric hypertension [10] and investigate therapeutic hypothermia [11]. Anselmino et al. [4] used 0D modelling to investigate the interplay between AF and cerebral hemodynamics. They determined that AF does indeed expose the brain to the risk of ischemia via low blood flow, or so-called hypoperfusion events. Saglietto et al. [12] also used 0D modelling to predict that the optimal goal for a heart rate control strategy should be around 60 bpm, considered strict rate control.

The findings by Saglietto et al. [12] contrast with the common practice of lenient rate control (<110 bpm), which is based on findings from the RACE II trial, a large, randomized control trial [13]. The RACE II trial was a consequential study, which found that, compared to lenient rate control (<110 bpm), strict rate control (<80 bpm) was not more effective in reducing mortality in persistent AF patients. These findings have informed treatment strategies for persistent AF patients; however, they do not consider the increased risk for dementia, later confirmed by de Bruijn et al. [2] in a longitudinal study. Modelling studies following de Bruijn et al. [2] have aimed at elucidating the mechanism behind the increased risk and finding potential treatment strategies that mitigate it.

Previous modelling studies form the basis for the present work. However, the role of cerebral vascular structural variants, (CoW variants) in the context of AF-cerebral perfusion relationship remains underexplored. As the CoW is known to play an important role in the distribution of blood flow to the brain, common variants should be considered while studying the interplay between AF and cerebral hemodynamics. In this study, a

composite 0D model of human circulation with detailed cerebral vasculature was developed to discover the effects of AF on cerebral perfusion in cases with common CoW variants. Model composition is described in Section 2.1. The model is used to assess cerebral hemodynamics during AF in all six common CoW variants, the strategy for which is described in Section 2.4. Finally, the model itself is also assessed using sensitivity analysis as described in Section 2.5, which details the parameter values that are correlated to model outcomes.

2.2. Methods

This study is a modelling study that examines the role of varying blood vessel geometries in AF-related cerebral hypoperfusion. A previously developed composite 0D model [1] (Figure 5) was used to simulate cerebral hemodynamics under control and AF conditions. Six common variants of CoW geometry were modelled as separate cases, and the results for each are presented. Sensitivity analysis was also performed on the model to assess model parameters that had the greatest impact on simulated outcomes.

2.2.1. Model Components

The 0D model is a composite model that consists of whole-body circulation, a blood-pressure modulated baroreflex control mechanism, and detailed cerebral circulation with an autoregulation function. All model parameters were inherited from the literature values, unless otherwise stated.

The whole-body circulation model was adapted from the model published by Heldt [14]. It consists of a network of blood containing elastic Windkessel compartments, which represent individual, or networks of, blood vessels. The time-dependent change in pressure within each compartment is a function of the change in volume (i.e., flow in or out) divided by the compliance of the compartment shown by the equation:

$$\frac{dP}{dt} = \frac{(q_{in} - q_{out})}{C} \quad \text{Equation 14}$$

where P is the compartment pressure, t is time, q denotes flow rate, and C denotes compliance. Flow between connected compartments is calculated using the equation:

$$q = \frac{(P_p - P_d)}{R} \quad \text{Equation 15}$$

where P_p and P_d denote proximal and distal pressure respectively, and R denotes resistance.

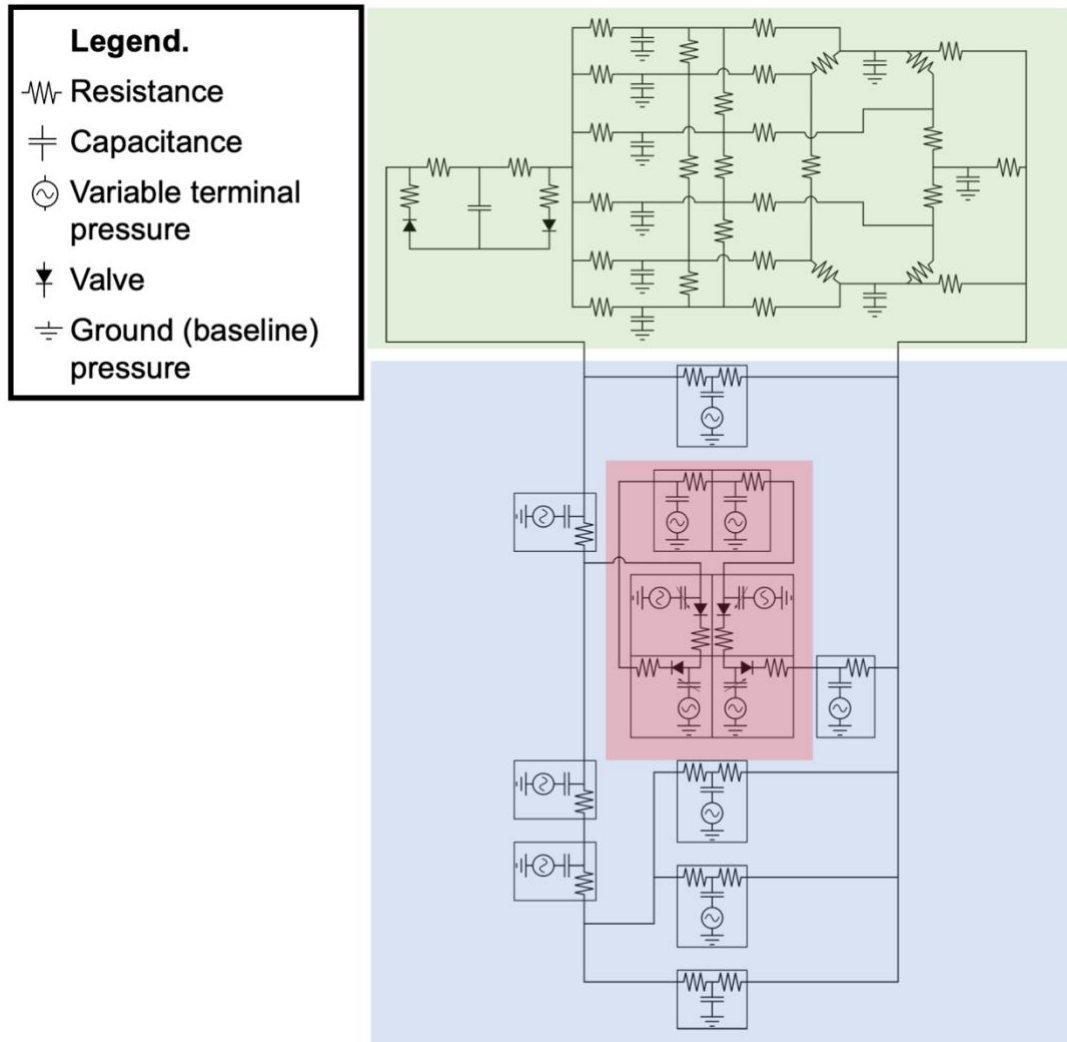


Figure 5. Electrical analogue of whole-body blood flow model. The green shaded area (top) represents the cerebral circulation, including the complete Circle of Willis, distal circulation, and cerebral spinal fluid compartment, which are further detailed in Figure 6. The red shaded region (middle) represents the heart, including the four pumping chambers of the heart and valves, as well as an aortic compartment. The blue shaded region (bottom) represents the systemic circulation, including splanchnic, kidney, legs, upper body, lungs, and venous circulation. The symbols represent electrical elements shown in the figure legend.

The pumping heart is represented as four compartments with variable elastance (inverse of compliance), representing the four chambers of the heart. The time-dependent elastances of ventricles and atria were calculated using activation terms. The equation for atrial activation is:

$$\text{act}_a = \begin{cases} 1 - \cos(\pi \cdot t_{loc}/t_{a,sys}) & \text{if } 0 < t_{loc} \leq t_{a,sys} \\ 1 - \cos(2 \cdot \pi \cdot (t_{loc} - t_{a,sys})/t_{a,sys}) & \text{if } t_{a,sys} < t_{loc} \leq 1.5 \cdot t_{a,sys} \\ 0 & \text{otherwise} \end{cases} \quad \text{Equation 16}$$

in which act_a is the activation term, t_{loc} is the time since the initiation of the cardiac cycle, $t_{a,sys}$ is a contraction timing parameter. Similarly ventricular activation is calculated using:

$$\text{act}_v = \begin{cases} 1 - \cos(\pi \cdot t_{loc} - t_{av}/t_s) & \text{if } t_{av} < t_{loc} \leq t_{av} + t_s \\ 1 - \cos(2 \cdot \pi \cdot (t_{loc} - t_{av} - t_s)/t_s) & \text{if } t_{av} + t_s < t_{loc} \leq t_{av} + 1.5 \cdot t_s \\ 0 & \text{otherwise} \end{cases} \quad \text{Equation 17}$$

where t_{av} is the atrioventricular time delay, t_s is a contraction timing parameter. The activation constants are applied to each heart compartment using the equation:

$$E = E_{dias} + 0.5 \cdot (E_{sys} - E_{dias}) \cdot \text{act} \quad \text{Equation 18}$$

where E_{sys} and E_{dias} are systolic and diastolic elastances respectively.

Additionally, backflow is prevented in the heart and systemic veins by setting flow between compartments equal to 0 if distal pressure is greater than proximal pressure. A simplified caricature of the circulation model is presented in Figure 5, in which systemic compartments are represented by boxes, and connections are indicated by straight lines.

The baroreflex is a feedback mechanism works to maintain hemodynamic homeostasis. It modulates peripheral vascular resistance, heart rate, and heart contractility to maintain systemic blood pressure and flow at healthy levels. The baroreceptor mechanism is implemented according to the model proposed by Lin et al. [15]. The model dynamically calculates sympathetic nervous activity (SNA) and parasympathetic nervous activity (PNA) based on the mean arterial pressure, as well as arterial carbon dioxide partial pressure (PCO_2), which is assigned a constant value of 40 mmHg. Values for sympathetic nervous activity and parasympathetic nervous activity are then used to dynamically modulate peripheral vascular resistance, the intrinsic heart rate, as well as heart contractility via modulation terms [15].

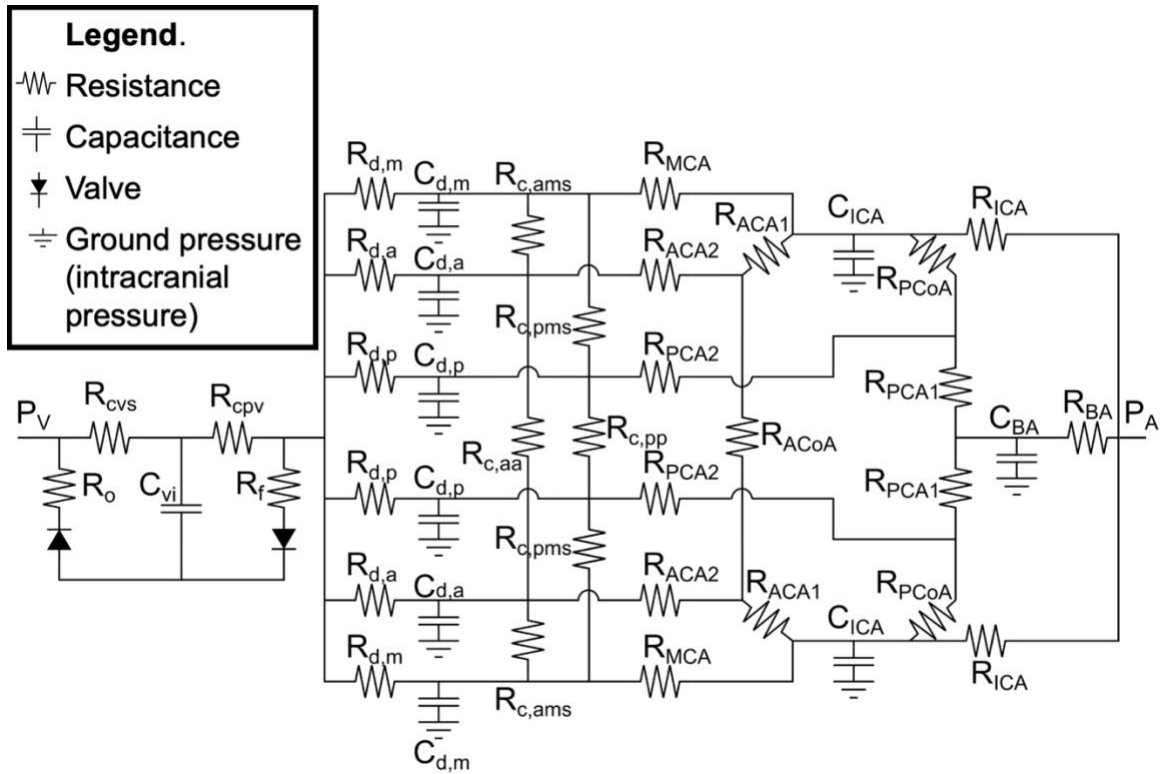


Figure 6. Electrical analog diagram of the cerebral circulation module. All resistances and capacitances are labeled, values and descriptions for which are given in Appendix A1. P_A is the inlet, given as the arterial pressure value from the systemic model. P_V is the outlet, given as superior vena cava pressure from the systemic model.

The cerebral circulation model is comprised of a network of elastic vessel compartments detailed in Figure 6. Pressure and flow are governed by similar equations as the systemic model (Ursino and Gianessi [16]). The model implements cerebral autoregulation, which is a physiological mechanism that alters vascular resistance and compliance in order to maintain cerebral blood flow within healthy ranges in the case of widely varying pressure. Each downstream region (Figure 6, RA, LA, RM, LM, RP, LP) is regulated by an autoregulation function comprised of two integrated signals which are given as ODEs. The first is blood flow rate in the region, which is calculated dynamically. The ODE for this signal is given as,

$$\frac{dx_{aut,j}}{dt} = - \frac{x_{aut,j} + G_{aut,j} \left(\frac{q_j - q_{n,j}}{q_{n,j}} \right)}{\tau_{aut,j}} \quad \text{Equation 19}$$

$$j = ra, la, rm, lm, rp, lp;$$

where $x_{aut,j}$ is the autoregulation signal, $G_{aut,j}$ is a gain value, q_j is the volumetric flow rate in the region j , $q_{n,j}$ is the normal value for volumetric flow rate in the region j , and $\tau_{aut,j}$ is the time constant for the filter function. The second signal is from arterial PCO_2 , which is assigned a value of 40 mmHg. The signal is calculated with a similar equation, with the addition of an activation function. These are not detailed here because the present study does not investigate the effect of varying arterial PCO_2 , however the interested reader may find the equations in the code or Ursino et al. [16]. Distal compliances are dynamically calculated by passing these two signals through a sigmoidal relationship with upper and lower saturation levels, given by the equation

$$C_{d,j} = \frac{C_{d0,j} \cdot \{(1 - \Delta C_{d,j}/2) + (1 + \Delta C_{d,j}/2) \cdot \exp[(x_{aut,j} - x_{aut,j})/k_{Cd,j}]\}}{1 + \exp[(x_{aut,j} - x_{aut,j})/k_{Cd,j}]} \quad \text{Equation 20}$$

where $k_{Cd,j}$ is a constant parameter, inversely proportional to the central slope of the sigmoidal curve, and $C_{d0,j}$ and $\Delta C_{d,j}$ are the central values and the amplitude of the sigmoidal curves in the different distal regions. Blood flow from the whole-body model to the cerebral model was allowed by connecting the basilar and internal carotid arteries to the aortic compartment, and by connecting the cerebral outlet vein to the superior vena cava compartment.

This work considers the six common variants of the Circle of Willis found in the cerebral vasculature, represented in Figure 7 [7]. All variants, aside from the complete variant, are characterized by one or multiple missing segments of the CoW (Figure 8). To model the absence of the relevant cerebral vessel, its inlet and outlet flow was assigned a nil value.

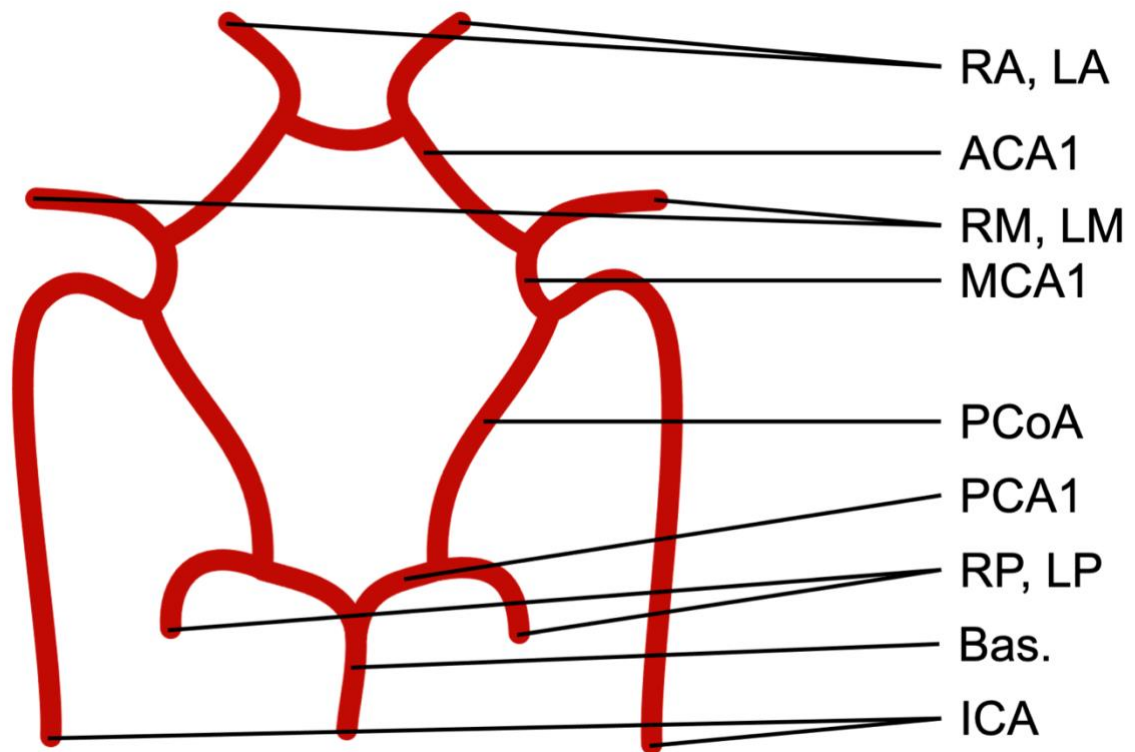


Figure 7. Caricature of the complete Circle of Willis. Blood flows into the Circle of Willis through the internal carotid arteries (ICA) and the basilar artery (BA). RA: Right anterior artery; LA: left anterior artery; RM: right middle artery; LM: left middle artery; RP: right posterior artery; LP: left posterior artery; ACA1: pre-communicating anterior cerebral artery; PCoA: posterior communicating artery; and PCA1: pre-communicating posterior cerebral artery.

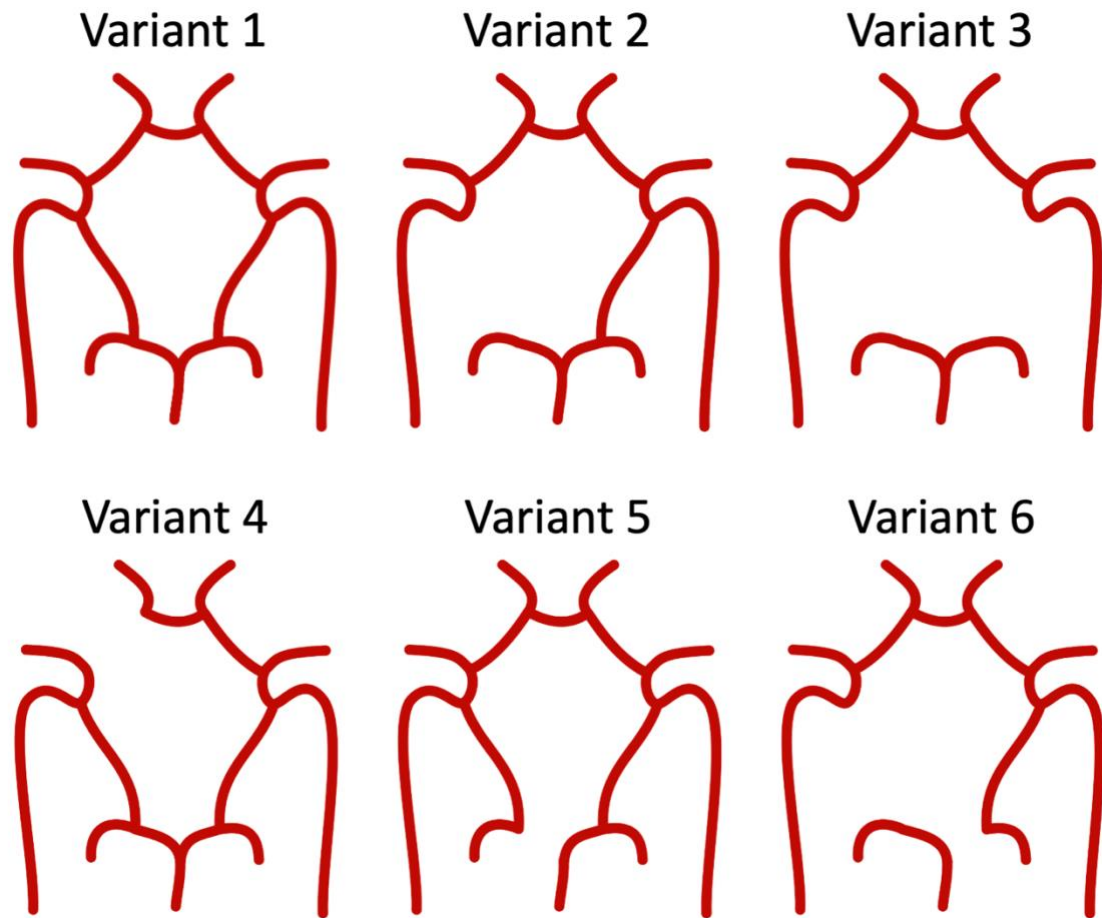


Figure 8. Caricature representations of all the common CoW variants. Variant 1 has all CoW vessels. Variant 2 has a missing posterior communicating artery (PCoA). Variant 3 has both missing PCoAs. Variant 4 has a missing precommunicating anterior cerebral artery, ACA1, segment. Variant 5 has a missing precommunicating posterior cerebral artery, PCA1, segment. Variant 6 has a missing PCoA and contralateral PCA1 segment.

2.2.2. Atrial Fibrillation

Each instance was simulated under AF and control conditions. The control was defined as having normal sinus rhythm (NSR) with stochastic RR intervals sampled from a normally distributed pink noise generator [17]. AF was modelled by assigning stochastic RR intervals sampled from an exponentially modified Gaussian distribution around a mean heart rate as shown in Figure 9, modifying ventricular elastances (contractility), and

assigning nil atrial contractility [4,17–19]. Pink noise and exponential samples were generated using in-house MATLAB scripts.

2.2.3. Numerical Methods

The model used in this study has 57 coupled stiff ordinary differential equations (ODEs) and was implemented in the C programming language. The SUNDIALS library [20] with in-house modifications was deployed to generate stable and accurate numerical solutions. The maximum integration timestep in the adaptive and implicit solver was 0.001 s, which was found to provide the same solution when the timestep was halved. The solutions were obtained using a relative tolerance of 10^{-6} , with an accuracy of $O(dt^6)$. Each instance of the simulation could be processed by available computing resources running Red Hat Linux within 60 s. Instances were trivially parallelized using GNU Parallel [21] in order to run a large number of instances (10^4) on multi-core compute nodes.

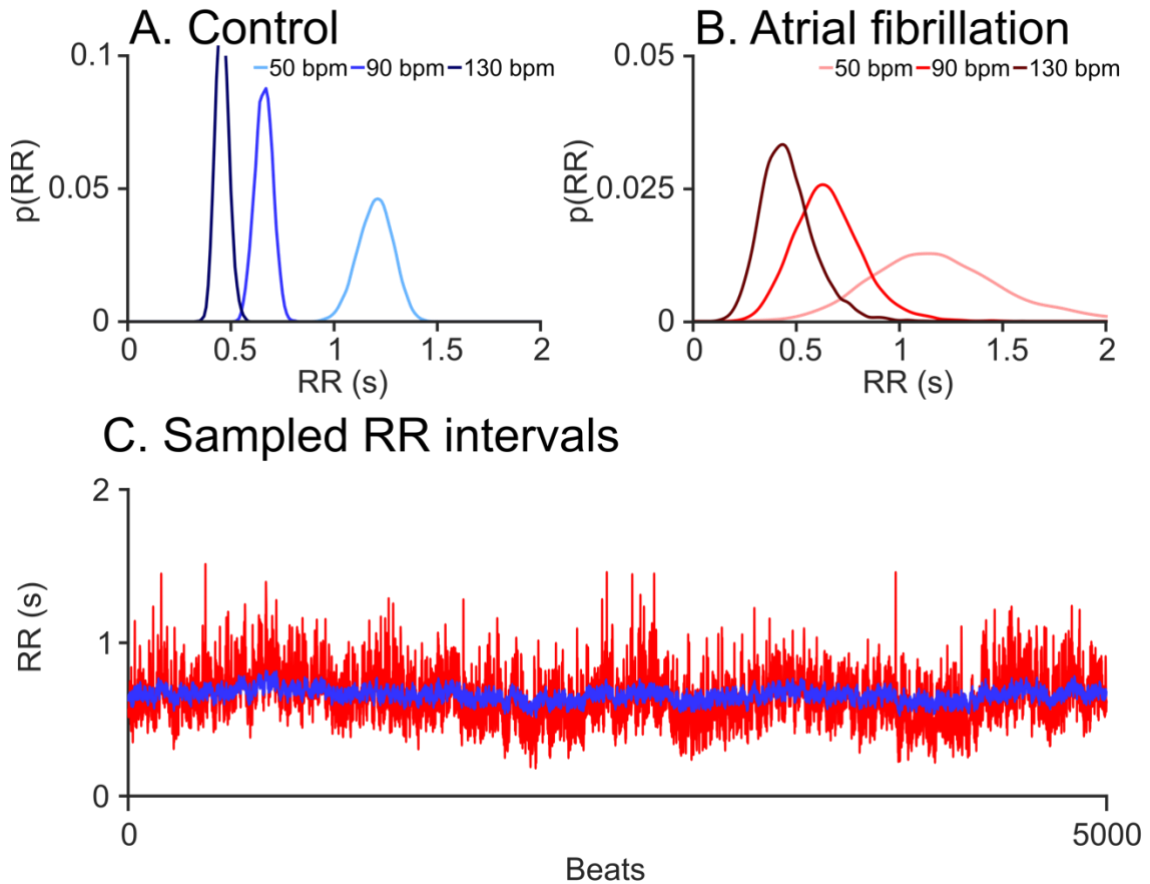


Figure 9. Stochastic RR interval assignment. Top row: Probability distribution functions for sampled RR intervals in normal sinus rhythm (A), and AF (B) at shown heart rates. C: Sampled RR intervals with mean of 70 bpm over the span of 5000 beats under NSR (blue line) and AF (red line) conditions.

2.2.4. Hemodynamic Differences in CoW Variants

Blood flow was simulated in each variant at nine different intrinsic heart rates (50 to 130 bpm in steps of 10 bpm) in accordance with clinical practice [22]. The probability distribution functions underlying the RR intervals and the representative RR interval time series are illustrated in Figure 9. In each simulation, the number of hypoperfusion events was recorded to represent cerebral perfusion deficit. Derived measurements were the number of hypoperfusion events in each vascular bed over the 5000 beats of the simulation. A hypoperfusion event in any vascular bed was defined as a heartbeat in which the mean blood flow through the vascular bed fell below the 5th percentile of blood flow in the corresponding NSR experiment.

2.2.5. Sensitivity Analysis

Sensitivity analysis is a tool that provides a comprehensive understanding of the workings of a computational model with respect to its parameters and a specified modelling outcome [23]. The model has 95 parameters, which include all resistances, compliances, vessel geometry attributes, time constants, and scaling factors. Parameters' descriptions and acronyms, as well as their control values relevant to this work, are provided in Table 2. Model behavior was defined as the total number of hypoperfusion events in the distal cerebral circulation over a 5000-heartbeat simulation.

To permit sensitivity analysis, a control model population of 10^4 instances was constructed. To generate the population, 95 modelling parameters were each randomly sampled simultaneously from uniform distributions using a non-repetitive Mersenne Twister random number generator [24]. The sampling was constrained using Latin Hypercube Sampling [25]. The lower and upper limits adopted for each parameter's uniform distribution were obtained by multiplying the literature value by 0.5. for the lower limit, and by 2.0 for the upper limit. The adopted limits provided a large range sampling for each parameter. The model parameters and model outputs were stored for further analysis. Sensitivity analysis, which ranked parameters according to their impact on model behavior, was performed using partial rank correlation coefficients (PRCC) [26].

Parameter	Description	Baseline Value
Systemic circulation		
HR ₀	Intrinsic heart rate	75 bpm
E _{dias,rv}	Right ventricular diastolic elastance.	0.07 (mmHg ml ⁻¹)
E _{sys,rv}	Right ventricular systolic elastance.	1.3 (mmHg ml ⁻¹)
E _{sys,ra}	Right atrial systolic elastance.	0.74 (mmHg ml ⁻¹)
E _{dias,ra}	Right atrial diastolic elastance.	0.3 (mmHg ml ⁻¹)
E _{dias,lv}	Left ventricular diastolic elastance.	0.13 (mmHg ml ⁻¹)
R _{pv}	Pulmonary venous resistance.	0.01 (mmHg s ml ⁻¹)
Cerebral circulation		
G _{aut}	Autoregulation function gain.	0.9 (unitless)
tau _{aut}	Autoregulation function time constant.	20 (s)
C _d	Distal cerebral arterial compliance.	200 (ml mmHg ⁻¹)
k _R	Distal cerebral resistance scaling term.	13,100 (mmHg ⁻³ s ml ⁻¹)

Table 2. Model parameters relevant to PRCC analysis.

To compute PRCC, first the normally distributed parameters (x_i) as well as the observed outputs (y_j) were rank transformed. Then, the linear effects of other additional variables are accounted for by expressing each as a linear regression of the inputs,

$$\hat{x}_j = a_0 + \sum_{\substack{k=1 \\ k \neq j}}^N a_k x_k, \text{ and } \hat{y}_j = b_0 + \sum_{\substack{k=1 \\ k \neq j}}^N b_k x_k \quad \text{Equation 21}$$

using residuals defined as $r_{xi} = x_i - \hat{x}_j$ and $r_{yi} = y_j - \hat{y}_j$, PRCC is defined as the correlation among these residuals normalized using their respective variances, i.e.

$$\text{PRCC}(x_i, y_j) = \frac{\text{Cov}(r_{xi}, r_{yj})}{\sqrt{\text{Var}(r_{xi})\text{Var}(r_{yj})}} \quad \text{Equation 22}$$

As evident in the above equation, PRCC assumes an underlying statistical model that is linear (regression), and assumption of monotonicity provides the strength of the linear relationship between a given pair of parameter and output [26, 27]. The PRCC indices range from -1 to $+1$.

2.3. Results

Model output statistics are presented from a single simulation instance with CoW variant 1 (complete CoW) at 80 bpm in Table 3. The statistics from the AF case are shown to be similar to those in the NSR case. Median systemic blood pressures of 117.44/77.81 mmHg (systolic/diastolic) for NSR and 119.51/78.95 mmHg for AF are shown to be similar to physiological levels. Additionally, total cerebral blood flow is 12.54 mL s⁻¹ for the NSR case and 12.31 mL s⁻¹ for the AF case.

Output Name	Output Values	
	NSR	AF
P _{a,sys} (mmHg)	117.44 ± 21.35	119.51 ± 17.45
P _{a,dias} (mmHg)	77.81 ± 15.85	78.95 ± 16.64
Q _{ACA} (ml s ⁻¹)	0.99 ± 0.37	0.95 ± 0.45
Q _{MCA} (ml s ⁻¹)	3.68 ± 1.21	3.64 ± 1.37
Q _{PCA} (ml s ⁻¹)	1.47 ± 0.52	1.44 ± 0.59
CBF (ml s ⁻¹)	12.54 ± 4.24	12.31 ± 4.78

Table 3. Model output statistics under NSR conditions.

Model output statistics for a simulation run with CoW variant 1 (complete CoW), at an HR of 80 bpm under AF and NSR conditions are shown in Table 3. Systemic pressure and cerebral blood flow statistics are shown to be similar in both NSR and AF cases. Values are shown as median ± standard deviation. P_{a,sys}: Arterial systolic pressure; P_{a,dias}: Arterial diastolic pressure; Q_{ACA}: Anterior cerebral artery flow rate; Q_{MCA}: Middle cerebral artery flow rate; Q_{PCA}: Posterior cerebral artery flow rate; CBF: Cerebral blood flow.

The model has demonstrated that large variations in blood pressure are propagated through the large arterial circulation and have a high impact on small vessels in the distal cerebral circulation, annotated as RA, LA, RM, LM, RP, and LP in Figure 7. This effect is demonstrated in Figure 10 where a drop in aortic blood pressure due to a long RR interval is associated with two consecutive hypoperfusion events. The example shows aortic blood pressure and simultaneous blood flow into the LM in a control and AF case, colored in blue and red, respectively. On panel A, the dip in blood pressure can be seen in the AF case between seconds 1 and 3. Corresponding with this dip, two hypoperfusion events are annotated with black in panel B, with horizontal lines indicating the mean blood flow value during the heartbeat to show that it is indeed below the fifth percentile of normal blood flow.

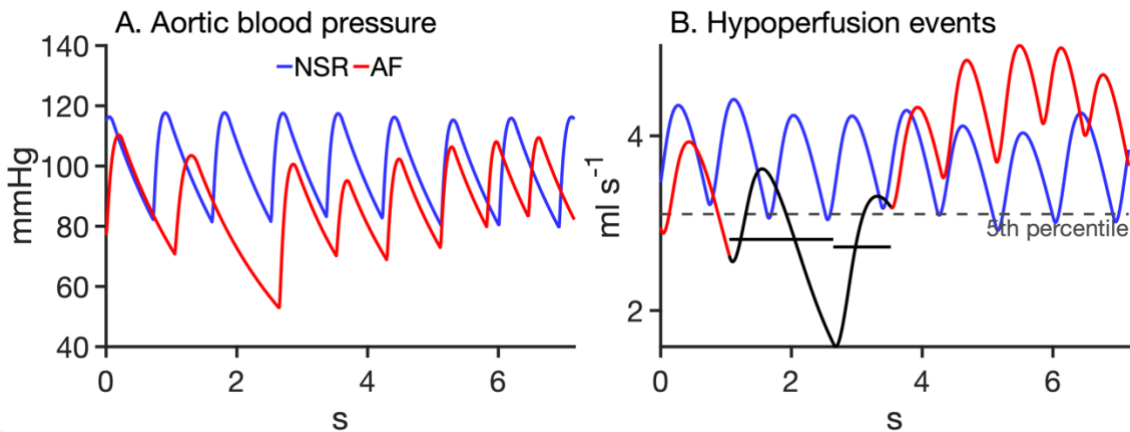


Figure 10. Hemodynamic outputs of a simulation of AF (red) and NSR (blue) at 70 bpm in the normal CoW. A: Aortic blood pressures. Under NSR the heart rate is stable giving rise to periodic aortic blood pressure. In contrast, under AF the heart rate is erratic that may promote a disproportionate loss of aortic blood pressure. B: Blood flow through the left middle distal artery with hypoperfusion events shown in black. A typical hypoperfusion event is shown with horizontal black lines overlaid on the AF related flow (red lines) whenever perfusion was below the 5th percentile threshold that was considered as a hypoperfusion event.

The heart rate and vascular geometry dependence of hypoperfusion events is illustrated in Figure 11. For each of the six common variants of the CoW, total hypoperfusion event counts are shown for simulations at imposed heart rates ranging from 50 to 130 bpm.

Counts include hypoperfusion events at each of the six distal regions of the brain over the entire 5000 heartbeat simulation, therefore the maximum possible count is 30000.

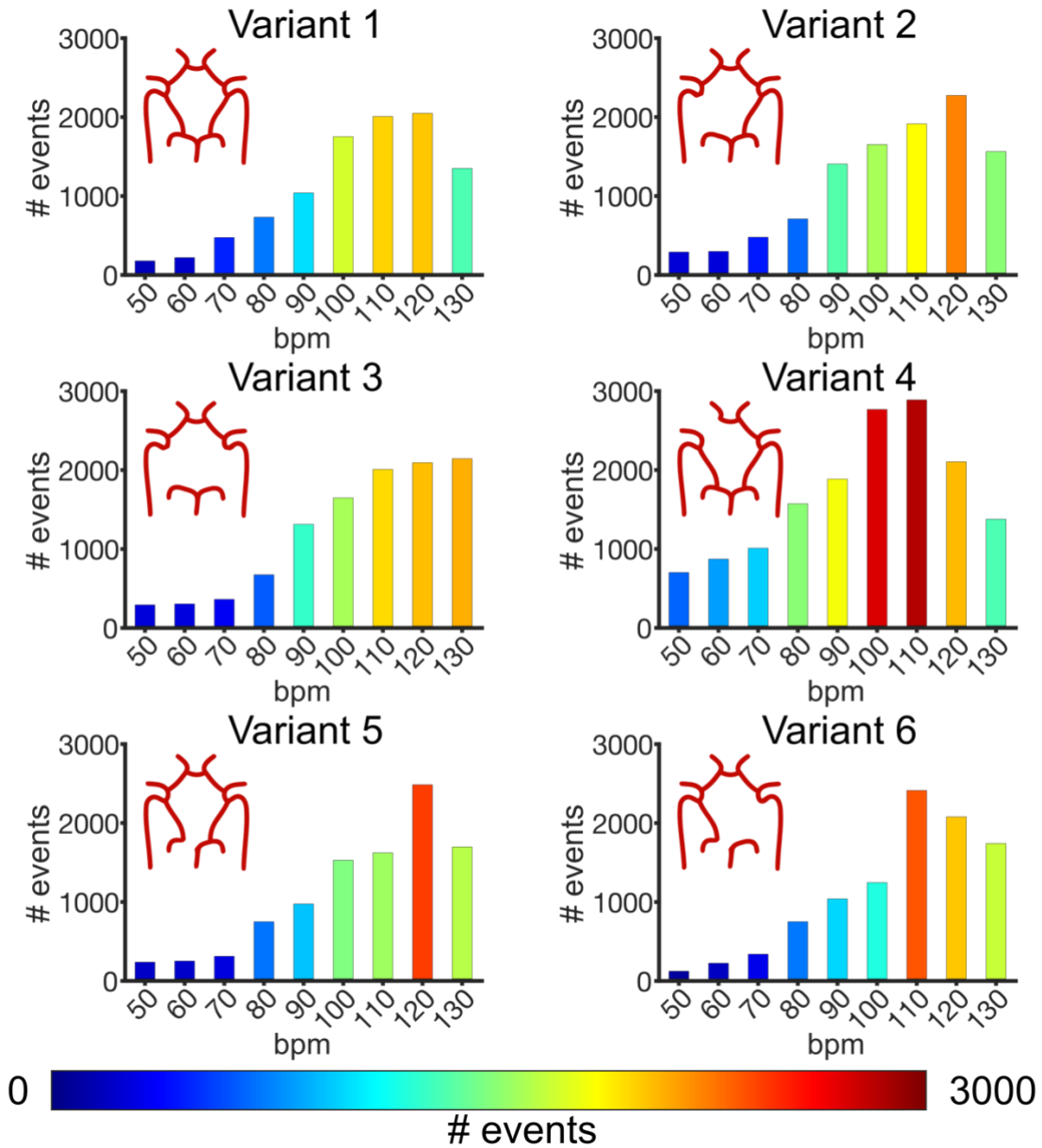


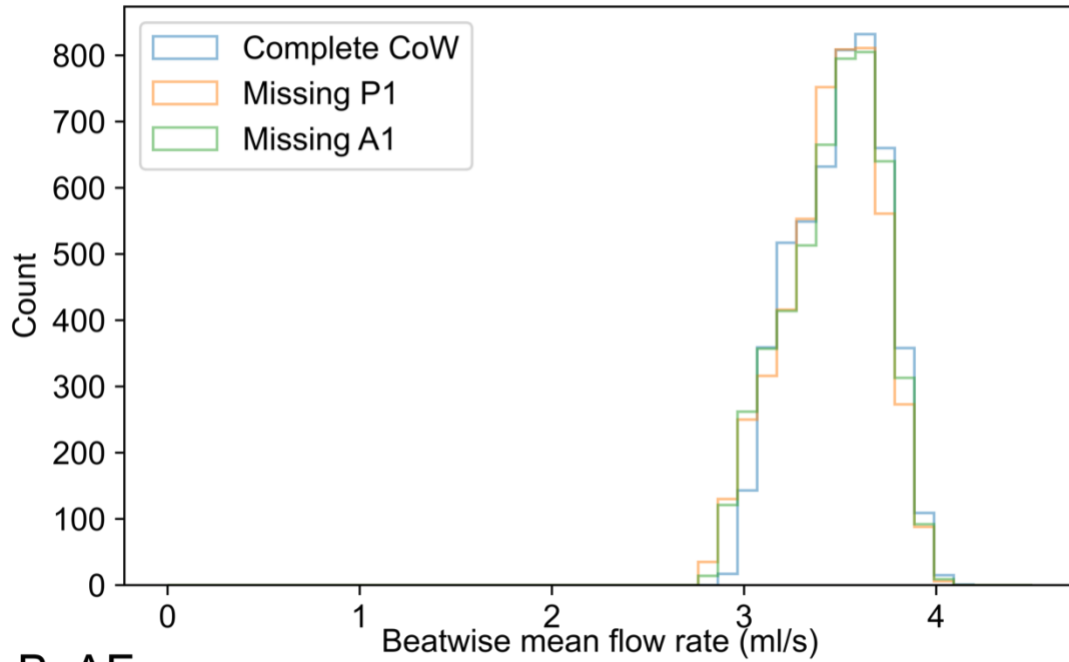
Figure 11. A grid of bar charts, in which each panel shows the number of hypoperfusion events found at a range of heart rates in a particular CoW variant. Each Cow variant was simulated for 5000 heart beats at each heart rate from 50 to 130 bpm.

All variants displayed similar behavior within the range of heart rates examined, with some differences in the number of counts, as well as the point at which they have the highest

hypoperfusion count. Variant 1, with a complete CoW, is represented in Figure 11 (top right). This variant had a minimum count occurring at a heart rate of 50 bpm with 178 total events, and a maximum count at 120 bpm with 2048 total events. Variant two, with a missing PCoA, is represented in Figure 11 (top left). This variant had a minimum count at 50 bpm with 264 events, and a maximum count at 120 bpm with 2248 events. Variant number three, with both PCoAs missing, is shown in Figure 11 (middle left). It had a minimum count at 50 bpm with 268 events, and a maximum count at 130 bpm with 2120 events. Variant four, with a missing ACA1, is represented in Figure 11 (middle right). This variant had a minimum count at 50 bpm with 675 events, and a maximum count at 110 bpm with 2861 events. Variant five, with a missing PCA1, is represented in Figure 11 (bottom left). This variant had a minimum count at 50 bpm with 211 events, and a maximum count at 120 bpm with 2458 events. Variant six, with a missing PCoA and contralateral PCA1, is represented in Figure 11 (bottom right). This variant had a minimum count at 50 bpm with 97 events, and a maximum count at 110 bpm with 2386 events. All variants had minimum counts at a 50 bpm heart rate. Maximum points varied between different variants, although all were within 110 to 130 bpm. Variant 3 is notable in that there is no count drop off at 130 bpm as there is in all other variants. Overall, all variants exhibit similar behavior, increasing count with bpm, up to a maximum around 120 bpm.

An example of beat-wise mean flow distributions for a set of simulation instances at 120 bpm are shown in Figure 12. Beat-wise mean flow is defined as the mean blood flow level during a cardiac cycle to a specified region of the brain. The data shown are beat-wise mean flow to the left medial (LM) region of the brain at 120 bpm, in variants 1, 4, and 5. These variants were chosen as they represent the complete CoW, and both cases with a major arterial segment missing. For the NSR case, the flow distributions (mean \pm std. dev., ml s⁻¹) are 3.49 ± 0.23 for variant 1 (complete CoW), 3.47 ± 0.25 for variant 4 (missing A1), and 3.46 ± 0.25 for variant 5 (missing P1). For the AF case, the flow distributions (mean \pm std. dev., ml s⁻¹) are 3.60 ± 0.38 for variant 1 (complete CoW), 3.58 ± 0.40 for variant 4 (missing A1), and 3.60 ± 0.37 for variant 5 (missing P1). Comparing the distributions from Figure 12A to those in Figure 12B shows that the primary reason for the occurrence of hypoperfusion events is a wider distribution of flow levels in the AF cases, as opposed to lower mean flow levels.

A. NSR



B. AF

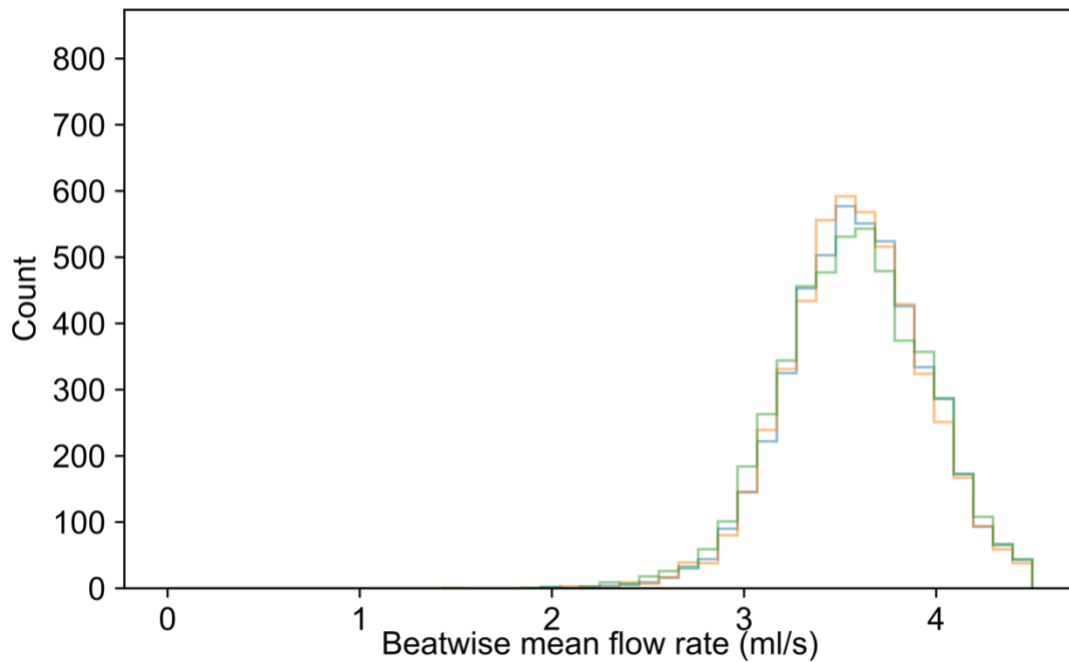


Figure 12. Histograms of beat-wise mean flow distributions in NSR and AF. Flow distributions are taken from flow to the left medial region. The top panel shows distributions for the NSR case, and the bottom shows distributions for the AF case. Three CoW variants are represented: variant 1 (complete CoW) in blue, variant 4 (missing A1) in orange, and variant 5 (missing P1) in green.

Figure 13 illustrates alterations in cerebral blood flow heterogeneity between the six variants. Under AF conditions, the left middle, left anterior, and left posterior regions experience a balanced outflow in variants 1 through 4 (Figure 13 variants 1-4), indicating virtually uniform cerebral perfusion. Alternatively, variants 5 and 6 show flow patterns that are more irregular. Both these variants also have either out-of-phase or negative-flow amplitude in the LP region relative to the other two regions shown. Additionally, flow oscillations in the LP region for these two variants have much larger amplitudes than flow to the other regions and compared to all flow in the other variants.

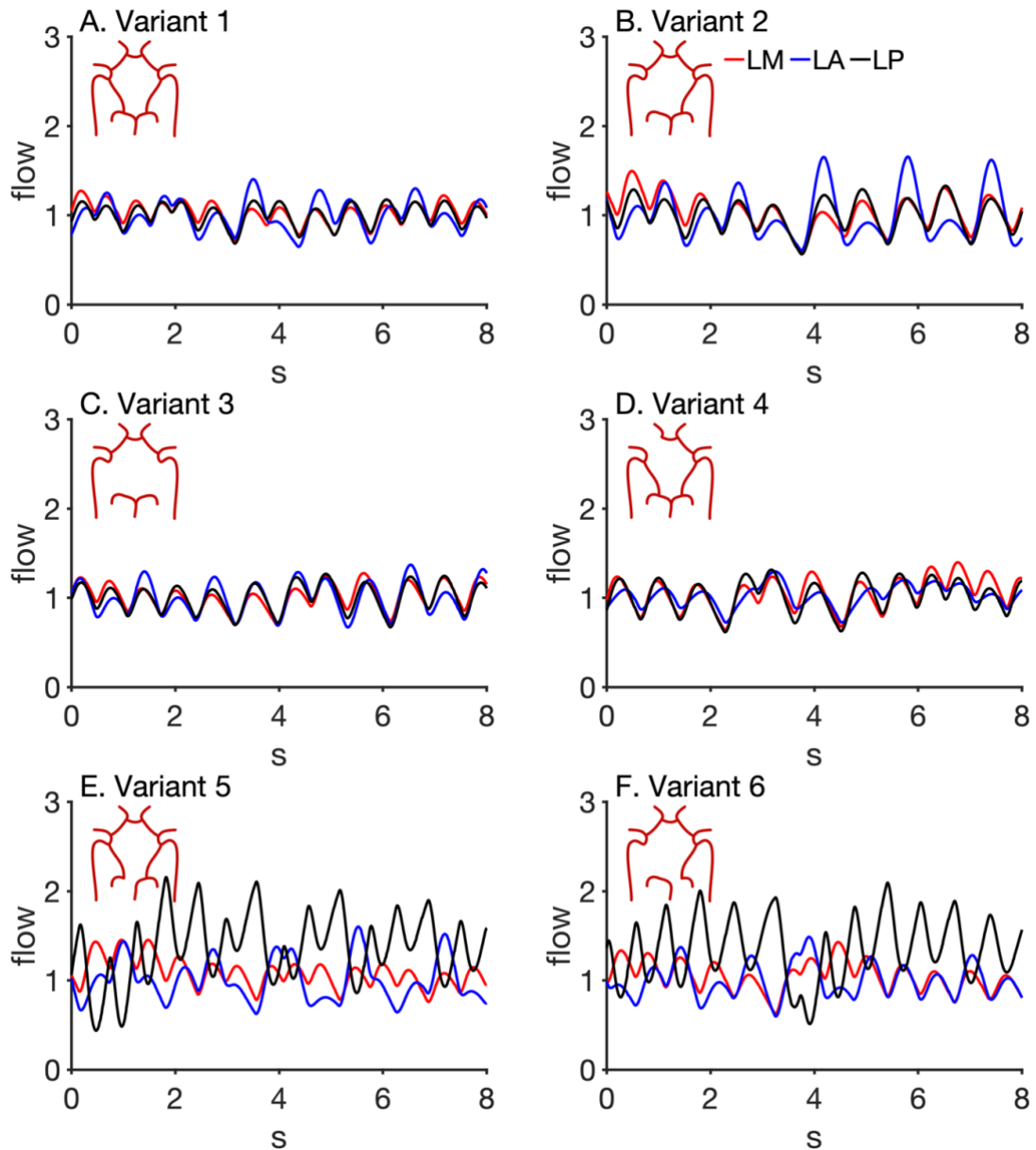


Figure 13. Perfusion to various parts of the brain, represented by outflow at three distinct vessel terminals. In all panels, black lines show blood flow rate in the left posterior (LP) region, blue lines show blood flow rate in the left anterior (LA) region, and red lines show blood flow rate in the left medial (LM) region. Blood flow rate was normalized by the mean flow rate for the respective regions. A: complete CoW. B: missing PCoA. C: Missing both PCoAs. D: Missing A1. E: missing P1. F: missing PCoA and P1.

As illustrated in Figure 14, the maximal PRCC values regarding hypoperfusion count are the intrinsic heart rate (HR_0), $E_{dias,rv}$, $E_{sys,rv}$, G_{aut} , and $E_{dias,ra}$. Notably, HR_0 ranked the highest for each variant, with varying amplitudes across the variants. Additionally, mechanical characteristics of the right ventricle and atria have high PRCC values, i.e., $E_{dias,rv}$, $E_{sys,rv}$, $E_{dias,ra}$, and $E_{sys,ra}$. G_{aut} , which plays a role in the cerebral autoregulation mechanism, also has a high PRCC value for all variants.

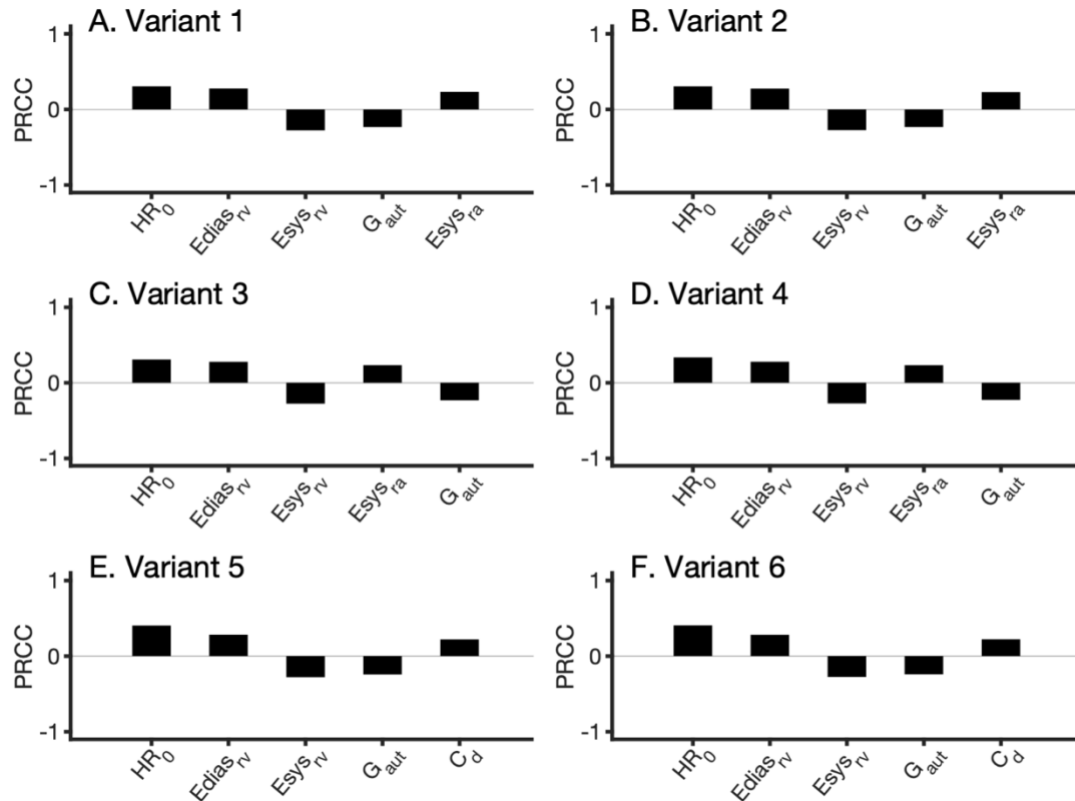


Figure 14. PRCC values for hypoperfusion count for each of the 6 considered CoW variants. The 5 PRCC values with the greatest magnitude are shown for each case and are ordered from greatest to least magnitude. Symbols are described in Table 2.

2.4. Discussion

While current treatment methods for AF, such as heart rate control and atrial ablation, are assessed based on treatment mortality, there is growing evidence that other factors, such as the impact on cognitive function, should be considered [2]. As research continues in this

field, the results of the present study suggest that the cerebrovascular structure should be considered in treatment planning to ensure better clinical outcomes.

The present model is a composite of previously published models. It is based on established biophysical modelling techniques, i.e., lumped-parameter modelling using Windkessel compartments. The components have been used previously to model a variety of disease cases, including AF. While direct model validation with in vivo data was not within the scope of the study, model outputs were presented for comparison with published values. Median arterial blood pressures (systolic/diastolic) were 117.44/77.81 mmHg and 119.51/78.95 mmHg for NSR and AF, respectively, which are considered to be within healthy ranges. Additionally, blood flow in major cerebral arteries is presented for comparison with measured values published by Zarrinkoob et al. [28]. Zarrinkoob reports blood flow in the ACA, MCA, and PCA to be 12%, 21%, and 8% of total CBF, respectively. The model shows corresponding values of 8%, 29%, and 12% for the NSR case, and 8%, 30%, and 12% for the AF case. Therefore, the model reflects clinically measured blood flow distribution, with predominant blood flow occurring in the MCA.

Variations from regular blood pressure in large arteries due to AF were shown to be associated with large changes in blood flow in the distal circulation of the brain (Figure 10). These changes lead to occurrences of critical hypoperfusion events in the brain, which may lead to silent cerebral ischemia, damaging brain tissue over time. The present modelling of this phenomenon is in agreement with previous works [1,4,12], and is the primary motivation for further investigation into the impacts of AF with respect to the cerebral circulation. Additionally, in Figure 10, it can be observed that the initial hypoperfusion seen at 2–4 s is followed by hyperperfusion from 4–7 s. This is to be expected because of the reflexive nature of the autoregulation mechanism. The autoregulatory function modulates the resistance and compliance of the downstream cerebral vessels within which the blood flow is being observed. The autoregulation function acts on a time scale of approximately 20 s, therefore there is a small delay between the drop in blood flow and the response of decreased resistance and increased compliance. This small delay in autoregulation function is thought to be the reason spontaneous drops in arterial pressure due to irregular heartbeats can cause transient hypoperfusion in the brain.

The result illustrated in Figure 11 shows that all considered CoW variants follow largely the same pattern with respect to the effect of heart rate on hypoperfusion frequency. All variants had a minimum hypoperfusion count at 50 bpm (in the heart rates considered), with the maximum occurring around 120 bpm. The most consequential result from this section is the result from variant 4, shown in Figure 11D. Variant 4 has a minimum hypoperfusion count of 675 at 50 bpm, which is over 2.5 times higher than variant 3, which has the next highest minimum. This demonstrates that although patients with CoW variant 4 may respond to a heart rate control strategy, it may not be sufficient to protect against hypoperfusion in the distal circulation of the brain. Based on this result, it is recommended that for patients with variant 4 of the CoW, alternative treatment methods be used in addition to, or instead of, heart rate control, in order to avoid ischemic cerebral damage.

It should be noted that this finding, along with previous modelling results [12], contradicts the recommendation made based on the RACE II trial [13]. The study found that relative to strict rate control, lenient rate control was as effective in preventing mortality and other outcomes and was easier to achieve. This finding has informed clinicians on rate control strategies in relation to preventing mortality in recent years. However, cognitive impairment/dementia was not considered to be outcomes of this study, and heart rate had not yet been linked to hypoperfusion events associated with AF. Therefore, there is now growing evidence supporting strict rate control for preventing deleterious cognitive outcomes.

It was shown that certain variants could lead to increased heterogeneity in cerebral blood flow, with increased blood flow in some regions, and decreased in others (Figure 13). In particular, both variants with a missing PCA1 segment (variants 5 and 6) displayed heterogeneous flow patterns, as well as having larger amplitudes of the oscillatory flow rate than the other variants. This indicates that the PCA1 segment plays a key role in the distribution of blood flow with respect to homogeneity among the distal cerebral vessels. Although the large oscillations in blood flow to the left posterior circulation present in these variants are not considered harmful by the metric of hypoperfusion events, which is the primary focus of this study, they may lead to detrimental outcomes via other mechanisms, such as abnormal wall shear stress or acute hypertension. These phenomena will be further investigated in future work.

Sensitivity analysis, as shown in Figure 14, shows the model parameters that have the largest impact on modelling outcomes, namely the hypoperfusion event frequency. It was shown that in all cases of variant CoWs, HR0 had the highest PRCC value, meaning that it is the parameter that most influences the hypoperfusion event frequency. This was expected, as heart rate control has been shown to be an effective method for decreasing hypoperfusion events [12,22]. In all variants, elastance values for the right heart were among the parameters with the largest PRCC values. This is an indication that the function of the right heart is strongly related to cerebral hypoperfusion outcomes and warrants further study.

The present work is an investigation into the impact of AF on cerebral circulation considering common cases of congenital variations to the CoW. The presented model considers AF in the absence of other common cardiovascular conditions such as hypertension or atherosclerosis and represents simple cases of missing arterial segments, for the purposes of direct comparison. The model components have previously been used to study such conditions as hypertension, atherosclerotic lesions, and arterial occlusions. Additionally, small variations in cerebrovascular structure can be trivially modelled by assigning modified resistances to blood vessels. Future work will focus on incorporating these common conditions into our modelling, to further understand the impact of AF on cerebral circulation. Previously used techniques for representing populations using 0D models will be employed to elucidate the impacts of varied cerebrovascular structures [11].

In a clinical environment, it is critical for computational models to be applicable on a patient-specific basis. Methods for the incorporation of imaging data into 0D blood flow models are currently under development and will be used to further assess the impact of variant vascular structures using patient-specific data [8,29]. Such methods will also be effective in the clinic, opening up the possibility of patient-specific assessments for persistent AF patients. The presented model is extensible and personalizable, which will permit patient-specific risk stratification [30]. Further investigation will be conducted using spatially resolved 1D modelling to investigate the impacts of these phenomena on the blood vessels as well as the surrounding tissue in greater detail.

2.5. References

1. Hunter TJ, Joseph JJ, Anazodo U, Kharche SR, McIntyre CW, Goldman D. Atrial Fibrillation and Anterior Cerebral Artery Absence Reduce Cerebral Perfusion: A De Novo Hemodynamic Model. *Applied Sciences*. **2022**; 12(3):1750.
2. De Bruijn, R.F.A.G.; Heeringa, J.; Wolters, F.J.; Franco, O.H.; Stricker, B.H.C.; Hofman, A.; Koudstaal, P.J.; Ikram, M.A. Association Between Atrial Fibrillation and Dementia in the General Population. *JAMA Neurol*. **2015**, 72, 1288–1294. <https://doi.org/10.1001/JAMANEUROL.2015.2161>.
3. Gardarsdottir, M.; Sigurdsson, S.; Aspelund, T.; Rokita, H.; Launer, L.J.; Gudnason, V.; Arnar, D.O. Atrial fibrillation is associated with decreased total cerebral blood flow and brain perfusion. *EP Eur*. **2018**, 20, 1252–1258. <https://doi.org/10.1093/EUROPACE/EUX220>.
4. Anselmino, M.; Scarsoglio, S.; Saglietto, A.; Gaita, F.; Ridolfi, L. Transient cerebral hypoperfusion and hypertensive events during atrial fibrillation: A plausible mechanism for cognitive impairment. *Sci. Rep*. **2016**, 6, 8635. <https://doi.org/10.1038/SREP28635>.
5. Anazodo, U.C.; Shoemaker, J.K.; Suskin, N.; St. Lawrence, K.S. An investigation of changes in regional gray matter volume in cardiovascular disease patients, pre and post cardiovascular rehabilitation. *Neuroimage* **2013**, 3, 388. <https://doi.org/10.1016/J.NICL.2013.09.011>.
6. Steinman, D.A.; Poepping, T.L.; Tambasco, M.; Rankin, R.N.; Holdsworth, D.W. Flow Patterns at the Stenosed Carotid Bifurcation: Effect of Concentric versus Eccentric Stenosis. *Ann. Biomed. Eng.* **2000**, 28, 415–423. <https://doi.org/10.1114/1.279>.
7. Alastruey, J.; Parker, K.H.; Peiró, J.; Byrd, S.M.; Sherwin, S.J. Modelling the circle of Willis to assess the effects of anatomical variations and occlusions on cerebral flows. *J. Biomech.* **2007**, 40, 1794–1805. <https://doi.org/10.1016/j.jbiomech.2006.07.008>.
8. Antiga, L.; Piccinelli, M.; Botti, L.; Ene-Iordache, B.; Remuzzi, A.; Steinman, D.A. An image-based modeling framework for patient-specific computational hemodynamics. *Med. Biol. Eng. Comput.* **2008**, 46, 1097–1112. <https://doi.org/10.1007/S11517-008-0420-1>.
9. Lan, H.; Updegrave, A.; Wilson, N.M.; Maher, G.D.; Shadden, S.C.; Marsden, A.L. A Re-Engineered Software Interface and Workflow for the Open-Source SimVascular Cardiovascular Modeling Package. *J. Biomech. Eng.* **2018**, 140, 024501. <https://doi.org/10.1115/1.4038751/367484>.
10. Altamirano-Diaz, L.; Kassay, A.D.; Serajelahi, B.; McIntyre, C.W.; Filler, G.; Kharche, S.R. Arterial Hypertension and Unusual Ascending Aortic Dilatation in a Neonate With Acute Kidney Injury: Mechanistic Computer Modeling. *Front. Physiol.* **2019**, 10, 1391. <https://doi.org/10.3389/FPHYS.2019.01391>.
11. Joseph, J.J.; Hunter, T.J.; Sun, C.; Goldman, D.; Kharche, S.R.; McIntyre, C.W. Using a Human Circulation Mathematical Model to Simulate the Effects of Hemodialysis and Therapeutic Hypothermia. *Appl. Sci.* **2021**, 12, 307. <https://doi.org/10.3390/app12010307>.

12. Saglietto, A.; Scarsoglio, S.; Ridolfi, L.; Gaita, F.; Anselmino, M. Higher ventricular rate during atrial fibrillation relates to increased cerebral hypoperfusions and hypertensive events. *Sci. Rep.* **2019**, *9*, 1–9. <https://doi.org/10.1038/s41598-019-40445-5>.
13. Van Gelder, I.C.; Groenveld, H.F.; Crijns, H.J.G.M.; Tuininga, Y.S.; Tijssen, J.G.P.; Alings, A.M.; Hillege, H.L.; Bergsma-Kadijk, J.A.; Cornel, J.H.; Kamp, O.; et al. Lenient versus Strict Rate Control in Patients with Atrial Fibrillation. *N. Engl. J. Med.* **2010**, *362*, 1363–1373. <https://doi.org/10.1056/nejmoa1001337>.
14. Heldt, T. Computational models of cardiovascular response to orthostatic stress. Ph.D. Dissertation, Massachusetts Institute of Technology, **2004**.
15. Lin, J.; Ngwompo, R.F.; Tilley, D.G. Development of a cardiopulmonary mathematical model incorporating a baro-chemoreceptor reflex control system. *Proc. Inst. Mech. Eng. Part H J. Eng. Med.* **2012**, *226*, 787–803. <https://doi.org/10.1177/0954411912451823>.
16. Ursino, M.; Giannessi, M. A model of cerebrovascular reactivity including the circle of Willis and cortical anastomoses. *Ann. Biomed. Eng.* **2010**, *38*, 955–974. <https://doi.org/10.1007/S10439-010-9923-7/TABLES/2>.
17. Hennig, T.; Maass, P.; Hayano, J.; Heinrichs, S.; Hennig, T.; Maass, P.; Hayano, J.; Heinrichs, S. Exponential Distribution of Long Heart Beat Intervals During Atrial Fibrillation and Their Relevance for White Noise Behaviour in Power Spectrum. *J. Biol. Phys.* **2006**, *32*, 383–392. <https://doi.org/10.1007/S10867-006-9022-Z>.
18. Scarsoglio, S.; Guala, A.; Camporeale, C.; Ridolfi, L. Impact of atrial fibrillation on the cardiovascular system through a lumped-parameter approach. *Med. Biol. Eng. Comput.* **2014**, *52*, 905–920. <https://doi.org/10.1007/S11517-014-1192-4>.
19. Anselmino, M.; Scarsoglio, S.; Saglietto, A.; Gaita, F.; Ridolfi, L. A computational study on the relation between resting heart rate and atrial fibrillation hemodynamics under exercise. *PloS ONE.* **2017**, *12*, e0169967. <https://doi.org/10.1371/JOURNAL.PONE.0169967>.
20. Hindmarsh, A.C.; Brown, P.N.; Grant, K.E.; Lee, S.L.; Serban, R.; Shumaker, D.E.; Woodward, C.S. SUNDIALS: Suite of non-linear and differential/algebraic equation solvers. *ACM Trans. Math. Softw.* **2005**, *31*, 363–396. <https://doi.org/10.1145/1089014.1089020>.
21. Tange, O. GNU Parallel **2018**;
22. Available online: <https://doi.org/10.5281/ZENODO.1146014> .
23. Pianelli, M.; Scaglione, M.; Anselmino, M.; Caponi, D.; Garcia, P.; Cesarani, F.; Toso, E.; Raimondo, C.; Halimi, F.; Leclercq, J.F.; et al. Delaying cardioversion following 4-week anticoagulation in case of persistent atrial fibrillation after a transcatheter ablation procedure to reduce silent cerebral thromboembolism: A single-center pilot study. *J. Cardiovasc. Med.* **2011**, *12*, 785–789. <https://doi.org/10.2459/JCM.0B013E32834BA0EB>.
24. Kharche, S.R.; Mironova, G.Y.; Goldman, D.; McIntyre, C.W.; Welsh, D.G. Sensitivity analysis of a smooth muscle cell electrophysiological model. In Functional Imaging and Modeling of the Heart; Ennis, D.B., Perotti, L.E., Wang, V.Y., Eds.; Springer International Publishing: Cham, Switzerland, **2021**; Volume 12738 LNCS, pp. 540–550.

25. Matsumoto, M.; Nishimura, T. Mersenne twister. *ACM Trans. Model. Comput. Simul.* **1998**, *8*, 3–30. <https://doi.org/10.1145/272991.272995>.
26. Malone, B.P.; Minansy, B.; Brungard, C. Some methods to improve the utility of conditioned Latin hypercube sampling. *PeerJ.* **2019**, *7*, e6451. <https://doi.org/10.7717/PEERJ.6451>.
27. Kharche, S.; Lüdtke, N.; Panzeri, S.; Zhang, H. A global sensitivity index for biophysically detailed cardiac cell models: A computational approach. In *Functional Imaging and Modeling of the Heart*; Ayache, N., Delingette, H., Sermesant, M., Eds.; *Springer Berlin Heidelberg: Berlin/Heidelberg, Germany*, **2009**; pp. 366–375.
28. Hamby, D.M. A comparison of sensitivity analysis techniques. *Health Phys.* **1995**, *68*, 195–204. <https://doi.org/10.1097/00004032-199502000-00005>.
29. Zarrinkoob, L.; Ambarki, K.; Wåhlin, A.; Birgander, R.; Eklund, A.; Malm, J. Blood flow distribution in cerebral arteries. *J. Cereb. Blood Flow Metab.* **2015**, *35*, 648–654. <https://doi.org/10.1038/jcbfm.2014.241>.
30. Joseph, J.J.; Lee, T.-Y.; Goldman, D.; McIntyre, C.W.; Kharche, S.R. The role of extra-coronary vascular conditions that affect coronary fractional flow reserve estimation. In *Functional Imaging and Modeling of the Heart*; Ennis, D.B., Perotti, L.E., Wang, V.Y., Eds.; *Springer International Publishing: Cham, Switzerland*, **2021**; Volume 12738 LNCS, pp. 595–604.
31. Grande Gutierrez, N. Hemodynamic Based Thrombotic Risk Stratification in Kawasaki Disease Patients with Coronary Artery Aneurysms. Ph.D. Dissertation, Stanford University, Stanford, CA, USA, **2019**.

Chapter 3. General Discussion and Conclusions

The results presented in chapter 2 of this thesis are novel and have important implications given the present landscape of research surrounding AF and dementia. The results are especially relevant considering current accepted practices in the treatment planning for AF.

3.1. Discussion of Chapter 2 Results

3.1.1. Hypoperfusion Events

AF has consistently been independently associated with early cognitive decline and a higher risk of dementia [1–12]. For instance, the UK Whitehall II study showed that in people aged 45–69 years, AF is significantly associated with higher risk of incident dementia (HR = 1.87, 95% CI 1.37–2.55) and that longer exposure to AF is associated with faster cognitive decline compared with AF-free adults [5]. In the Atherosclerosis Risk in Communities (ARIC) Study, data were available from 12,515 participants (mean age 56.9 years) who were followed up for over 20 years. This study reported that incident AF was associated with faster global cognitive decline and higher risk of dementia after adjusting for cardiovascular diseases including ischemic stroke [2]. The US Cardiovascular Health Study demonstrated that, in the absence of clinical stroke, the cognitive function declined faster in patients experiencing incident AF compared to people with no prior AF [13]. In the Rotterdam study, AF is associated with an elevated risk of incident dementia only among people younger than 67 years (HR = 1.81, 95% CI 1.11–2.94) [6]. Similarly, the US Intermountain Heart Collaborative Study showed that the highest risk of dementia associated with AF was seen in people younger than 70 years [12]. Among the elderly (e.g., age ≥ 80 years), there is still a lack of evidence from epidemiologic studies to support an association of AF with cognitive decline and dementia, and more data from population-based studies are needed to fully elucidate this association in the elderly population, as reported by a review of studies pertaining to subjects ≥ 80 years [14].

While there is a large basis of evidence showing the independent association of AF with cognitive decline and dementia, the underlying mechanism(s) of this relationship remains unknown. Several mechanisms have been suggested, including microbleeds, micro emboli, systemic inflammation, and cerebral hypoperfusion. Potential mechanisms have been widely studied in clinical and epidemiological literature [2,15–19]. Despite this, it is still unclear which of these mechanisms, if any, are the driving factor behind cognitive decline and dementia in AF patients.

Cerebral hypoperfusion is the least studied mechanism which has been proposed, due to the difficult nature of monitoring blood flow and cerebral perfusion *in vivo*. These difficulties can be overcome through computational studies, which have been important in investigating this mechanism.

Hypoperfusion events are defined as the average blood flow rate during one heartbeat dropping below a baseline level. The 6 distal cerebral circulation regions were monitored, using the 5th percentile flow rates from an equivalent control simulation as baseline values. It was found that in all tested cases, AF caused hypoperfusion events to occur, as shown in Figure 11. It has been found previously that hypoperfusion events may be the result of hemodynamic instability caused by AF [20] which is confirmed by the present modelling. There is a lack of information on the extent to which transient hypoperfusion events cause ischemic damage to the brain tissue, however it is suggested that any instantaneous drop below 90-93% of oxygen delivery can have negative consequences [21].

3.1.2. Subclinical Cerebral Ischemia

In this work, frequency of hypoperfusion events in the distal cerebral circulation were taken to be an indicator of subclinical ischemia, which is an important driver of cognitive decline. Figure 11 shows the frequency of hypoperfusion events in the distal cerebral circulation per 5000 heart beats. Data are shown for each heart rate from 50 bpm to 130 bpm in intervals of 10. Additionally, this data is presented for each CoW variant that was modelled. It can be observed qualitatively that each variant has a unique behavior concerning hypoperfusion at varying heart rates. The heart rate which produces the highest frequency varies between the different variants, but is always in the range of 110-130 bpm, except in the case with both missing PCoAs, for which the maximum appears to be above the tested

range. The trend shared among all variants is that the hypoperfusion event frequency decreases from the maximum point as heart rate decreases (Figure 11). One variant to note is the missing A1 variant. This variant exhibited higher mean frequencies than all other variants, with the minimum frequency at 50 bpm being 2-4x higher than all other variants. The finding that ischemia increases with heart rate is consistent with previous computational modelling in the field [22]. This finding by itself would suggest that a strict rate control strategy of less than 70 bpm is ideal. Interpretation from the RACE II trial suggests that a lenient control strategy of less than 120 bpm is as beneficial as a strict regimen, with fewer negative outcomes [23]. While this analysis is important in understanding the impacts of rate control strategies on patients, it did not consider cognitive impacts of AF. The findings from the present work shows that a constant low heart rate (strict rate control) result in virtually eliminating hypoperfusion events. While the findings from the present work are theoretical, they suggest that the impact of lenient versus strict rate control should be investigated in a clinical setting. The variant with a missing A1 has been shown to be most vulnerable to hypoperfusion [24,25]. This supports the finding that the missing A1 variant is at particular risk of subclinical ischemia. This variant is present in only 6% of the population [26], however the risk of dementia or cognitive decline may be high in AF patients with this variant, as well as other risk factors such as long durations of AF and younger patients. Therefore, it is recommended that CoW geometry be taken into account in treatment planning for patients who are already at high risk for cognitive decline or dementia.

3.1.3. Hemodynamic Variability Between CoW Variants

Blood flow to the distal circulation regions was assessed qualitatively for each of the CoW variants at 90 bpm. An interesting observation is that in the variants with a missing P1 segment, i.e., variant 5 and variant 6, flow waveforms in the ipsilateral posterior circulation is phase shifted relative to flow in the other regions (Figure 13). This is an unexpected finding and has not been published in the literature. The present model is a lumped parameter model, and therefore has no spatial element. Additionally, it neglects inertial effects which would be described by inductors in the electrical model. Therefore, it should

not be assumed that the wave propagation behaviour of the model is accurate. However, this result warrants further investigation. A 1-dimensional model of the aorta and cerebral vasculature is being developed in our lab and will yield detailed data on blood flow through the CoW. While the hemodynamic differences in variants 5 and 6 are qualitatively notable, they were not associated with a marked increase in subclinical ischemia as measured in this study.

3.1.4. Sensitivity Analysis

Sensitivity analysis allows the identification of the model parameter or set of model parameters that have the greatest influence on the model output (model behaviour). Sensitivity analysis (SA) of dynamical models can be broadly classified into local sensitivity analysis and global sensitivity analysis. As can be seen in Chapter 2, sensitivity analysis was successfully used to demonstrate the prime role of intrinsic heart rate (model parameter) on hypoperfusion event frequency (model behaviour).

3.1.4.1. Local Sensitivity Analysis

Local sensitivity analysis evaluates changes in the model outputs with respect to variations in a single parameter input. The input parameters are typically changed one at a time in relatively small increments (e.g., 0.5 to 1.5-fold), and the effect of this individual parameter perturbation on the model output is calculated using local sensitivity indices. Local sensitivity analysis is suited to a deeper understanding of differential equation dynamics during system evolution. Traditionally local sensitivity analysis is performed as a derivative-based index [27,28]. For simplicity, we consider a system of ODEs defined by

$$\frac{dy}{dt}(t) = f(t, y, p), \quad y(t_0) = y_0 \quad \text{Equation 23}$$

where p represents the vector of model parameters, $p = [p_1, p_2, p_3, \dots, p_n]$. The derivative-based index is defined as

$$S_{ij} = \frac{p_j}{y_{i,0}} \frac{dy_i}{dp_j} \quad \text{Equation 24}$$

where $y_{i,0} \neq 0$. In this manner S_{ij} represents the alterations in y_i effected by a small change, dp_j in the given parameter. S_{ij} in general, is a function of time. Derivative based sensitivity analysis has been used to analyze lumped parameter hemodynamic models [22].

3.1.4.2. Global Sensitivity Analysis

Global sensitivity analysis ranks the model parameters according to the degree to which they influence the model output. This type of global sensitivity analysis is commonly performed in a probabilistic manner by evaluating the model for multiple sets of randomly and independently selected input values drawn, for instance, from uniform distributions over suitable intervals. The output, being a function of the randomized inputs, thus also becomes a random variable. If the inputs are sampled independently, the variance of the output distribution can be decomposed into contributions by individual inputs, pairs, triplets and so forth. This procedure is well known in statistics as ‘analysis of variance’ [30], and several authors have contributed to improve its computational efficiency for sensitivity analysis [31].

In a global sensitivity analysis, all parameters are varied simultaneously over the entire parameter space, which allows for simultaneous evaluation of the relative contributions of each individual parameter as well as the interactions between parameters to the model output variance. Given that model inputs can span a wide range (e.g., the intrinsic heart rate, cardiac elastances, vascular compliances and resistances) for hemodynamic models such as considered in this thesis, global sensitivity analysis is an innovative approach for determining which reactions and processes contribute most to the behavior of the overall system. In this work, multiple global sensitivity analysis methods were used.

Another set of traditional sensitivity indices are Sobol’s parameters. Sobol’s method is a variance-based method where model parameters are perturbed, and the variance of the model behaviour is computed to provide Sobol indices [32]. Sobol sensitivity analysis determines the contribution of each input parameter, and its interactions, to the overall model output variance. Sobol sensitivity analysis is intended to determine how much of the variability in model output is dependent upon each of the input parameters, either a single parameter or multiple independent parameters. The decomposition of the output variance in a Sobol sensitivity analysis employs the same principal as the classical analysis of

variance in a factorial design. It should be noted that Sobol sensitivity analysis is not intended to identify the cause of the input variability. It indicates what impact is and the extent of the impact on the model output [31,33].

Another global SA method is based on partial rank correlation coefficient (PRCC), as used in Chapter 2. To compute PRCC, first the normally distributed parameters (x_i) as well as the observed outputs (y_j) were rank transformed. Then, the linear effects of other additional variables were accounted for by expressing each as a linear regression of the inputs,

$$\hat{x}_i = a_0 + \sum_{\substack{k=1 \\ k \neq 0}}^N a_k x_k, \text{ and } \hat{y}_j = b_0 + \sum_{\substack{k=1 \\ k \neq 0}}^N b_k x_k \quad \text{Equation 25}$$

which provides residuals defined as $r_{x_i} = x_i - \hat{x}_i$, $r_{y_j} = y_j - \hat{y}_j$. PRCC is defined as the correlation among these residuals normalized by their respective variances, i.e.

$$\text{PRCC}(x_i, y_j) = \frac{\text{Cov}(r_{x_i}, r_{y_j})}{\text{Var}(r_{x_i})\text{Var}(r_{y_j})} \quad \text{Equation 26}$$

As evident in Equation 26, PRCC assumes an underlying statistical model that is linear (regression), and assumption of monotonicity provides the strength of the linear relationship between a given pair of parameter and output [34,35]. The range of PRCC indices is from -1 to $+1$ by its mathematical definition in Equation 26. This is the index that was used in the presented work.

The global information-theoretic sensitivity index was developed in a previous study [27]. It constitutes deterministic quantification of the correlation between modelling parameters, which included initial conditions, to model responses. Through multiple evaluations of the model (more than 105) for randomly selected configurations of parameters including initial conditions, one obtains empirical samples of model responses, from which the underlying probability distributions of responses are computed. Thus, although the models under investigation are deterministic, parameters and responses are randomized. The sensitivity indexing consists of determining statistical relations between parameters and responses. The impact of individual parameters on a particular model response can be quantified in terms of the correlation between the sampling distributions of the parameters and the

resulting responses distributions. In the information-theoretic approach, a universally applicable correlation measure, the mutual information index (MI_i), was chosen as the mutual information between an individual parameter X_i and a model response Y , and the total information, or response entropy, in the system as

$$MI_i = \frac{I(X_i; Y)}{H(Y)} \quad \text{Equation 27}$$

where $I(X_i; Y)$ is the mutual information and $H(Y)$ is the response entropy. Further details for computing $I(X_i; Y)$ and $H(Y)$ are discussed elsewhere [27]. In brief, the entropy $H(Y)$ quantifies the sampling-induced uncertainty of the response values (i.e., the "spread" of the distribution of Y), and the mutual information is the portion of this uncertainty that parameter X_i accounts for. Thus, every model response is associated with several MI_i related to parameter i . This set of MI_i for every model response can be further normalised to the maximal value in that set of MI_i to uniformly reveal the relative influence of parameters on that particular response. It is important to inform developed models regarding information content in order to permit subject specific identification.

In applying PRCC analysis, the model parameters were evaluated with respect to their correlation to model outputs. The model was evaluated six times, representing each of the common CoW variants. As has been suggested by previous modelling efforts [22], intrinsic heart rate was confirmed to be the primary factor influencing the frequency of hypoperfusion events. It was expected that intrinsic heart rate would have a high correlation with hypoperfusion frequency, both because it had been shown to be linked by previous modelling, and because it had been shown by the present work that changes in intrinsic heart rate lead to changes in hypoperfusion frequency. This hypothesis was confirmed by the PRCC analysis showing that intrinsic heart rate was the highest ranked model parameter for each of the CoW variants. Additionally, it was found that right ventricular diastolic and systolic elastance respectively were the highest ranked PRCC values after intrinsic heart rate. This result is likely explained by the fact that increased right ventricular contractility leads to increased preload in the left heart, and consequently increased cardiac output. There are several mechanisms by which increased cardiac output may increase cerebral blood flow [36], thereby reducing the frequency of cerebral hypoperfusion events. An

investigation into the dynamics of this phenomenon is worthwhile, however as treatment of AF via increased right ventricular contractility is not a promising treatment path due to the relation between sympathetic innervation and AF, a detailed investigation into this phenomenon is beyond the scope of this work.

3.2. General Conclusions and Reflections

The aims of this thesis were twofold. The first was to develop an open-source model of cerebral blood flow capable of simulating pathological conditions for experimentally and clinically relevant investigations. Second, was to use the model to investigate the impacts of AF on localized cerebral blood flow with respect to variations in cerebrovascular anatomy and model parameters.

The first aim was achieved through the incremental development of a lumped parameter hemodynamic model for a research project within the laboratory [37]. This model contained mechanistic descriptions of the human whole-body circulation and four chamber heart and was therefore a suitable foundation on which to construct the atrial fibrillation model. The model was implemented using modular C code, which made it adaptable and extensible, therefore it was possible to extend the model to include the cerebral circulation. This extensibility is what made the model valuable for an investigation into cerebral blood flow dynamics. This workflow emphasized the importance for mathematical models to be modular and extensible, and therefore to be widely applicable to a range of research topics. Additionally, there was an emphasis on quality documentation of the model so that it could be understood, reproduced, and extended by peers. This principle was demonstrated by researchers such as Ursino [38] and Heldt [39], who documented the mechanistic equations used to a high level of detail, inspiring the same level of detail in the present work.

The second aim was achieved by applying the model to explore the dynamics of the system under various experimental conditions, and to understand the dynamic mathematical behavior of the model. The model was first simulated with parameters representing a healthy individual and the results were compared to literature values of blood flow rates and pressures to ensure that the model and simulation method produced realistic

predictions. After this, the model was thoroughly investigated using sensitivity analysis techniques previously described to deepen our understanding of model dynamics and to show that the model behaves as expected. Sensitivity analysis entailed simulating the model for a total of 10^5 instances to sample the entire parameter space within and beyond physiological levels. Finally, the model was simulated under an array of physiological conditions, particularly varying intrinsic heart rate and CoW geometry. The primary findings of this investigation were that both intrinsic heart rate and cerebral vascular geometry have an impact on frequency of cerebral hypoperfusion during AF. Particularly, it was discovered that patients with a missing A1 segment of the CoW are at highest risk for cerebral hypoperfusion. It follows that cerebral vascular structure is an important consideration in the treatment of AF patients at high risk of early cognitive decline and dementia.

3.3. Future Work

Computational modelling is now an accepted research instrument. It is also increasingly being used in basic science, clinical research and clinical decision making. The future goal for this work is for further development and application of the mathematical model, as well as uptake and further investigation into modelling outcomes from experimental and clinical researchers. Further development of the presented model will be driven primarily by the author and the lab but remains open for any peers who wish to collaborate or to develop their own projects based on this open-source work. Planned future development involves investigation into alternative treatment methods for AF such as catheter ablation or external pacing control. Aside from investigation into AF, the model may also be extended to include a highly detailed autoregulation mechanism. This subsection describes the future applications and development of the model developed in this thesis.

3.3.1. Application of Model in Basic Science Research

In a recent study it was found that microvascular blood flow is highly organized at multiple spatial scales. This organization is disturbed by conditions such as hypoxia [40]. A future application of the model presented in this thesis will be to include such multiscale data by

further developing the model's boundary conditions. A second recent study also found that changes in blood viscosity regulate the hyperemic response [41]. Since the presented model can be personalized using imaging data which must be obtained under hyperemic conditions (mimicking exercise), the boundary conditions can be further developed to incorporate the non-Newtonian behavior of blood in terms of vessel specific viscosity. The microvasculature plays a significant role in delivery of oxygen to skeletal muscle [42] and cerebral tissue which in turn may affect large vessel hemodynamics. Incorporation of such micro-macro vasculature feedback mechanisms into our cerebral model will provide further pathophysiological insights into blood flow in the Circle of Willis and the impacts of transient ischemia. In line with the oxygen supply research focus in our university, extending of the microvasculature responses to large vessels is essential, and may permit development of new biomarkers. One such effect is the control of cerebral blood flow by cerebral autoregulation [43]. A physiologically accurate cerebral autoregulation model has been described, which will be used in the future to extend our model [44]. It has been found that obesity has a deleterious impact on vascular reactivity, microvascular network and wall structure [45]. Our model will be extended based on experimental data to investigate the implications of these changes for cerebral blood flow.

3.3.2. Applications of Model in Clinical Research

Imaging data acquired by the McIntyre Group strongly suggest disease induced dysfunction of blood flow in organs. Our ongoing efforts aim to uncover the cause-effect relationships, thus reducing the gap between clinical research and treatment, in addition to generating novel biomarkers such as fractal dimension [46]. The efficacy of disruptive novel treatments such as therapeutic hypothermia was tested in our group using our *in silico* models [37,47]. This model is the latest in our suite of evidence generating computational descriptions of physiological processes.

High dimensional models now provide the capability to undertake *in silico* clinical trials [48]. However, high dimensional models currently cannot provide recommendations in real time, whilst rapid decision-making is important in our hospitals. It is therefore essential to further develop the presented model, since it has the potential to provide a rapid scaffold on the clinician's desktop. Multiscale *in silico* models are being used in clinical trials to

predict outcomes of deleterious cerebral conditions [49]. We believe that reduced order models may generate new knowledge as well as provide computational efficient research tools.

Cognitive decline and dementia have been recognized as potential outcomes of cardiac disease [6]. Clinical imaging studies by Dr. Udunna Anazodo suggest a close nexus between the imageable structure and cerebral dysfunction of relevance. Our model will be used to generate evidence for this hypothesis [50]. A large number of biophysical factors involved in the development of Alzheimer's disease can now be identified, and prevention strategies have been developed due to the availability of novel vasculature computational models [51]. Our model has contributed to enabling *in silico* computational trials in our university's research groups.

3.4. References

1. Nishtala, A.; Piers, R.J.; Himali, J.J.; Beiser, A.S.; Davis-Plourde, K.L.; Saczynski, J.S.; McManus, D.D.; Benjamin, E.J.; Au, R. Atrial fibrillation and cognitive decline in the Framingham Heart Study. *Hear. Rhythm* **2018**, *15*, doi:10.1016/j.hrthm.2017.09.036.
2. Chen, L.Y.; Norby, F.L.; Gottesman, R.F.; Mosley, T.H.; Soliman, E.Z.; Agarwal, S.K.; Loehr, L.R.; Folsom, A.R.; Coresh, J.; Alonso, A. Association of atrial fibrillation with cognitive decline and dementia over 20 years: The ARIC-NCS (Atherosclerosis Risk in Communities Neurocognitive Study). *J. Am. Heart Assoc.* **2018**, *7*, 1–13, doi:10.1161/JAHA.117.007301.
3. Peters, R.; Poulter, R.; Beckett, N.; Forette, F.; Fagard, R.; Potter, J.; Swift, C.; Anderson, C.; Fletcher, A.; Bulpitt, C.J. Cardiovascular and biochemical risk factors for incident dementia in the hypertension in the very elderly trial. *J. Hypertens.* **2009**, *27*, doi:10.1097/HJH.0b013e32832f4f02.
4. Tilvis, R.S.; Kähönen-Väre, M.H.; Jolkkonen, J.; Valvanne, J.; Pitkala, K.H.; Strandberg, T.E. Predictors of Cognitive Decline and Mortality of Aged People over a 10-Year Period. *Journals Gerontol. - Ser. A Biol. Sci. Med. Sci.* **2004**, *59*, doi:10.1093/gerona/59.3.m268.
5. Singh-Manoux, A.; Fayosse, A.; Sabia, S.; Canonico, M.; Bobak, M.; Elbaz, A.; Kivimäki, M.; Dugravot, A. Atrial fibrillation as a risk factor for cognitive decline and dementia. *Eur. Heart J.* **2017**, *38*, doi:10.1093/eurheartj/ehx208.
6. De Bruijn, R.F.A.G.; Heeringa, J.; Wolters, F.J.; Franco, O.H.; Stricker, B.H.C.; Hofman, A.; Koudstaal, P.J.; Ikram, M.A. Association Between Atrial Fibrillation and Dementia in the General Population. *JAMA Neurol.* **2015**, *72*, 1288–1294, doi:10.1001/JAMANEUROL.2015.2161.

7. Rusanen, M.; Kivipelto, M.; Levälahti, E.; Laatikainen, T.; Tuomilehto, J.; Soininen, H.; Ngandu, T. Heart Diseases and Long-Term Risk of Dementia and Alzheimer's Disease: A Population-Based CAIDE Study. *J. Alzheimer's Dis.* **2014**, *42*, doi:10.3233/JAD-132363.
8. Haring, B.; Leng, X.; Robinson, J.; Johnson, K.C.; Jackson, R.D.; Beyth, R.; Wactawski-Wende, J.; von Ballmoos, M.W. yle.; Goveas, J.S.; Kuller, L.H.; et al. Cardiovascular disease and cognitive decline in postmenopausal women: results from the Women's Health Initiative Memory Study. *J. Am. Heart Assoc.* **2013**, *2*, doi:10.1161/JAHA.113.000369.
9. Marzona, I.; O'Donnell, M.; Teo, K.; Gao, P.; Anderson, C.; Bosch, J.; Yusuf, S. Increased risk of cognitive and functional decline in patients with atrial fibrillation: Results of the ONTARGET and TRANSCEND studies. *CMAJ* **2012**, *184*, doi:10.1503/cmaj.111173.
10. Dublin, S.; Anderson, M.L.; Haneuse, S.J.; Heckbert, S.R.; Crane, P.K.; Breitner, J.C.S.; McCormick, W.; Bowen, J.D.; Teri, L.; McCurry, S.M.; et al. Atrial fibrillation and risk of dementia: A prospective cohort study. *J. Am. Geriatr. Soc.* **2011**, *59*, doi:10.1111/j.1532-5415.2011.03508.x.
11. Marengoni, A.; Qiu, C.; Winblad, B.; Fratiglioni, L. Atrial fibrillation, stroke and dementia in the very old: A population-based study. *Neurobiol. Aging* **2011**, *32*, doi:10.1016/j.neurobiolaging.2009.08.002.
12. Bunch, T.J.; Weiss, J.P.; Crandall, B.G.; May, H.T.; Bair, T.L.; Osborn, J.S.; Anderson, J.L.; Muhlestein, J.B.; Horne, B.D.; Lappe, D.L.; et al. Atrial fibrillation is independently associated with senile, vascular, and Alzheimer's dementia. *Hear. Rhythm* **2010**, *7*, doi:10.1016/j.hrthm.2009.12.004.
13. Thacker, E.L.; McKnight, B.; Psaty, B.M.; Longstreth, W.T.; Sitlani, C.M.; Dublin, S.; Arnold, A.M.; Fitzpatrick, A.L.; Gottesman, R.F.; Heckbert, S.R. Atrial fibrillation and cognitive decline: A longitudinal cohort study. *Neurology* **2013**, *81*, doi:10.1212/wnl.0b013e31829a33d1.
14. Proietti, M.; Recchia, A.; Riva, E.; Lucca, U.; Tettamanti, M.; Mannucci, P.M.; Nobili, A. Relationship between atrial fibrillation and cognitive decline in individuals aged 80 and older. *Eur. J. Intern. Med.* **2017**, *46*.
15. Alosco, M.L.; Spitznagel, M.B.; Sweet, L.H.; Josephson, R.; Hughes, J.; Gunstad, J. Atrial fibrillation exacerbates cognitive dysfunction and cerebral perfusion in heart failure. *PACE - Pacing Clin. Electrophysiol.* **2015**, *38*, doi:10.1111/pace.12543.
16. Dietzel, J.; Haeusler, K.G.; Endres, M. Does atrial fibrillation cause cognitive decline and dementia? *Europace* **2018**, *20*, doi:10.1093/europace/eux031.
17. Takeda, S.; Sato, N.; Morishita, R. Systemic inflammation, blood-brain barrier vulnerability and cognitive / non-cognitive symptoms in Alzheimer disease: Relevance to pathogenesis and therapy. *Front. Aging Neurosci.* **2014**, *6*, doi:10.3389/fnagi.2014.00171.
18. Schmidt, R.; Schmidt, H.; Curb, J.D.; Masaki, K.; White, L.R.; Launer, L.J. Early inflammation and dementia: A 25-year follow-up of the Honolulu-Asia Aging Study. *Ann. Neurol.* **2002**, *52*, doi:10.1002/ana.10265.
19. Pantoni, L. Cerebral small vessel disease: from pathogenesis and clinical characteristics to therapeutic challenges. *Lancet Neurol.* **2010**, *9*.

20. Anselmino, M.; Scarsoglio, S.; Saglietto, A.; Gaita, F.; Ridolfi, L. Transient cerebral hypoperfusion and hypertensive events during atrial fibrillation: a plausible mechanism for cognitive impairment OPEN. *Nat. Publ. Gr.* **2016**, doi:10.1038/srep28635.
21. Slessarev, M.; Mahmoud, O.; McIntyre, C.W.; Ellis, C.G. Cerebral Blood Flow Deviations in Critically Ill Patients: Potential Insult Contributing to Ischemic and Hyperemic Injury. *Front. Med.* **2021**, *7*, doi:10.3389/fmed.2020.615318.
22. Saglietto, A.; Scarsoglio, S.; Ridolfi, L.; Gaita, F.; Anselmino, M. Higher ventricular rate during atrial fibrillation relates to increased cerebral hypoperfusions and hypertensive events. *Sci. Reports 2019 91* **2019**, *9*, 1–9, doi:10.1038/s41598-019-40445-5.
23. Van Gelder, I.C.; Groenveld, H.F.; Crijns, H.J.G.M.; Tuininga, Y.S.; Tijssen, J.G.P.; Alings, A.M.; Hillege, H.L.; Bergsma-Kadijk, J.A.; Cornel, J.H.; Kamp, O.; et al. Lenient versus Strict Rate Control in Patients with Atrial Fibrillation. *N. Engl. J. Med.* **2010**, *362*, 1363–1373, doi:10.1056/nejmoa1001337.
24. Amin-Hanjani, S.; Du, X.; Pandey, D.K.; Thulborn, K.R.; Charbel, F.T. Effect of age and vascular anatomy on blood flow in major cerebral vessels. *J. Cereb. Blood Flow Metab.* **2015**, *35*, doi:10.1038/jcbfm.2014.203.
25. Fahy, P.; McCarthy, P.; Sultan, S.; Hynes, N.; Delassus, P.; Morris, L. An experimental investigation of the hemodynamic variations due to aplastic vessels within three-dimensional phantom models of the circle of willis. *Ann. Biomed. Eng.* **2014**, *42*, doi:10.1007/s10439-013-0905-4.
26. Lippert, H.; Pabst, R. *Arterial Variations in Man*; **1985**;
27. Khariche, S.; Lüdtke, N.; Panzeri, S.; Zhang, H. A Global Sensitivity Index for Biophysically Detailed Cardiac Cell Models: A Computational Approach. In Proceedings of the Functional Imaging and Modeling of the Heart; Ayache, N., Delingette, H., Sermesant, M., Eds.; Springer Berlin Heidelberg: Berlin, Heidelberg, **2009**; pp. 366–375.
28. Nygren, A.; Fiset, C.; Firek, L.; Clark, J.W.; Lindblad, D.S.; Clark, R.B.; Giles, W.R. Mathematical model of an adult human atrial cell: The role of K⁺ currents in repolarization. *Circ. Res.* **1998**, *82*, doi:10.1161/01.RES.82.1.63.
29. Ellwein, L.M.; Tran, H.T.; Zapata, C.; Novak, V.; Olufsen, M.S. Sensitivity analysis and model assessment: Mathematical models for arterial blood flow and blood pressure. *Cardiovasc. Eng.* **2008**, *8*, doi:10.1007/s10558-007-9047-3.
30. Addelman, S.; Box, G.E.P.; Hunter, W.G.; Hunter, J.S. Statistics for Experimenters. *Technometrics* **1979**, *21*, doi:10.2307/1267766.
31. Sobol', I.M. Sensitivity estimates for nonlinear mathematical models and their Monte Carlo estimation. *Math. Model. Comput. Exp.* **1993**, *1*.
32. Sobol', I.M. On the distribution of points in a cube and the approximate evaluation of integrals. *USSR Comput. Math. Math. Phys.* **1967**, *7*, doi:10.1016/0041-5553(67)90144-9.
33. Sobol, I.M. Global sensitivity indices for nonlinear mathematical models and their Monte Carlo estimates. *Math. Comput. Simul.* **2001**, *55*, doi:10.1016/S0378-4754(00)00270-6.
34. Marino, S.; Hogue, I.B.; Ray, C.J.; Kirschner, D.E. A methodology for performing global uncertainty and sensitivity analysis in systems biology. *J. Theor. Biol.* **2008**, *254*, 178–196, doi:10.1016/J.JTBI.2008.04.011.

35. Hamby, D.M. A comparison of sensitivity analysis techniques. *Health Phys.* **1995**, *68*, 195–204, doi:10.1097/00004032-199502000-00005.
36. Castle-Kirszbaum, M.; Parkin, W.G.; Goldschlager, T.; Lewis, P.M. Cardiac Output and Cerebral Blood Flow: A Systematic Review of Cardio-Cerebral Coupling. *J. Neurosurg. Anesthesiol.* **2021**.
37. Joseph, J.J.; Hunter, T.J.; Sun, C.; Goldman, D.; Kharche, S.R.; McIntyre, C.W. Using a Human Circulation Mathematical Model to Simulate the Effects of Hemodialysis and Therapeutic Hypothermia. *Appl. Sci.* **2021**, *12*, 307, doi:10.3390/app12010307.
38. Ursino, M.; Giannessi, M. A model of cerebrovascular reactivity including the circle of Willis and cortical anastomoses. *Ann. Biomed. Eng.* **2010**, *38*, 955–974, doi:10.1007/S10439-010-9923-7/TABLES/2.
39. Heldt, T. Computational models of cardiovascular response to orthostatic stress. **2004**, 185.
40. Poole, D.C. Spatial matching of microvascular oxygen delivery to demand in skeletal muscle: Has the missing link been found? *J. Physiol.* **2021**, 599.
41. Mendelson, A.A.; Ho, E.; Scott, S.; Vijay, R.; Hunter, T.; Milkovich, S.; Ellis, C.G.; Goldman, D. Capillary module haemodynamics and mechanisms of blood flow regulation in skeletal muscle capillary networks: Experimental and computational analysis. *J. Physiol.* **2022**, doi:10.1113/JP282342.
42. Ghonaim, N.W.; Fraser, G.M.; Goldman, D.; Milkovich, S.; Yang, J.; Ellis, C.G. Evidence for role of capillaries in regulation of skeletal muscle oxygen supply. *Microcirculation* **2021**, *28*, doi:10.1111/micc.12699.
43. Duffin, J.; Hare, G.M.T.; Fisher, J.A. A mathematical model of cerebral blood flow control in anaemia and hypoxia. *J. Physiol.* **2020**, 598, doi:10.1113/JP279237.
44. Payne, S. *Cerebral Flow in the Brain Control of Blood Autoregulation*; 2016;
45. Stapleton, P.A.; James, M.E.; Goodwill, A.G.; Frisbee, J.C. Obesity and vascular dysfunction. *Pathophysiology* **2008**, *15*, doi:10.1016/j.pathophys.2008.04.007.
46. Kharche, S.R.; So, A.; Salerno, F.; Lee, T.-Y.; Ellis, C.; Goldman, D.; McIntyre, C.W. Computational Assessment of Blood Flow Heterogeneity in Peritoneal Dialysis Patients' Cardiac Ventricles. *Front. Physiol.* **2018**, *9*, 511, doi:10.3389/fphys.2018.00511.
47. Kharche, S.R.; Lemoine, S.; Tamasi, T.; Hur, L.; So, A.; McIntyre, C.W. Therapeutic Hypothermia Reduces Peritoneal Dialysis Induced Myocardial Blood Flow Heterogeneity and Arrhythmia. *Front. Med.* **2021**, *8*, doi:10.3389/fmed.2021.700824.
48. Padmos, R.M.; Józsa, T.I.; El-Bouri, W.K.; Konduri, P.R.; Payne, S.J.; Hoekstra, A.G. Coupling one-dimensional arterial blood flow to three-dimensional tissue perfusion models for in silico trials of acute ischaemic stroke. *Interface Focus* **2021**, *11*, doi:10.1098/rsfs.2019.0125.
49. Józsa, T.I.; Padmos, R.M.; Samuels, N.; El-Bouri, W.K.; Hoekstra, A.G.; Payne, S.J. A porous circulation model of the human brain for in silico clinical trials in ischaemic stroke. *Interface Focus* **2021**, *11*, doi:10.1098/rsfs.2019.0127.
50. Anazodo, U.C.; Shoemaker, J.K.; Suskin, N.; St. Lawrence, K.S. An investigation of changes in regional gray matter volume in cardiovascular disease patients, pre and post cardiovascular rehabilitation. *NeuroImage Clin.* **2013**, *3*, 388–395, doi:10.1016/j.nicl.2013.09.011.

51. Uleman, J.F.; Quax, R.; Melis, R.J.; Hoekstra, A.; Gm, M.; Rikkert, O. An individualized systems model to optimize Alzheimer's disease prevention strategies. *Alzheimer's Dement.* **2021**, *17*, e050885, doi:10.1002/ALZ.050885.

Appendices

A1. Model Parameter Table

Symbol	Description	Value	Ref.
t_{resp}	Respiration frequency	0.2 Hz	[1]
$E_{dias,lv}$	Left ventricular diastolic elastance	0.13 ml mmHg ⁻¹	[1]
$E_{sys,lv}$	Left ventricular systolic elastance	2.5 ml mmHg ⁻¹	[1]
$E_{dias,rv}$	Right ventricular diastolic elastance	0.07 ml mmHg ⁻¹	[1]
$E_{sys,rv}$	Right ventricular systolic elastance	1.3 ml mmHg ⁻¹	[1]
$E_{dias,la}$	Left atrial diastolic elastance	0.5 ml mmHg ⁻¹	[1]
$E_{sys,la}$	Left atrial systolic elastance	0.61 ml mmHg ⁻¹	[1]
$E_{dias,ra}$	Right atrial diastolic elastance	0.3 ml mmHg ⁻¹	[1]
$E_{sys,ra}$	Right atrial systolic elastance	0.74 ml mmHg ⁻¹	[1]
R_{sup}	Superior vena cava resistance	0.06 mmHg s ml ⁻¹	[1]
R_{ab}	Abdominal vena cava resistance	0.01 mmHg s ml ⁻¹	[1]
R_{inf}	Inferior vena cava resistance	0.015 mmHg s ml ⁻¹	[1]
R_{tri}	Tricuspid valve resistance	0.005 mmHg s ml ⁻¹	[1]
R_{ro}	Right ventricular outlet resistance	0.003 mmHg s ml ⁻¹	[1]
R_{pa}	Pulmonary arterial resistance	0.08 mmHg s ml ⁻¹	[1]
R_{pv}	Pulmonary venous resistance	0.01 mmHg s ml ⁻¹	[1]
R_{mv}	Mitral valve resistance	0.01 mmHg s ml ⁻¹	[1]
R_{lo}	Left ventricular outlet resistance	0.006 mmHg s ml ⁻¹	[1]
$R_{up,1}$	Upper body arterial resistance	8.1 mmHg s ml ⁻¹	Estimated
$R_{up,2}$	Upper body venous resistance	0.5 mmHg s ml ⁻¹	Estimated
$R_{sp,1}$	Splanchnic circulation arterial resistance	3.0 mmHg s ml ⁻¹	[1]
$R_{sp,2}$	Splanchnic circulation venous resistance	0.18 mmHg s ml ⁻¹	[1]

$R_{kid,1}$	Kidney arterial resistance	4.1 mmHg s ml ⁻¹	[1]
$R_{kid,2}$	Kidney venous resistance	0.3 mmHg s ml ⁻¹	[1]
$R_{ll,1}$	Lower body arterial resistance	3.6 mmHg s ml ⁻¹	[1]
$R_{ll,2}$	Lower body venous resistance	0.3 mmHg s ml ⁻¹	[1]
R_f	Cerebral spinal fluid formation resistance	2380 mmHg s ml ⁻¹	[2]
R_o	Cerebral spinal fluid outflow resistance	526.3 mmHg s ml ⁻¹	[2]
R_{cpv}	Cerebral proximal venous resistance	0.88 mmHg s ml ⁻¹	[2]
$R_{c,pms}$	Resistances of the collateral anastomoses from the posterior to the middle territories	120 mmHg s ml ⁻¹	[2]
$R_{c,ams}$	Resistances of the collateral anastomoses from the anterior to the middle territories	105 mmHg s ml ⁻¹	[2]
$R_{c,pp}$	Resistance of the collateral anastomoses between posterior territories	75 mmHg s ml ⁻¹	[2]
$R_{c,aa}$	Resistance of the collateral anastomoses between anterior territories	22.0 mmHg s ml ⁻¹	[2]
R_{PCA1}	Precommunicating posterior cerebral artery resistance	0.764 mmHg s ml ⁻¹	[2]
R_{PCA2}	Postcommunicating posterior cerebral artery resistance	3.6063 mmHg s ml ⁻¹	[2]
R_{PCoA}	Posterior communicating artery resistance	90.98 mmHg s ml ⁻¹	[2]
R_{ACA1}	Precommunicating anterior cerebral artery resistance	3.7912 mmHg s ml ⁻¹	[2]
R_{ACA2}	Postcommunicating anterior cerebral artery resistance	1.6227 mmHg s ml ⁻¹	[2]
R_{ACoA}	Anterior communicating artery resistance	14.9228 mmHg s ml ⁻¹	[2]
R_{ICA}	Internal carotid artery resistance	0.5689 mmHg s ml ⁻¹	[2]
R_{BA}	Basilar artery resistance	0.4501 mmHg s ml ⁻¹	[2]
C_{sup}	Superior vena cava capacitance	15.0 ml mmHg ⁻¹	[1]
C_{ab}	Abdominal vena cava capacitance	25.0 ml mmHg ⁻¹	[1]

C_{inf}	Inferior vena cava capacitance	2.0 ml mmHg ⁻¹	[1]
C_{pa}	Pulmonary arterial capacitance	4.3 ml mmHg ⁻¹	[1]
C_{pv}	Pulmonary venous capacitance	8.4 ml mmHg ⁻¹	[1]
C_a	Aortic capacitance	2.0 ml mmHg ⁻¹	[1]
C_{up}	Upper body capacitance	7.0 ml mmHg ⁻¹	[1]
C_{sp}	Splanchnic circulation capacitance	55.0 ml mmHg ⁻¹	[1]
C_{kid}	Kidney circulation capacitance	15.0 ml mmHg ⁻¹	[1]
C_{ll}	Lower body circulation capacitance	19.0 ml mmHg ⁻¹	[1]
C_{ICA}	Internal carotid artery capacitance	0.0034 ml mmHg ⁻¹	[2]
C_{BA}	Basilar artery capacitance	0.0017 ml mmHg ⁻¹	[2]
C_{dn}	Total distal cerebral capacitance	0.2 ml mmHg ⁻¹	[2]

Table 4. All relevant baseline model parameters for the lumped parameter cerebral model detailed in Chapter 2.

A2. List of Hemodynamic Simulations Research Landscape

#	Purpose of study.	Platform used.	Reference.
Lumped parameter.			
1	Personalization	In-house codes	[3]
2	Physiological investigation	In-house code	[4]
3	Surgery	Crimson	[5]
4	Surgery	Crimson	[6]
5	Cerebral blood flow pathophysiology	In-house scripts	[7]
6	Blood flow pathophysiology	in-house scripts	[8]
7	Novel modelling framework	In-house scripts	[9]
1D modelling.			
8	Cerebral blood flow pathophysiology	In-house codes	[10]
9	Physiological investigation	In-house codes	[11]
10	Physical/numerical investigation	in-house codes	[12]

11	Comparison of 1D methods to 3D and in-vivo	SolidWorks (3D modelling), MeshSim (3D meshing), in-house codes: Nektar1D (1D simulation), CRIMSON (3D simulation)	[13]
12	Presentation of whole-body arterio-venous 1D vascular model.	In-house codes	[14]
3D modelling.			
13	Physiological Investigation	Mimics (meshing), Comsol Multiphysics (CFD)	[15]
14	Physiological investigation	SEPRAN	[16]
15	Physiological investigation	ANSYS CFX v. 10.0	[17]
16	Surgical device evaluation	ICEM-ANSYS v12 (mesh), ANSYS-CFX v12 (simulation)	[18]
17	Validation of imaging methodology	ANSYS FLUENT	[19]
18	Comparison of CFD and PC-MRI	MeVisLab 2.3 and Blender 2.68a (segmentation), ANSYS ICEM-CFD 14.0 (meshing), ANSYS Fluent 14.0 (simulation)	[20]

Table 5. A compiled list of studies focussing on hemodynamic simulation. Studies are divided by modelled dimensionality (i.e., 0D, 1D or 3D). The table includes the purpose of the study, and the platform used.

A3. Code Availability

The open-source code is hosted at <https://github.com/tmhnt/cerebral-0D-model> and is available for free use under the GNU GPL V3.0 license. The code has been tested for use on Red Hat Linux and MacOS 11 and 12.

A4. Open-Source Intracranial Aneurysm CFD Modelling Workflow

In this chapter, a working 3D model of cerebral arteries is provided. The model is designed to assist uptake by new users in experimental laboratories. The model provides:

- a) 18 geometries obtained from the Aneurisk repository provided by Emory University (<http://ecm2.mathcs.emory.edu/aneuriskweb/index>).
- b) Working finite element meshes of the geometries.
- c) Physiological boundary conditions.
- d) Steady state simulation models suitable for use on laptops and large clusters.
- e) Transient simulation models to extend the steady state results.

A4.1. Intracranial Aneurysms

Another pathology of the heart brain axis which can lead to devastating consequences is the progression of Intracranial Aneurysm (IA). An aneurysm is a pathological thinning of the arterial wall, which leads to ballooning of the artery and loss of structural integrity. There are three types of aneurysms, saccular, fusiform, and dissecting. The most common of these, around 90% [21], is the saccular aneurysm, and this will be the focus of this work. IAs are aneurysms that form on any of the cerebral arteries. IAs are relatively common, occurring in around 1-5% of the population [22] and while most are completely asymptomatic, in some cases they can rupture, causing blood to leak into the cerebrospinal fluid, which is called subarachnoid hemorrhage (SAH). SAH is a devastating event, with a mortality rate of 40-50% [23] and leaving surviving patients with lifelong complications. The vast majority of IAs are discovered incidentally, meaning they are found during screening for unrelated illness. Improvements in quality of medical imaging, as well as increased usage has led to increased number of detected unruptured IAs overall [24]. Risk of SAH for patients with no prior history is relatively low, around 1-2% per year, which leaves specialists with the difficult decision to treat, survey, or do nothing to patients with unruptured IA. The risk for treatment is not negligible, and since the vast majority of IAs will never rupture, the decision to treat or not is a difficult one. It requires knowledge of

which IAs are likely to rupture and which are not. Unfortunately, the mechanisms leading to rupture are not well understood, and these decisions are frequently based on crude metrics such as shape and size of the aneurysm. Thus, there is a need for improved methods for distinguishing unruptured IAs that will rupture, from ones that won't.

Many factors have been identified as being associated with increased risk for IA formation and rupture. These include physiological, genetic, and hemodynamic factors. The baseline risk for the average person to have an IA is about 1-5% [22]. This risk is twice as high for females [25]. Another risk factor is age; this is thought to be the case because the artery walls are slowly degraded over time, explaining the very low prevalence in young people [26,27]. The most significant risk factors identified are smoking, and hypertension, which are associated with an 8-fold increase in risk for aneurysm formation [28]. Both factors are thought to be the cause of increased hemodynamic stress, leading to the increased risk. The final risk factor is family history of IA. Individuals who have first degree relatives with IA are at 3-7 times the risk of the general population for having IA [29]. This factor lends to the theory that there is a genetic basis for the formation of IA.

Although the process of IA rupture is still not fully understood, there are some characteristics which have been used to identify IAs at high risk for rupture. IA rupture risk is primarily assessed by observing the geometry of the aneurysm. This is done by means of high-resolution medical imaging. Such imaging techniques include X-ray angiography, magnetic resonance imaging and ultrasound. The primary feature used to assess IAs is the size, with sizes greater than 10mm being categorized as high risk. Another feature is the presence of blebs, small protrusions, or bumps on the surface of the aneurysm. Finally, aneurysm growth is taken to be a sign of extremely high rupture risk.

Study of the aneurysm lifecycle can be broken down into 3 major phases, formation, growth, and rupture. The first two of these phases have been greatly elucidated by biological research, and the last of which is still somewhat poorly understood.

Formation of IA is understood to be a result of the interaction of several genetic, mechanical, and hemodynamic mechanisms [30]. The structure of the arterial wall is highly specific and tuned to the particular forces that it experiences continually throughout an individual's lifetime. There are three layers or 'tunica' to its structure, the tunica intima,

tunica media, and tunica adventitia. The Tunica intima is composed of endothelial cells, which cover the lumen of the vessel, and an internal elastic lamina, which is a layer of highly elastic connective tissue. The tunica media is comprised mainly of smooth muscle cells, which provide the vessel with tensile strength and allow it to contract or dilate in response to environmental stimuli. The tunica adventitia is made up mainly of connective tissue, and in most vessels an external elastic lamina which connects the vessel to surrounding tissue and maintains shape. IA initiation begins as pathological changes in the composition and structure of the arterial wall. These changes occur very slowly, over the course of an individual's lifetime, which explains the low occurrence of IA in young people [31]. As mentioned previously, there is indication that genetic factors play a role in aneurysm formation. Some genome wide association studies have shown links between mutations to extracellular matrix and connective tissue encoding and increased risk for IA formation [32,33]. In addition to risk factors previously mentioned, arteries in the cerebral circulation, particularly in the Circle of Willis (Figure 1) are particularly prone to aneurysm formation [25,34]. This is due to several structural aspects unique to cerebral arteries, including: a thin tunica adventitia, absence of the external elastic lamina, decreased elastic fiber density in the tunica media, and being surrounded by cerebrospinal fluid, rather than connective tissue [35,36].

Currently treatment is recommended for patients with aneurysms larger than 10mm in size, with smaller aneurysms often being surveyed for growth, which is a sign of high risk for rupture, and aneurysms around 10mm being up to the discretion of the specialist. Additionally, low risk aneurysms may be left without surveillance if the patient is nearing the end of life or surveillance will cause significant disruption relative to the low rupture risk. There are several treatment options to be considered. Surgical techniques include clipping, endovascular coiling, and flow diverting stents. These options represent the more aggressive treatment methods. Clipping is a surgical technique in which a metal clip is placed around the exterior of the aneurysm, usually around the neck, to pinch and prevent blood flow into the aneurysm. Endovascular coiling is a procedure in which a long catheter is inserted into an artery, usually the femoral artery, and fed up to the location of the aneurysm. The catheter is then used to dispense a thin platinum wire into the aneurysm bulb, which then coils up and seals blood flow to the aneurysm. Flow diversion is a

technique in which a stent-like implant which diverts some blood flow away from the site of the aneurysm, allowing it to recover and heal from hemodynamic stress it may have been experiencing. Non-surgical treatment options include medications to manage high blood pressure or other cardiovascular risk factors, as well as lifestyle changes such as quitting smoking.

A4.2. Aneurysm Structures

The geometries were obtained from the Aneurisk repository (<http://ecm2.mathcs.emory.edu/aneuriskweb/index>). The repository provides data driven volume structures of human cerebral arteries suffering from a spectrum of aneurysms [37]. A number of geometries are provided to the users. The repository provides finite element meshes of the volumes which are illustrated in Figures 15 and 16 The geometries, hemodynamic models, and representative results, as well as documentation can be found at our github: [github/mccssk22](https://github.com/mccssk22). The interested user can access the underlying DICOM images from the original repository.

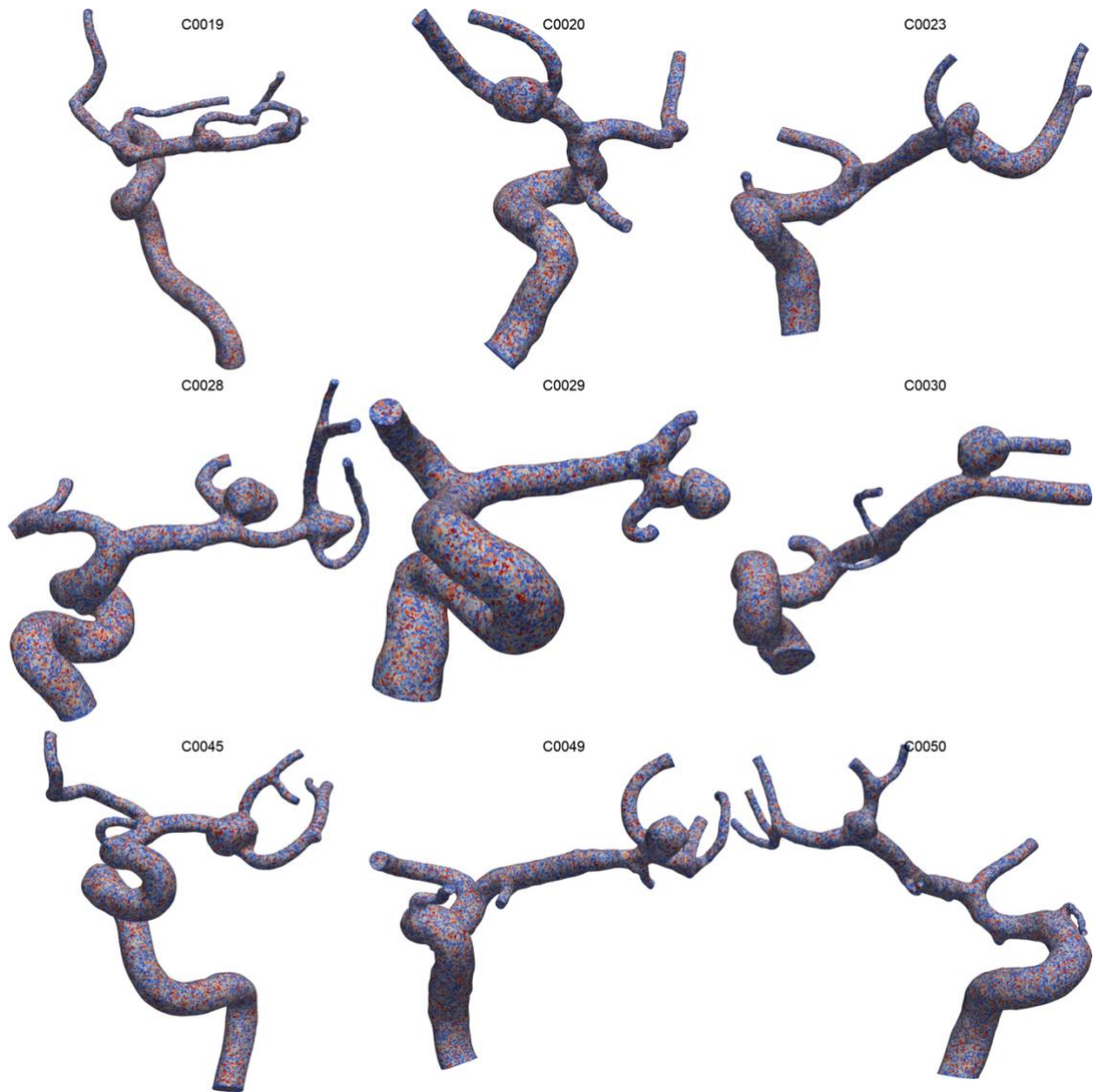


Figure 15. Basic visualization of 9 geometries selected from the Aneurisk dataset. All selected geometries contain at least one aneurysm on the MCA.

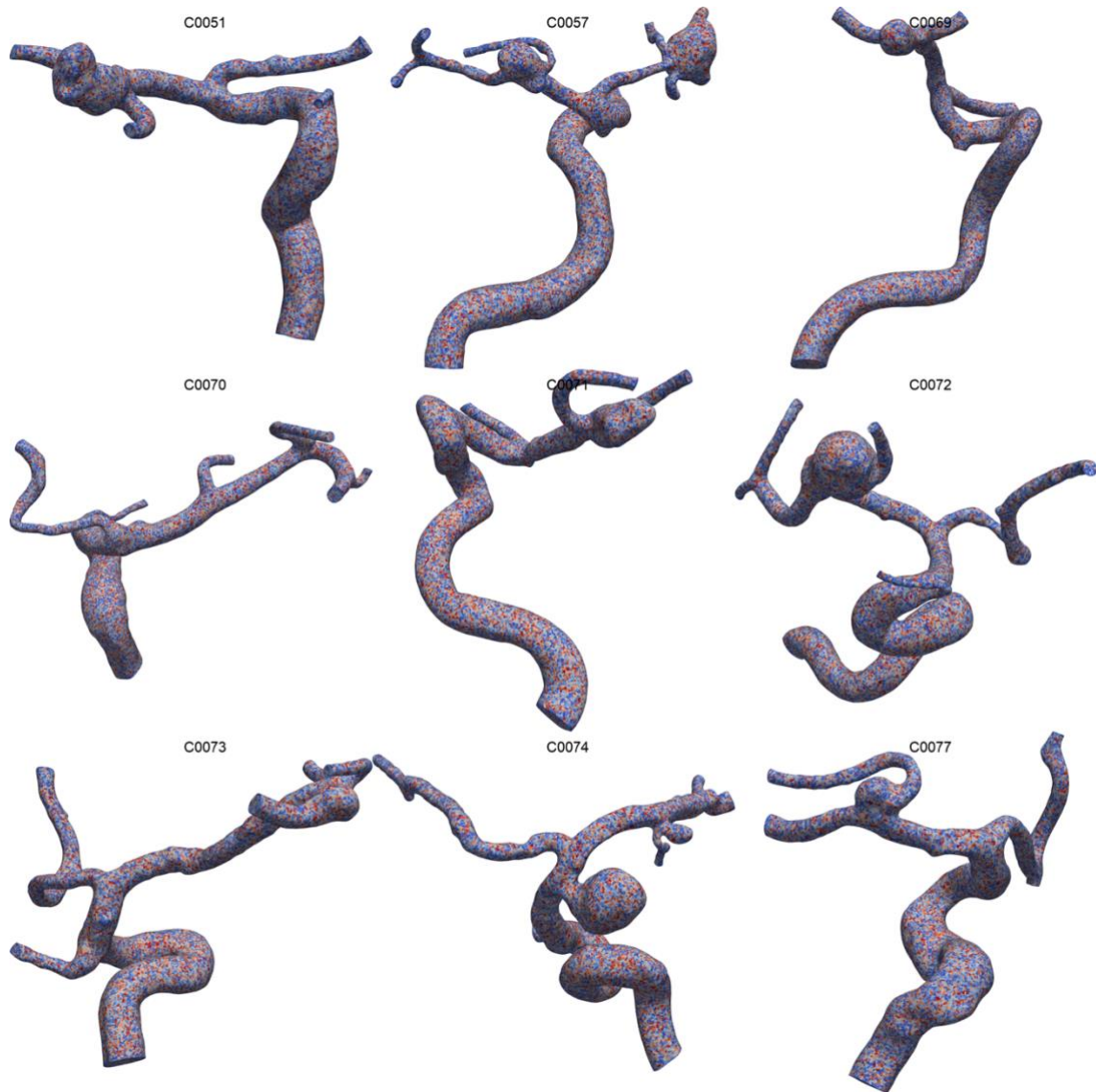


Figure 16. Basic visualization of 9 geometries selected from the Aneurisk dataset. All selected geometries contain at least one aneurysm on the MCA.

A4.3. Boundary Conditions

In the wider literature, either flow or pressure conditions are applied at the boundaries of hemodynamic models.

A4.3.1. Inlet Boundary Conditions

Inlet boundary conditions are commonly set as Neumann boundary conditions. This means that the value of a derivative state is enforced at the boundary nodes. In the case of fluid

dynamics, this derivative state value is fluid velocity. The reasons for using Neumann boundary conditions are because this method has been shown to yield stable simulation results, blood flow velocity can be measured in the clinic non-invasively with ultrasound Doppler or MRI [38], and in the absence of clinical measurements blood flow rates can be approximated based on vessel cross sectional area and scaling laws [39,40]. In the present work, flow rate waveforms are prescribed as the inlet boundary conditions. Average flow rates Q ($\text{cm}^3 \text{s}^{-1}$) were derived from an empirical relation between flow rate Q and ICA cross-sectional area [39]. The scaling law in steady state is as follows:

$$Q = 48.21 \times A^{1.84} \quad \text{Equation 28}$$

In steady-state simulations, a fully developed Poiseuille flow velocity profile (parabolic) was used to impose a constant flow rate of Q .

Transient simulations require time-dependent flow rate values ($Q(t)$). Firstly, the lumped parameter model presented in Chapter 2 provides time dependent pressure and flow at all epicardial locations in the cerebral arterial network. Similarly, the whole body model [41] may also provide flow waveforms suitable for use as inlet boundary conditions. Open-source repositories may provide ready to use pressure (as well as flow) waveforms suitable [42]. Finally, simple heart models [43] may also provide the information, especially since the shape and values of pressure within large vessels is virtually the same in the aorta, carotids, and other epicardial cerebral vessels. A representative pressure waveform is illustrated in Figure 19.

In transient (pulsatile) simulations, velocity waveforms derived from an average patient dataset are scaled according to Q . These scaled waveforms are applied at the inlets as fully developed Womersley velocity profiles [44]. Upon estimating cross sectional areas (A) from the available geometries, inlet steady state flow rates (Q) were calculated according to equation 28, both of which are presented in Table 6.

Case #	ICA cross-sectional area (cm ²)	Q (cm ³ s ⁻¹)
19	0.198183	2.453229
20	0.160897	1.671803
23	0.138690	1.272046
28	0.147754	1.429189
29	0.254833	3.896256
30	0.190057	2.271346
45	0.163667	1.725153
49	0.173822	1.927212
50	0.181510	2.086957
51	0.137995	1.260334
57	0.187826	2.222536
69	0.117692	0.940397
70	0.122983	1.019650
71	0.198528	2.461105
72	0.195509	2.392679
73	0.145908	1.396502
74	0.120298	0.979071
77	0.163241	1.716900
78	0.132925	1.176448
92	0.159571	1.646536

Table 6. Inlet cross sectional area and derived inlet flow rate. C: cerebral geometry from Aneurisk repository. ICA: Internal carotid artery. Q: blood flow rate (ml s⁻¹).

A4.3.2. Outlet Boundary Conditions

Outlet boundary conditions are enforced using weakly applied pressure conditions [45]. To do so, first downstream resistance values (R) were obtained from the literature. We assume

that pressure in the downstream domain is constant over the cross-sectional area of the outlet boundary, note that it is not constant over time in transient simulations. This means that pressure values are not directly assigned to elements at the outlet surface, but rather using the pressure-flow relationship:

$$p = p_0 + RQ \quad \text{Equation 29}$$

Where p is the mean lumen pressure at the outlet surface, p_0 is the distal pressure (nominally set to 0 mmHg), R is the network resistance of the outlet, and Q is the volumetric flow rate out of the outlet surface, i.e., the integration of velocity across the outlet surface. Rearranging equation 29, we derive the following relation:

$$R = \frac{p}{Q} \quad \text{Equation 30}$$

Using this method, time dependent pressure values are not needed, and downstream vascular resistance values may be obtained from the literature.

Because of the high variability in the imaged structures, a method for assigning a resistance value to each outlet surface was developed. First, outlet surfaces were grouped based on which major artery they were branching away from. The groups included middle cerebral artery (MCA), anterior cerebral artery (ACA) and other, which mainly branch from the ICA but do not contribute significantly to the flow volume. Literature values for network resistances of these groups were obtained and applied to the prescribed outlets. Resistances for individual outlets were calculated using a flow splitting principle derived from Murrays law [46] that asserts that flow distribution is scaled proportional to d^3 where d is daughter vessel diameter. Therefore:

$$\frac{Q_1}{Q_0} = \left(\frac{d_1}{d_0}\right)^3 \quad \text{Equation 31}$$

Where Q_0 and d_0 are parent vessel flow rate and diameter respectively, and Q_1 and d_1 are daughter vessel flow rate and diameter respectively. Parent vessel diameter was approximated as

$$d_0 = \sqrt[3]{\sum d_n^3} \quad \text{Equation 32}$$

according to Murrays law. Values for d_n are approximated by assuming the vessel cross section is circular, therefore:

$$d_n = 2 \sqrt{\frac{A_n}{\pi}} \quad \text{Equation 33}$$

By combining equations 30-33 we get the following equation for outlet resistance:

$$R_1 = \frac{p}{Q_0 \left(\frac{\left(\frac{A_1}{\pi}\right)^{3/2}}{\sum \left(\frac{A_n}{\pi}\right)^{3/2}} \right)} \quad \text{Equation 34}$$

We can once again substitute $p = RQ$ with $p_0 = 0$, $R = R_{total}$, and $Q = Q_0$ to get:

$$R_1 = \frac{R_{total}}{\left(\frac{\left(\frac{A_1}{\pi}\right)^{3/2}}{\sum \left(\frac{A_n}{\pi}\right)^{3/2}} \right)} \quad \text{Equation 35}$$

Where Q_0 is the total flow rate to a group of outlets, and A_n , is the cross-sectional area of outlet n in the group.

Cas e #	M2_1	M2_2	M2_3	M2_4	M2_5	ACA	AChA	ACoA	PCoA	OphA
19	0.0119 3	0.0123 4	0.0172 4	0.0103 4	-	0.01937	0.01748	-	-	-
20	0.0330 8	0.0148 7	-	-	-	0.01776	-	-	0.01419	-
23	0.0080 7	0.0100 0	0.0145 0	-	-	0.02665	0.00590	-	-	0.00586
28	0.0056 5	0.0117 9	0.0044 3	-	-	0.01955	0.01291	0.0206 7	-	-
29	0.0313 8	0.0132 4	0.0086 3	0.0120 1	-	0.04850	-	-	-	-

30	0.0336 4	0.0181 4	-	-	-	0.03390	0.00323	-	-	0.00536
45	0.0132 3	0.0089 8	0.0231 3	0.0068 1	-	0.01784	-	-	-	0.01351
49	0.0225 2	0.0106 8	0.0251 1	0.0089 6	-	0.04205 2	0.01268 4	-	0.00388 0	0.01117 8
50	0.0091 2	0.0105 4	0.0057 0	0.0076 6	0.006 1	0.02363	0.00318	-	0.00528	0.00343
51	0.0180 8	0.0170 7	-	-	-	0.03463	-	-	-	0.00655
57	0.0107 6	0.0187 8	0.0142 1	-	-	0.01323	-	0.0184 4	-	0.00833
69	0.0247 7	0.0194 5	-	-	-	0.02506	-	-	0.01636	-
70	0.0238 1	0.0089 7	0.0085 5	-	-	0.02126	0.01160	-	-	0.00757
71	0.0214 2	0.0240 8	-	-	-	0.02900	-	-	-	-
72	0.0264 3	0.0241 7	0.0279 2	-	-	0.03855	-	-	-	0.00880
73	0.0154 0	0.0105 2	0.0264 1	-	-	0.02961	-	-	-	0.01381
74	0.0402 7	0.0167 7	-	-	-	0.01691	0.00827	-	-	0.01054
77	0.0417 6	0.0149 4	-	-	-	0.01631	-	0.0226 5	-	-
78	0.0188 7	0.0268 6	-	-	-	0.01876	-	-	-	0.00768
92	0.0194 4	0.0279 9	-	-	-	0.03997	-	-	-	0.00924

Table 7. Outlet boundary condition data for each aneurysm geometry. All values are shown are in ($\times 10^4$ dynes s cm^{-5}). M2: second segment of middle cerebral artery. ACA: Anterior cerebral artery. AChA: Anterior choroidal artery. ACoA: Anterior communicating artery. PCoA: Posterior communicating artery. OpthA: Ophthalmic artery.

A4.3.3. Wall Boundary Conditions

The boundary condition at the vessel wall is implemented as a no-slip condition which is a special type of Neumann condition in which the velocity is explicitly set to 0.

A4.4. Finite Element Meshing

The repository provides finite element (FE) meshes of the geometries as illustrated in Figures 15 and 16 above. However, each hemodynamic simulator deploys its own unique data format. De novo meshing of any 3D geometry is therefore recommended. Briefly, the 3D images of the geometries are processed using the hemodynamic simulator's graphical user interface (GUI) to generate a centerline and volume representation within the simulator's data structures. The GUI then uses an open-source finite element meshing tool called TetGen to generate a tetrahedral finite element mesh suitable for numerical solutions of the 3D Navier-Stokes equations. The number of finite elements, number of edges, number of nodes, size of largest edge, for each of the 18 geometries are provided in Table 8. The FE meshes suitable for our hemodynamic simulator are provided on our github.

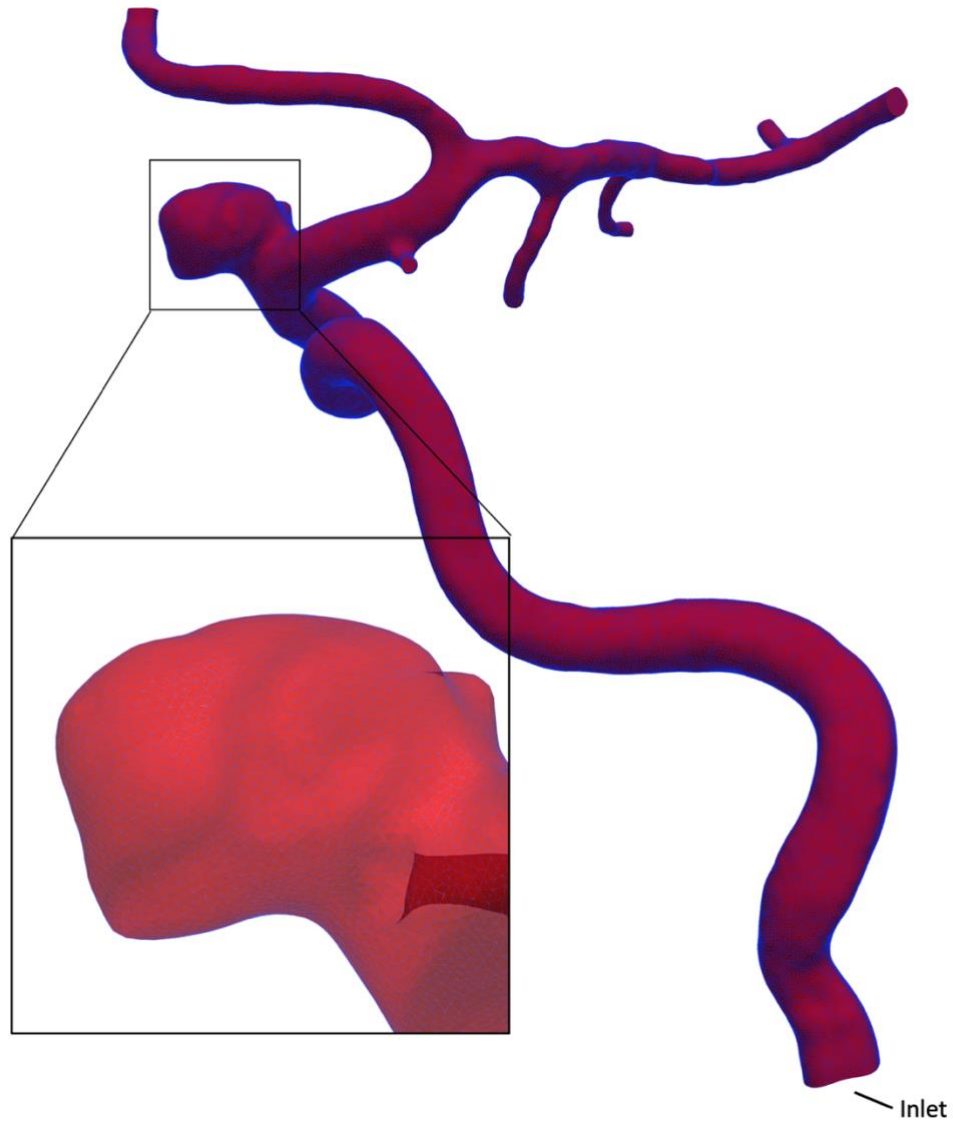


Figure 17. Visualization of FE mesh of an aneurysm geometry. The aneurysm is enlarged for increased visibility of the tetrahedral mesh elements on the aneurysm surface.

Case #	Global max edge size (mm)	Number of Nodes	Number of Elements	Number of Edges	Number of Faces
19	0.300	190122	1074480	128076	85384
20	0.240	177531	1023028	103482	68988
23	0.220	204067	1177776	117195	78130
28	0.240	204467	1177552	119442	79628
29	0.250	193090	1124246	103473	68982
30	0.220	193996	1125845	106350	70900
45	0.300	183472	1048673	113988	75992
49	0.240	206135	1188989	119040	79360
50	0.220	196058	1134126	110499	73666
51	0.230	178922	1039546	97344	64896
57	0.310	189464	1092500	109338	72892
69	0.220	186998	1080388	107100	71400
70	0.210	190402	1086333	120060	80040
71	0.280	190007	1093111	112431	74954
72	0.360	189673	1085353	116544	77696
73	0.225	178237	1010974	117654	78436
74	0.260	179437	1024860	111693	74462
77	0.260	197784	1145452	110370	73580
78	0.220	179851	1033878	107304	71536
92	0.265	181288	1039422	110127	73418

Table 8. Mesh properties of all 20 analyzed cases.

A4.5. Steady State and Transient Simulations

The free and open-source CFD platform SimVascular was used along with the boundary conditions detailed in A5.4 to simulate both steady-state and transient (pulsatile) blood

flow through each of the selected geometries. The SimVascular platform also provides an executable binary which postprocesses the output files of the simulation into both structured and unstructured VTK format geometric data. These data files can then be visualized and further processed using the free and open-source data visualization platform Paraview [47] as detailed in A.6. This platform can be used to visualize a variety of important indices for assessment of IA including WSS (Figure 17 and Figure 19), blood velocity fields (Figure 20), and oscillatory shear index (OSI) (Figure 21).

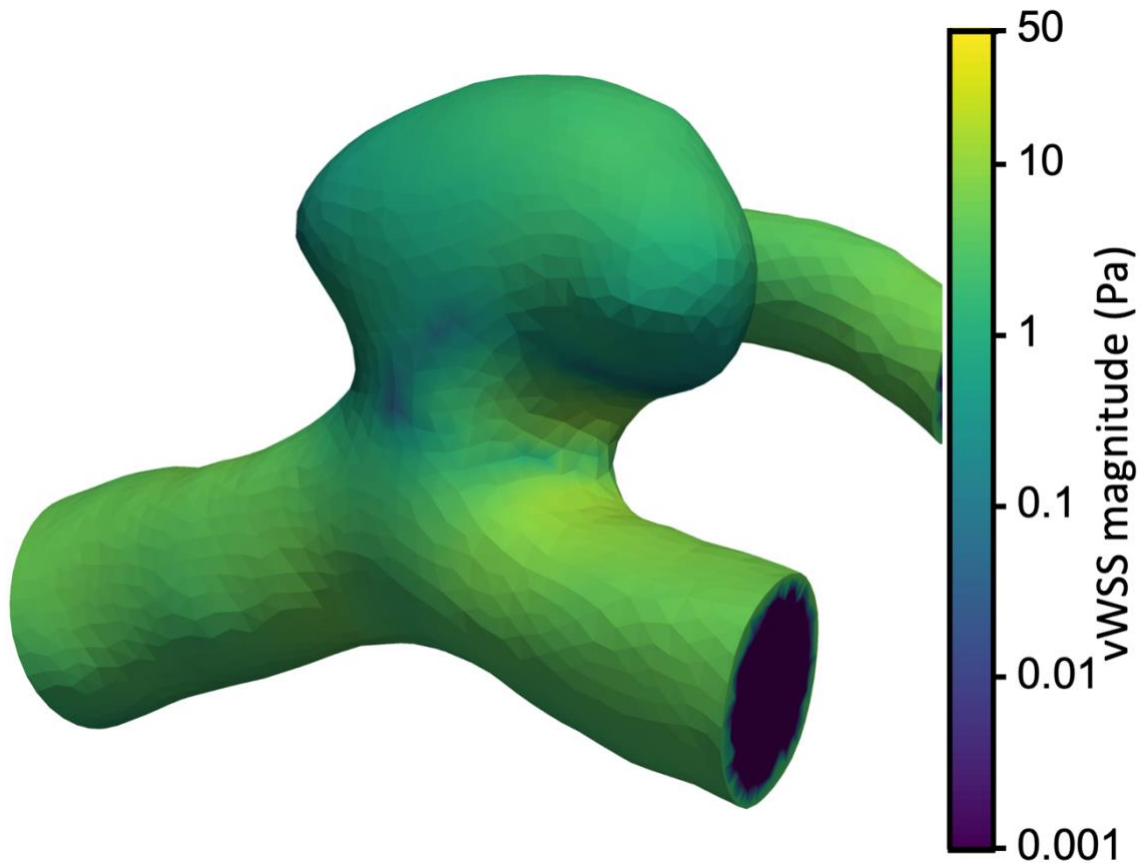


Figure 18. Wall shear stress magnitudes mapped on to an intracranial aneurysm geometry. Wall shear stress values are derived from velocity vectors which are outputs of the CFD simulation. The results shown are from a steady state simulation with constant flow rate imposed at the inlet.

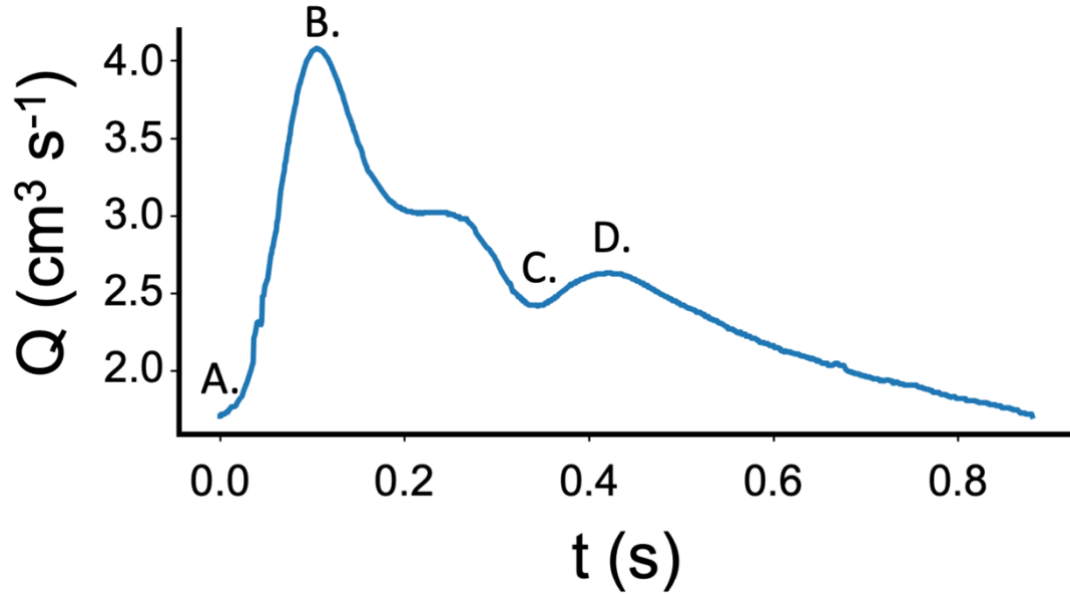


Figure 19. Plot of the volumetric flow rate (Q) versus time (t) at the inlet boundary. Four key timepoints are marked for reference by following figures. This flow profile has been scaled to the surface area of the inlet of case C0019 according to previously mentioned scaling laws. The waveform spans 0.86 seconds, which was taken as the length of a heartbeat. In practice, the waveform repeats periodically. A-B are respectively diastolic flow rate, systolic flow rate, trough of the dicrotic notch, peak of the dicrotic notch.

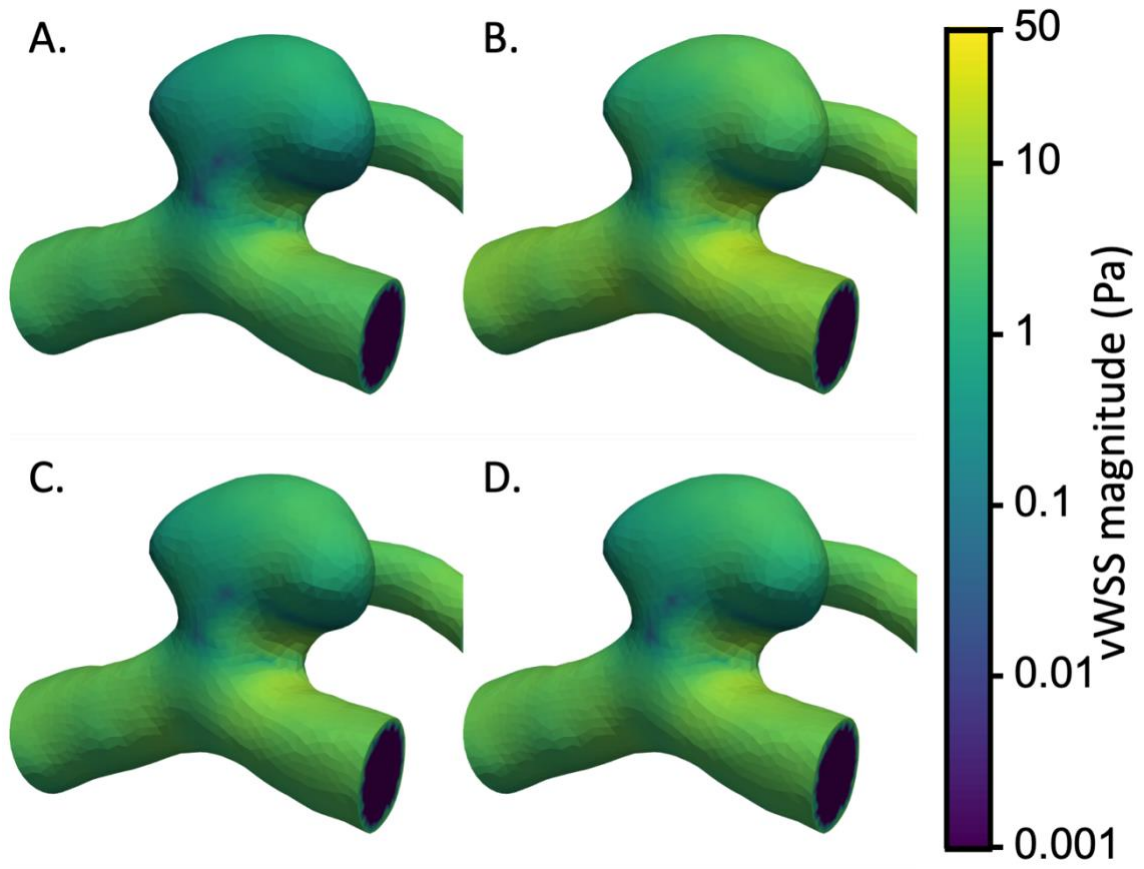


Figure 20. Wall shear stress is shown on aneurysm geometry at four key timepoints during a transient simulation. Wall shear stress magnitude is indicated both by arrow size and by colour. A-D reference key timepoints in the cardiac cycle which are shown in Figure 19.

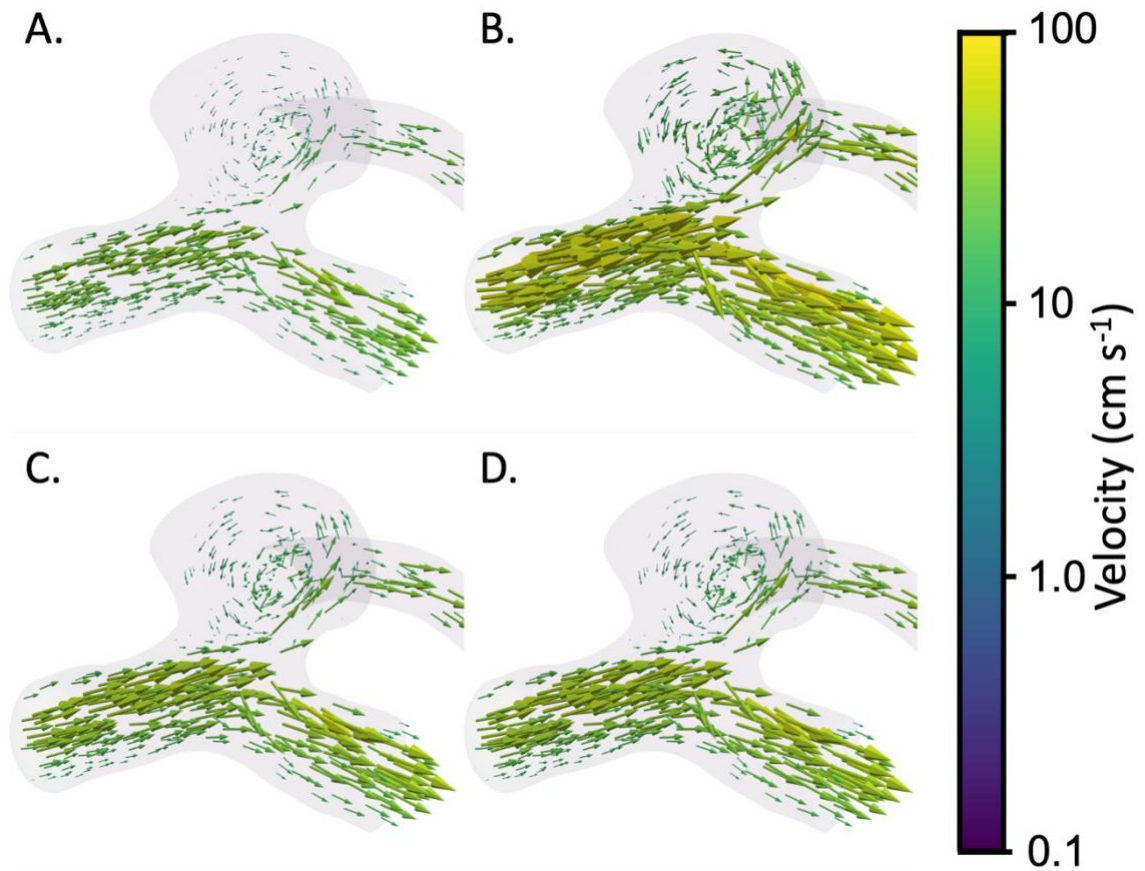


Figure 21. Blood velocity fields are shown within aneurysm geometry at four key timepoints during a transient simulation. Velocity vector direction is indicated by arrow direction. Velocity magnitude is indicated both by arrow size and by colour. A-D reference key timepoints in the cardiac cycle which are shown in Figure 19.

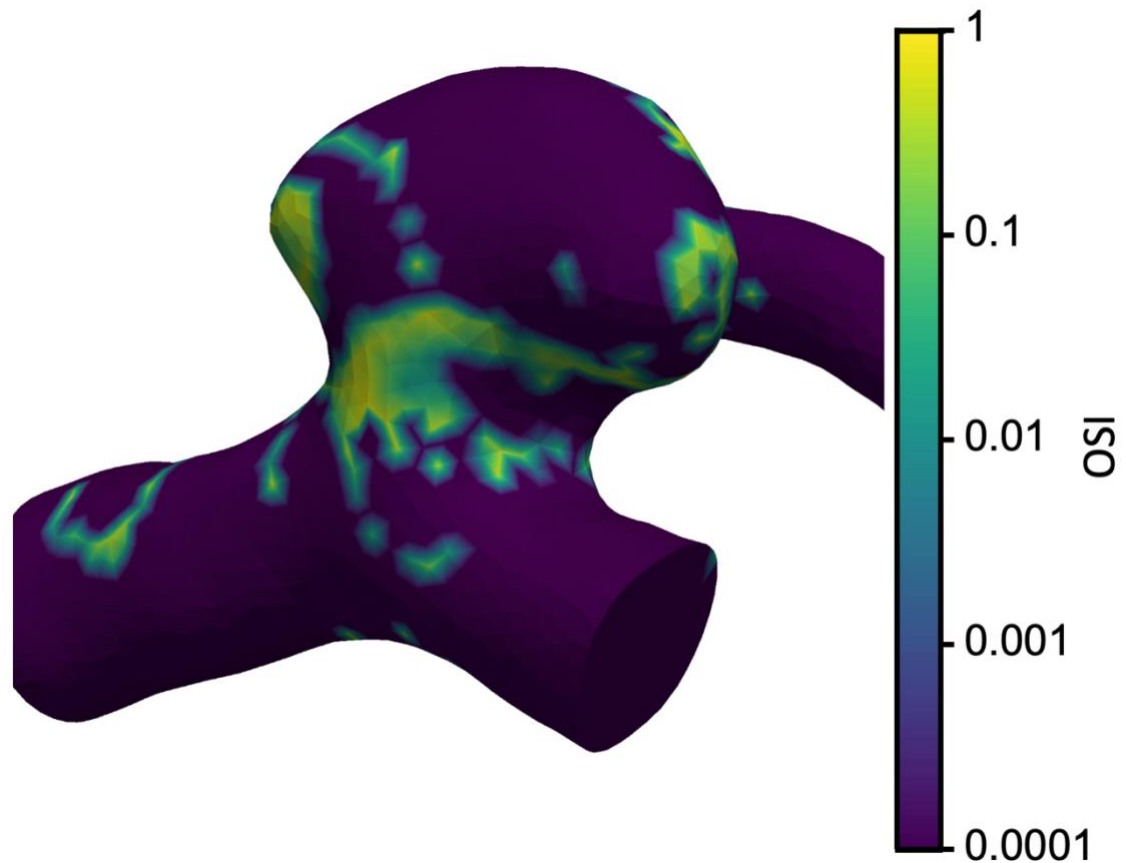


Figure 22. Oscillatory shear stress (OSI) mapped on to an intracranial aneurysm geometry. OSI values are derived from transient velocity vectors over the course of a single cardiac cycle which are outputs of the CFD simulation.

A4.6. Postprocessing

The simulator provides outputs encoded into binary VTK files. As seen in section 3.4, the user is able to visualize the output using the VTK GUI called ParaView [47]. Either by means of ParaView or otherwise, the data provided in the binary output can be manipulated to generate composite measurements.

A4.7. Applications

The presented modelling has multiple applications. Due to the intricate nature of cerebral vasculature, physical modelling provides insights into flow patterns. Computer modelling can be used to interpret experimental-clinical data to enhance its information content. [48].

Computer modelling can inform the physical modelling by providing expected boundary conditions and velocity profiles [49]. As image processing is an integral part of the computer modelling, it may be used to generate physical model geometries suitable for 3D printing. As our modest simulations show, flow patterns are complex in the vicinity of aneurysms. Prior to physical modelling (which is resource intensive), the computer models can be used to explore the relationships between aneurysm geometry and flow [50,51]. In addition to geometry, the relationships between aneurysm wall biomechanical properties (Young's modulus) and clinical observations of waveforms can be studied using the computer models [52,53]. Imaging is a key part in clinical assessment. Using routine images, the computer model can be personalized using established workflows [54]. A knowledge of the underlying fluid dynamics is known to assist in reducing repeat patient examination and reduce radiation exposure [54,56]. Further validation and verification of the computer model will advance its use in a clinical-experimental environment [56]. Due to their delicate biomechanical attributes, aneurysms are primed to rupture causing mortal cerebral hemorrhage. The presented computer modelling can be deployed to rapidly assess the rupture risk [48].

Whereas the technology has been presented, its customization for specific studies and deployment in itself requires significant effort [57]. As such, the model is prepared for larger data science studies for inclusion into in silico clinical trials [58]. In summary, a working model of 3D cerebral blood flow has been presented in the hope that it will find meaningful applications in the near future.

Appendix References

1. Heldt T. Computational models of cardiovascular response to orthostatic stress. Published online **2004**:185. <http://dspace.mit.edu/handle/1721.1/28761>
2. Ursino M, Giannessi M. A model of cerebrovascular reactivity including the circle of Willis and cortical anastomoses. *Ann Biomed Eng.* **2010**;38(3):955-974. doi:10.1007/S10439-010-9923-7/TABLES/2
3. Pope SR, Ellwein LM, Zapata CL, Novak V, Kelley CT, Olufsen MS. Estimation and identification of parameters in a lumped cerebrovascular model. *Math Biosci Eng.* **2009**;6(1):93-115. doi:10.3934/mbe.2009.6.93
4. Olufsen MS, Nadim A, Lipsitz LA. Dynamics of cerebral blood flow regulation explained using a lumped parameter model. *Am J Physiol Regul Integr Comp Physiol.* **2002**;282(2):R611-22. doi:10.1152/ajpregu.00285.2001

5. Figueroa CA, Vignon-Clementel IE, Jansen KE, Hughes TJR, Taylor CA. A coupled momentum method for modeling blood flow in three-dimensional deformable arteries. *Comput Methods Appl Mech Eng.* **2006**;195(41-43):5685-5706. doi:10.1016/j.cma.2005.11.011
6. Schollenberger J, Figueroa AC, Pfaller M. A lumped parameter model of cerebral blood flow regulation: Applications to simulation of carotid endarterectomy. Published online **2015**. https://bloodflow.engin.umich.edu/wp-content/uploads/sites/165/2014/07/20141201_thesis.pdf
7. Anselmino M, Scarsoglio S, Saglietto A, Gaita F, Ridolfi L. Transient cerebral hypoperfusion and hypertensive events during atrial fibrillation: a plausible mechanism for cognitive impairment. *Sci Rep.* **2016**;6(1):28635. doi:10.1038/srep28635
8. Scarsoglio S, Guala A, Camporeale C, Ridolfi L. Impact of atrial fibrillation on the cardiovascular system through a lumped-parameter approach. *Med Biol Eng Comput.* **2014**;52(11):905-920. doi:10.1007/s11517-014-1192-4
9. Mirramezani M, Shadden SC. A Distributed Lumped Parameter Model of Blood Flow. *Ann Biomed Eng.* **2020**;48(12):2870-2886. doi:10.1007/s10439-020-02545-6
10. Moore SM, Moorhead KT, Chase JG, David T, Fink J. One-Dimensional and Three-Dimensional Models of Cerebrovascular Flow. *J Biomech Eng.* **2005**;127(3):440-449. doi:10.1115/1.1894350
11. Alastruey J, Parker KH, Peiró J, Byrd SM, Sherwin SJ. Modelling the circle of Willis to assess the effects of anatomical variations and occlusions on cerebral flows. *J Biomech.* **2007**;40(8):1794-1805. doi:10.1016/j.jbiomech.2006.07.008
12. Sherwin SJ, Formaggia L, Peiró J, Franke V. Computational modelling of 1D blood flow with variable mechanical properties and its application to the simulation of wave propagation in the human arterial system. *Int J Numer Methods Fluids.* **2003**;43(6-7):673-700. doi:10.1002/flid.543
13. Jin W, Alastruey J. Arterial pulse wave propagation across stenoses and aneurysms: assessment of one-dimensional simulations against three-dimensional simulations and in vitro measurements. *J R Soc Interface.* **2021**;18(177):rsif.2020.0881. doi:10.1098/rsif.2020.0881
14. Mynard JP, Smolich JJ. One-Dimensional Haemodynamic Modeling and Wave Dynamics in the Entire Adult Circulation. *Ann Biomed Eng.* **2015**;43(6):1443-1460. doi:10.1007/s10439-015-1313-8
15. Liu X, Gao Z, Xiong H, et al. Three-dimensional hemodynamics analysis of the circle of Willis in the patient-specific nonintegral arterial structures. *Biomech Model Mechanobiol.* **2016**;15(6):1439-1456. doi:10.1007/s10237-016-0773-6
16. Moore S, David T, Chase JG, Arnold J, Fink J. 3D models of blood flow in the cerebral vasculature. *J Biomech.* 2006;39(8):1454-1463. doi:10.1016/j.jbiomech.2005.04.005
17. Jozwik K, Obidowski D. Numerical simulations of the blood flow through vertebral arteries. *J Biomech.* **2010**;43(2):177-185. doi:10.1016/j.jbiomech.2009.09.026
18. Morales HG, Larrabide I, Geers AJ, Aguilar ML, Frangi AF. Newtonian and non-Newtonian blood flow in coiled cerebral aneurysms. *J Biomech.* **2013**;46(13):2158-2164. doi:10.1016/j.jbiomech.2013.06.034
19. Jou LD, Mawad ME. Analysis of Intra-Aneurysmal Flow for Cerebral Aneurysms with Cerebral Angiography. *Am J Neuroradiol.* **2012**;33(9):1679-1684. doi:10.3174/ajnr.A3057

20. Berg P, Stucht D, Janiga G, Beuing O, Speck O, Thévenin D. Cerebral Blood Flow in a Healthy Circle of Willis and Two Intracranial Aneurysms: Computational Fluid Dynamics Versus Four-Dimensional Phase-Contrast Magnetic Resonance Imaging. *J Biomech Eng.* **2014**;136(4). doi:10.1115/1.4026108
21. Wiebers, D.O. Unruptured intracranial aneurysms: natural history, clinical outcome, and risks of surgical and endovascular treatment. *Lancet* **2003**, *362*, 103–110, doi:10.1016/S0140-6736(03)13860-3.
22. Investigators, S. Unruptured Intracranial Aneurysms — Risk of Rupture and Risks of Surgical Intervention. *N. Engl. J. Med.* **1998**, *339*, 1725–1733, doi:10.1056/nejm199812103392401.
23. Juvela, S.; Porras, M.; Poussa, K. Natural history of unruptured intracranial aneurysms: probability of and risk factors for aneurysm rupture. *J. Neurosurg.* **2008**, *108*, 1052–1060, doi:10.3171/JNS/2008/108/5/1052.
24. Tummala, R.P.; Bas ,Kaya, M.K.; Heros, R.C. Contemporary management of incidental intracranial aneurysms. *Neurosurg. Focus* **2005**, *18*, 1–7, doi:10.3171/foc.2005.18.1.10.
25. Winn, H.R.; Jane, J.A.; Taylor, J.; Kaiser, D.; Britz, G.W. Prevalence of asymptomatic incidental aneurysms: review of 4568 arteriograms. *J. Neurosurg.* **2002**, *96*, 43–49, doi:10.3171/jns.2002.96.1.0043.
26. Gasparotti, R.; Liserre, R. Intracranial aneurysms. *Eur. Radiol.* **2005**, *15*, 441–447, doi:10.1007/s00330-004-2614-8.
27. Schievink, W.I. Intracranial Aneurysms. *N. Engl. J. Med.* **1997**, *336*, 28–40, doi:10.1056/NEJM199701023360106.
28. Vlak, M.H.M.; Rinkel, G.J.E.; Greebe, P.; Algra, A. Independent Risk Factors for Intracranial Aneurysms and Their Joint Effect. *Stroke* **2013**, *44*, 984–987, doi:10.1161/STROKEAHA.111.000329.
29. Brown, R.D.; Huston, J.; Hornung, R.; DR.P.H.; Foroud, T.; Kallmes, D.F.; Kleindorfer, D.; Meissner, I.; Woo, D.; Sauerbeck, L.; et al. Screening for brain aneurysm in the Familial Intracranial Aneurysm study: frequency and predictors of lesion detection. *J. Neurosurg.* **2008**, *108*, 1132–1138, doi:10.3171/JNS/2008/108/6/1132.
30. Pfohman, M.; Criddle, L.M. Epidemiology of Intracranial Aneurysm and Subarachnoid Hemorrhage. *J. Neurosci. Nurs.* **2001**, *33*, 39–41, doi:10.1097/01376517-200102000-00005.
31. Korja, M.; Kivisaari, R.; Rezai Jahromi, B.; Lehto, H. Natural History of Ruptured but Untreated Intracranial Aneurysms. *Stroke* **2017**, *48*, 1081–1084, doi:10.1161/STROKEAHA.116.015933.
32. Ruigrok, Y.M.; Rinkel, G.J.E. Genetics of Intracranial Aneurysms. *Stroke* **2008**, *39*, 1049–1055, doi:10.1161/STROKEAHA.107.497305.
33. Khurana, V.G.; Meissner, I.; Meyer, F.B. Update on genetic evidence for rupture-prone compared with rupture-resistant intracranial saccular aneurysms. *Neurosurg. Focus* **2004**, *17*, 1–5, doi:10.3171/foc.2004.17.5.7.
34. Brisman, J.L.; Song, J.K.; Newell, D.W. Cerebral Aneurysms. *N. Engl. J. Med.* **2006**, *355*, 928–939, doi:10.1056/NEJMra052760.

35. Ingebrigtsen, T.; Morgan, M.K.; Faulder, K.; Ingebrigtsen, L.; Sparr, T.; Schirmer, H. Bifurcation geometry and the presence of cerebral artery aneurysms. *J. Neurosurg.* **2004**, *101*, 108–113, doi:10.3171/jns.2004.101.1.0108.
36. Humphrey, J.D.; Canham, P.B. Structure, mechanical properties, and mechanics of intracranial saccular aneurysms. *J. Elast.* **2000**, *61*.
37. Piccinelli, M.; Bacigaluppi, S.; Boccardi, E.; Ene-Iordache, B.; Remuzzi, A.; Veneziani, A.; Antiga, L. Geometry of the Internal Carotid Artery and Recurrent Patterns in Location, Orientation, and Rupture Status of Lateral Aneurysms: An Image-Based Computational Study. *Neurosurgery* **2011**, *68*, 1270–1285, doi:10.1227/NEU.0b013e31820b5242.
38. Karmonik, C.; Yen, C.; Grossman, R.G.; Klucznik, R.; Benndorf, G. Intra-aneurysmal flow patterns and wall shear stresses calculated with computational flow dynamics in an anterior communicating artery aneurysm depend on knowledge of patient-specific inflow rates. *Acta Neurochir. (Wien)*. **2009**, *151*, 479–485, doi:10.1007/s00701-009-0247-z.
39. Cebal, J.R.; Castro, M.A.; Putman, C.M.; Alperin, N. Flow–area relationship in internal carotid and vertebral arteries. *Physiol. Meas.* **2008**, *29*, 585–594, doi:10.1088/0967-3334/29/5/005.
40. Valen-Sendstad, K.; Piccinelli, M.; KrishnankuttyRema, R.; Steinman, D.A. Estimation of Inlet Flow Rates for Image-Based Aneurysm CFD Models: Where and How to Begin? *Ann. Biomed. Eng.* **2015**, *43*, 1422–1431, doi:10.1007/s10439-015-1288-5.
41. Joseph, J.J.; Hunter, T.J.; Sun, C.; Goldman, D.; Kharche, S.R.; McIntyre, C.W. Using a Human Circulation Mathematical Model to Simulate the Effects of Hemodialysis and Therapeutic Hypothermia. *Appl. Sci.* **2021**, *12*, 307, doi:10.3390/app12010307.
42. Ford, M.D.; Alperin, N.; Lee, S.H.; Holdsworth, D.W.; Steinman, D.A. Characterization of volumetric flow rate waveforms in the normal internal carotid and vertebral arteries. *Physiol. Meas.* **2005**, *26*, 477–488, doi:10.1088/0967-3334/26/4/013.
43. Marzo, A.; Singh, P.; Larrabide, I.; Radaelli, A.; Coley, S.; Gwilliam, M.; Wilkinson, I.D.; Lawford, P.; Reymond, P.; Patel, U.; et al. Computational hemodynamics in cerebral aneurysms: The effects of modeled versus measured boundary conditions. *Ann. Biomed. Eng.* **2011**, *39*, 884–896, doi:10.1007/s10439-010-0187-z.
44. Taylor, C.A.; Hughes, T.J.R.; Zarins, C.K. Finite element modeling of blood flow in arteries. *Comput. Methods Appl. Mech. Eng.* **1998**, *158*, 155–196, doi:10.1016/S0045-7825(98)80008-X.
45. Vignon-Clementel, I.E.; Alberto Figueroa, C.; Jansen, K.E.; Taylor, C.A. Outflow boundary conditions for three-dimensional finite element modeling of blood flow and pressure in arteries. *Comput. Methods Appl. Mech. Eng.* **2006**, *195*, 3776–3796, doi:10.1016/j.cma.2005.04.014.
46. Murray, C.D. The Physiological Principle of Minimum Work: I. The Vascular System and the Cost of Blood Volume. *Proc. Natl. Acad. Sci. U. S. A.* **1926**, *12*, 207–14, doi:10.1073/pnas.12.3.207.
47. Moreland, K.; Ayachit, U.; Geveci, B.; Quammen, C.; Demarle, D.; Moreland, K.; Bauer, A.; Boeckel, B.; Lipsa, D.; Westphal, M.; et al. The ParaView Guide. *Sandia Natl. Lab.* **2016**.

48. Steinman, D.A.; Taylor, C.A. Flow Imaging and Computing: Large Artery Hemodynamics. *Ann. Biomed. Eng.* **2005**, *33*, 1704–1709, doi:10.1007/s10439-005-8772-2.
49. Poepping, T.L.; Nikolov, H.N.; Thorne, M.L.; Holdsworth, D.W. A thin-walled carotid vessel phantom for Doppler ultrasound flow studies. *Ultrasound Med. Biol.* **2004**, *30*, 1067–1078, doi:10.1016/j.ultrasmedbio.2004.06.003.
50. Steinman, D.A.; Poepping, T.L.; Tambasco, M.; Rankin, R.N.; Holdsworth, D.W. Flow Patterns at the Stenosed Carotid Bifurcation: Effect of Concentric versus Eccentric Stenosis. *Ann. Biomed. Eng.* **2000**, *284*, 28, 415–423, doi:10.1114/1.279.
51. Kefayati, S.; Holdsworth, D.W.; Poepping, T.L. Turbulence intensity measurements using particle image velocimetry in diseased carotid artery models: Effect of stenosis severity, plaque eccentricity, and ulceration. *J. Biomech.* **2014**, *47*, 253–263, doi:10.1016/j.jbiomech.2013.09.007.
52. Wong, E.Y.; Nikolov, H.N.; Thorne, M.L.; Poepping, T.L.; Rankin, R.N.; Holdsworth, D.W. Clinical Doppler ultrasound for the assessment of plaque ulceration in the stenosed carotid bifurcation by detection of distal turbulence intensity: a matched model study. *Eur. Radiol.* **2009**, *19*, 2739–2749, doi:10.1007/s00330-009-1457-8.
53. Khoshniat, M.; Thorne, M.L.; Poepping, T.L.; Hirji, S.; Holdsworth, D.W.; Steinman, D.A. Real-time numerical simulation of Doppler ultrasound in the presence of nonaxial flow. *Ultrasound Med. Biol.* **2005**, *31*, 519–528, doi:10.1016/j.ultrasmedbio.2004.12.013.
54. Taylor, C.A.; Steinman, D.A. Image-Based Modeling of Blood Flow and Vessel Wall Dynamics: Applications, Methods and Future Directions. *Ann. Biomed. Eng.* **2010**, *38*, 1188–1203, doi:10.1007/s10439-010-9901-0.
55. Piccinelli, M.; Veneziani, A.; Steinman, D.A.; Remuzzi, A.; Antiga, L. A Framework for Geometric Analysis of Vascular Structures: Application to Cerebral Aneurysms. *IEEE Trans. Med. Imaging* **2009**, *28*, 1141–1155, doi:10.1109/TMI.2009.2021652.
56. Ethier, C.R.; Steinman, D.A. Exact fully 3D Navier-Stokes solutions for benchmarking. *Int. J. Numer. Methods Fluids* **1994**, *19*, 369–375, doi:10.1002/fld.1650190502.
57. Marsden, A.L.; Esmaily-Moghadam, M. Multiscale modeling of cardiovascular flows for clinical decision support. *Appl. Mech. Rev.* **2015**, *67*, doi:10.1115/1.4029909.
58. Viceconti, M.; Hunter, P.; Hose, R. Big Data, Big Knowledge: Big Data for Personalized Healthcare. *IEEE J. Biomed. Heal. Informatics* **2015**, *19*, 1209–1215, doi:10.1109/JBHI.2015.2406883.

Curriculum Vitae

Name: Timothy J. Hunter

Post-secondary Education:

The University of Western Ontario - London, Ontario, Canada

2016-2020 B.Sc. (Honours Specialization in Medical Biophysics)

The University of Western Ontario - London, Ontario, Canada

2020-2022 M.Sc. Medical Biophysics

Related Work Experience:

Research Assistant, London Health Sciences Centre (KCRU) 2020-2022

Research Assistant, University of Western Ontario (Goldman Lab) 2019-2020

Publications:

Hunter TJ, Joseph JJ, Anazodo U, Kharche SR, McIntyre CW, Goldman D. Atrial Fibrillation and Anterior Cerebral Artery Absence Reduce Cerebral Perfusion: A De Novo Hemodynamic Model. *Applied Sciences*. **2022**; 12(3):1750.

Joseph JJ, Hunter TJ, Sun C, Goldman D, Kharche SR, McIntyre CW. Using a Human Circulation Mathematical Model to Simulate the Effects of Hemodialysis and Therapeutic Hypothermia. *Applied Sciences*. **2022**; 12(1):307.

Mendelson, A.A.; Ho, E.; Scott, S.; Vijay, R.; Hunter, T.; Milkovich, S.; Ellis, C.G.; Goldman, D. Capillary module haemodynamics and mechanisms of blood flow regulation in skeletal muscle capillary networks: Experimental and computational analysis. *J. Physiol.* **2022**, 600, 1867–1888.

Mendelson AA, Milkovich S, Hunter TJ, et al. The capillary fascicle in skeletal muscle: Structural and functional physiology of RBC distribution in capillary networks. *J Physiol.* **2021**;599(8):2149-2168.